

## Editorial corner – a personal view

### Role of polymers in developing phase change materials for energy storage

A. S. Luyt\*

Department of Chemistry, University of the Free State (Qwaqwa Campus), Private Bag X13, Phuthaditjhaba, 9866, South Africa

It is now more important than ever to be able to store energy over longer periods and to effectively release the energy when needed. Research on sensible heat and latent heat phase change materials (PCMs), which started about 20 years ago, still plays an important role in addressing this problem. PCMs absorb and store heat energy when undergoing a solid-solid or solid-liquid phase change. Problems associated with the use of PCMs are their lack of long-term stability, especially under conditions of thermal cycling, the stability of the PCM-container system, and effective heat transfer, because most PCMs have very low thermal conductivity.

Apart from a multitude of inorganic materials investigated and commercially used as PCMs in energy storage, commercial waxes and fatty acids were found to be the most promising organic latent heat PCMs. Normally the latent heat of melting method for energy storage is used, but some research focused on the latent heat of solid-solid transitions. Commercial paraffin waxes are cheap with moderate thermal storage densities and a wide range of melting temperatures. They undergo negligible sub-cooling and they are chemically inert and stable with no phase segregation. On the downside they have low thermal conductivity, relative high liquid viscosities, and they are difficult to contain in a certain shape or size.

This is where polymers come into the picture. A fair amount of research has been done on the

microencapsulation of PCMs by different polymers. Work has also been done on preparing phase change materials consisting of paraffin wax dispersed in a polymer as a supporting material (shape-stabilised PCM). In this case research concentrated mostly on the use of polyolefins. The effective temperature range of such a PCM falls between the melting point of the wax and that of the polymer. It is, however, important that there must be little co-crystallization between the paraffin wax and the polymer. This system has long-term thermal stability under cycling conditions, and the PCM is well contained within the polymer matrix. There are only two persistent problems: low thermal conductivity (which may be overcome by using conductive polymers or by doping) and poor mechanical properties in the presence of high paraffin wax contents.



Prof. Dr. Riaan Luyt  
Member of International Advisory Board

\*Corresponding author, e-mail: [luytas@qwa.uovs.ac.za](mailto:luytas@qwa.uovs.ac.za)  
© BME-PT and GTE

# Vibration welding of alpha and beta isotactic polypropylenes: Mechanical properties and structure

J. Varga<sup>1\*</sup>, G. W. Ehrenstein<sup>2</sup>, A. K. Schlarb<sup>3</sup>

<sup>1</sup>Laboratory of Plastics and Rubber Technology, Department of Physical Chemistry and Material Science, Budapest University of Technology and Economics, H-1111 Budapest, Műgyetem rkp. 3, Hungary

<sup>2</sup>Lehrstuhl für Kunststofftechnik, University of Erlangen-Nürnberg, D-91058 Erlangen-Tennelohe, Am Weichselgarten 9, Germany

<sup>3</sup>Institut für Verbundwerkstoffe GmbH, Universität Kaiserslautern, D-67663 Kaiserslautern, Erwin-Schrödinger Str., Germany

Received 4 January 2008; accepted in revised form 12 January 2008

**Abstract.** Propylene homo- and copolymers (both random and block types) with and without beta nucleation were injection moulded and the related plaques joined by linear vibration welding. The melt flow index (MFI) of the polypropylenes was different. During vibration welding the pressure has been varied (0.5, 2 and 8 MPa). The properties of the welded plaques were determined under both static (tensile) and dynamic conditions (Charpy impact). It was found that the mechanical performance of the welds could strongly be improved when beta nucleated PP plaques were combined with each other. In other combinations the ‘weaker’ alpha modification controls the mechanical response. The supermolecular structure of the weld was assessed by polarised light microscopy using thin microtomed sections. Formations of the weld morphology along with its effects on the mechanical performance were discussed.

**Keywords:** processing technologies, isotactic polypropylene, vibration welding, mechanical properties, morphology

## 1. Introduction

Welding is widely used to produce plastic products of complicated shape and large size [1]. The structure-property relationships of vibration welded semicrystalline polymers, especially in case of isotactic polypropylene (iPP), have been studied comprehensively [2–9]. It was established that the morphology of the weld joint (seam) reflects very sensitively the conditions of the welding process (e.g. [3–8]). During vibration welding the parts to be welded are clamped in tools and pressed together with a defined load ( $F$ ). After this ‘close-up’ process, the upper part is brought to oscillation (vibration step) – cf. Figure 1. Depending on the type of the oscillation movement one distinguishes

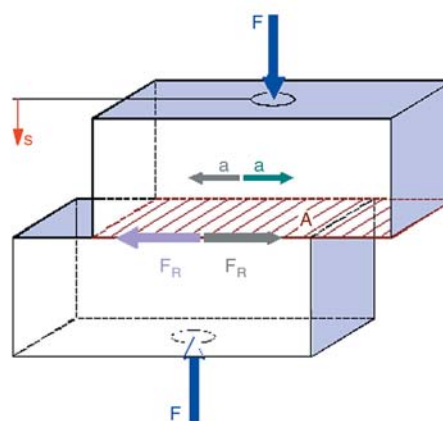


**Figure 1.** Scheme of the linear vibration welding. Note: this figure also indicates the major technological parameters:  $F$  – load,  $A$  – initial surface of the parts,  $a$  – amplitude,  $s$  – penetration

\*Corresponding author, e-mail: [jvarga@mail.bme.hu](mailto:jvarga@mail.bme.hu)  
© BME-PT and GTE

between linear, rotation and twisting types vibration welding [9]. The surface layers of the thermoplastic parts became molten owing to the frictional heat evolved during welding. As a consequence, a molten layer appears between the welded parts. Under pressure, some molten polymer flows outside of the welding surface creating some flash when the parts move against each other. The relative movement of the weldable parts is termed as welding distance ( $s$ ) or penetration.

Depending on the technological parameters, viscoelasticity of the polymer melt and the thermal conductivity conditions, the heat development and loss (via heat radiation and conduction, incl. the heat capacity of the flash giving melt) may be equilibrated. This results in quasi-stationary melt stage in the weld. Recall that heat generates due to the periodic loading of the melt of viscoelastic nature (mechanical loss work) in the quasi-stationary stage. Next the vibration is stopped but the parts are still held together under pressure. In this pressure holding phase the welding joint solidifies owing to cooling, which is accompanied by crystallization from the melt. Major technology parameters of linear vibration welding are: welding pressure ( $p$ , which is calculated by dividing the closing force,  $F$ , by the initial contact surface of the parts), vibration time ( $t_v$ ), amplitude and frequency of the vibration ( $a$  and  $f$ , respectively). Note that the above parameters control the thermal and flow behaviours of the molten zone in the welding joint. The welding process was split in four phases by Potente *et al.* [2]: 1 – friction in the solid phase, 2 – onset of an instationary melt, 3 – appearance of a quasi-stationary melt, and 4 – cooling. These four phases are displayed in Figure 2, which shows the

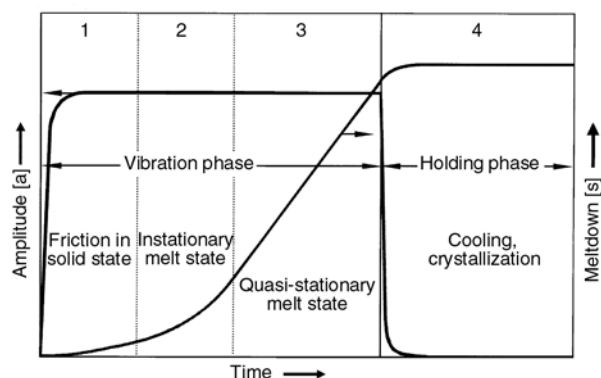


**Figure 2.** Phases of the vibration welding showing also the changes in the amplitude ( $a$ ) and welding distance or penetration ( $s$ ) in time

variation of the penetration ( $s$ ) and vibration amplitude ( $a$ ) as a function of the welding time. By increasing the welding pressure the related curves shift towards smaller times. Parallel to the increase in the welding pressure, the thickness and strength of the weld joint decrease monotonously [9].

iPP is a polymer existing in several crystalline modifications (polymorphism) [10]. Adding selective beta nucleators, the formation of the beta modification of iPP can be triggered, even under usual processing conditions [10, 11]. Beta-iPP has a higher toughness than the alpha version, which form usually in non-nucleated iPP. The toughness improvement is more prominent for high than for low molecular weight iPP grades [10, 12]. Therefore, it is of great importance to check whether or not the high toughness of beta iPP can be exploited in welded parts. So, the present contribution is dedicated to the vibration welding of beta-nucleated injection moulded iPP plaques. In order to get more general information, the work covered the following combinations of the welded plaques: alpha/alpha (i.e. non-nucleated/non-nucleated), alpha/beta (i.e. non-nucleated/beta-nucleated) and beta/beta (beta-nucleated/beta-nucleated). The morphology of the weld joints was studied by polarised light microscopy (PLM) and discussed.

## 2. Experimental

### 2.1. Production and characterisation of the plaques to be welded

Plaques (145×70×4 mm) were injection moulded on an Engel ES 200/50HZ machine. The injection molding parameters were: melt temperature: 240°C, injection speed: 70 mm/s, holding pressure: 330 MPa. As propylene homopolymers the following Tipplén grades of Tisza Chemical Works (Tiszaújváros, Hungary) were selected: Tipplén H384, Tipplén H543 and Tipplén H781. In addition to homopolymers, also propylene-co-ethylene copolymers – both random (Tipplén R351) and block (Tipplén K392) types – were involved in this study. The iPP types were modified by incorporation of crystal water free calcium salt of pimelic acid in 0.1 wt%. This highly selective proprietary beta-nucleating agent was developed in our laboratory [13]. For the various iPPs the following coding was introduced: the first capital refers to the absence or presence of the beta nucleator (A and B,

respectively). The second capital indicates the type of the PP, so the homopolymer, random and block copolymers are given by H, R and K, respectively. Finally, the third number refers to the melt flow index (MFI) of the related PP grade. Note that with increasing number the MFI of the PP decreases. All above iPPs crystallise predominantly in the beta form in the presence the above-disclosed nucleator, at least when plaques are produced by compression molding, whereby a long isothermal step of the crystallisation ( $T_c = 110\text{--}135^\circ\text{C}$ ) was set [10]. On the other hand, the injection-moulded plaques possess a molding-induced skin-core structure with mixed polymorphic composition [11]. This affects markedly the mechanical performance of the related systems [14]. The core of a beta-nucleated iPP contains beta-spherulites and the skin layer consists of alpha-cylindrites, as demonstrated in our previous works [11]. The morphology and polymorphic composition in the skin layer depend on the iPP type (homo- or copolymer) and its characteristics (mostly MFI), distance from the gate and injection speed. The beta content of the core of the plaques was assessed by the  $k$ -value, which was introduced by Turner Jones *et al.* [15]. The  $k$ -values were determined by wide angle X-ray scattering (WAXS) after removal of the skin layers by polishing. The  $k$ -values of the injection-moulded beta plaques, along with the skin layer thicknesses are reported in Table 1. Table 1 also lists the measured MFI values. Recall that information on the MFI contains the last number in our coding. Attention should be paid to the fact that the same number refers to very similar MFI values for all kind of iPPs. This is in accord with the designation policy of the iPP producer.

## 2.2. Welding

Welding tests were run on a fully automatic Branson Ultraschall device Model 2800. During weld-

ing the penetration and pressure can be monitored as a function of time. The welding pressure was varied (8, 2 and 0.5 MPa) while the amplitude (0.7 mm) and frequency (240 Hz) of the vibration were kept constant. As various iPP pairs were used for welding, the above-introduced code had to be extended as follows: AA, AB and BB mean the welding pairs alpha/alpha, alpha/beta and beta/beta, respectively. In the new code this capital combination appears first.

## 2.3. Mechanical testing

The tensile strength ( $\sigma$ ) of the parent and welded plaques was determined by a Zwick universal testing machine (Ulm, Germany) at ambient temperature ( $RT$ ) with 20 mm/min deformation rate. The Charpy impact strength (more precisely: energy,  $W$ ) was measured by an impact pendulum at the following conditions:  $RT$ , incident impact speed: 2.9 m/s, incident energy of the hammer: 2 J. Prior to the related tests the flash of the welded joints was removed. Specimens cut from the parent plaques did not break under these impact conditions. Therefore they were notched until a depth of ca. 1.5 mm (i.e. 1/3 of the overall thickness in line with the related standard).

## 2.4. Morphology detection

The morphology of the injection moulded plaques and the welds was studied in PLM using microtomed sections (ca. 10  $\mu\text{m}$  thickness). The microsections were embedded in a thermoset resin (Eukitt) and cured. Inserting a lambda-plate in between the polariser and analyser diagonally assessed the type of birefringence. PLM micrographs taken with and without using lambda plate are presented in this paper.

**Table 1.** Characteristics of the PP types and their injection molded plaques used

Sample	MFI* [dg/min]	Non-nucleated	$\beta$ -nucleated	
		Thickness of skin (d), [ $\mu\text{m}$ ]	Thickness of skin (d), [ $\mu\text{m}$ ]	k value
H3	13.4	<0	<20	0.89
H5	5.5	~40	~40	0.89
H7	0.76	~400	~400	0.90
R3	11	<20	<20	0.85
K3	12	<20	<20	0.99

\*MFI was measured at  $230^\circ\text{C}$  with 21.6 N load

### 3. Results and discussion

#### 3.1. Mechanical properties

The tensile mechanical characteristics of the welded PP pairs as functions of their types and welding pressure are summarised in Table 2. One can see that the best mechanical performance exhibited those weld pairs, which were produced at the lowest welding pressure. The tensile strength-strain curves of the related specimens were similar to those of semicrystalline polymers showing prominent necking and substantial deformation (several hundred %) before final fracture. The high elongation (ductility) was due to the sharp necking, which occurred away of the weld joint, i.e. in one or other half ('leg') of the welded specimens (cf. Figure 3). The iPP pairs welded at low welding pressure did not break at the weld line. So, the yielding stress of the parent plaques agreed fairly well with that of the welded ones. Note that alpha-iPP undergoes a highly localised necking, whereas this is far more diffuse in the beta-modification. In welded pairs, containing beta-PP, necking appears

**Table 2.** Tensile strength ( $\sigma$ ) of the PP pairs welded at different pressures (viz. 0.5, 2 and 8 MPa)\*

Sample	$\sigma(8)$ [MPa]	$\sigma(2)$ [MPa]	$\sigma(0.5)$ [MPa]
A-H3	35.1		
B-H3	28.4		
AA-H3	26.5	30.2	32.9
BB-H3	24.9	26.8	>29.0
AB-H3	24.6	26.5	>29.8
A-H5	34.3		
B-H5	27.4		
AA-H5	25.7	31.6	32.7
BB-H5	24.8	26.8	>27.4
AB-H5	23.9	26.5	>28.0
A-H7	30.8		
B-H7	26.5		
AA-H7	13.1	18.1	>30.2
BB-H7	21.1	24.3	>26.1
AB-H7	20.5	23.8	>26.6
A-R3	28.7		
B-R3	25.8		
AA-R3	25.6	26.8	27.5
BB-R3	21.8	23.3	>24.5
AB-R3	23.0	25.0	25.5
A-K3	23.8		
B-K3	19.2		
AA-K3	15.1	17.0	21.0
BB-K3	15.3	16.2	>19.2
AB-K3	15.2	16.0	19.5

\*The tensile strength was determined at RT using 20 mm/min deformation speed. The coding is referred in the text

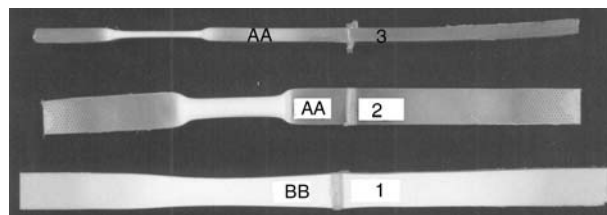


**Figure 3.** Necking due to static mechanical loading in the dumbbells cut from the welded pairs AA-H7 and BB-H7. Designation: 1 – BB-H7: flat on, 2 – AA-H7 flat on, 3 – AA-H7 edge on

exclusively in the beta PP section (cf. Figure 3). This can be attributed to the difference in the yield stresses between beta and alpha-iPPs – beta-iPP yields always at a lower stress than the alpha version [10]. Specimens welded at high pressures (2 and 8 MPa) had low tensile strength data and they break in the weld. This was accompanied with low elongation at break (several percent) values, as well.

#### 3.2. Impact strength of the welds

Results of the Charpy impact tests are summarised in Table 3. This table also contains the notched Charpy impact strength data (marked by asterisk) of the parent injection moulded plaques. However, the latter data are of indicative nature and serve merely to collate the impact performance of the various PPs used. Considering the notched Charpy impact strengths of the parent plaques, one can recognise that the toughness increases with decreasing MFI for both alpha- and beta-iPPs according to the expectation. The relative increment in the Charpy impact strength is higher for the beta-nucleated compared to the corresponding alpha versions. Comparing the impact strength of the H, R and K grades at the same MFI (which is rather high in this case), one can only notice a slight increase in the toughness owing to beta nucleation. This is in line with the state of knowledge as disclosed for example in [10, 11].

Data in Table 3 display that the Charpy impact strength of the welded plaques increases markedly with decreasing MFI for both alpha- and beta-iPPs. The welded plaques from H7 iPP possess the highest impact toughness. For example, BB-H7, when welded at low pressure, exhibits outstanding impact strength (ca. 70 kJ/m<sup>2</sup>). It is noteworthy that both tensile and impact strengths of the AA and AB



welded pairs are practically the same (cf. data in Tables 2 and 3). This suggests that the ‘weak site’ is in the non-nucleated (alpha) section. In fact, the

**Table 3.** Notched and unnotched Charpy impact strength (precisely: energy) data for the PP pairs welded at different pressures (viz. 0.5, 2 and 8 MPa)

Sample	W(8) [kJ/m <sup>2</sup> ]	W(2) [kJ/m <sup>2</sup> ]	W(0,5) [kJ/m <sup>2</sup> ]
A-H3		3.53*	
B-H3		4.41*	
AA-H3	5.00	10.00	11.67
BB-H3	5.00	10.42	13.33
AB-H3	5.00	9.58	11.67
A-H5		3.53*	
B-H5		5.88*	
AA-H5	5.42	10.00	10.83
BB-H5	5.83	9.17	9.58?
AB-H5	5.42	9.17	9.58
A-H7		4.71*	
B-H7		15.29*	
AA-H7	5.00	10.83	31.25
BB-H7	5.83	8.33	70.83
AB-H7	6.67	9.17	30.00
A-R3		3.24*	
B-R3		3.53*	
AA-R3	6.67	10.83	13.33
BB-R3	6.25	11.67	20.83
AB-R3	6.67	11.25	12.50
A-K3		4.41*	
B-K3		7.98*	
AA-K3	6.67	7.50	10.42
BB-K3	9.58	9.58	30.00
AB-K3	8.33	8.33	10.00

Notes: the impact strength (W) was determined at RT using 2.9 m/s impact speed. The coding of the materials is referred in the text. Data with \* are measured on standardised, notched specimens

failure in the welded AB pairs occurred always in the alpha part close to the weld joint. The above test results confirm that joints of very high toughness can be produced when plaques of beta-nucleated iPPs of low MFI are welded together. However, this claim holds only for BB pairs, i.e. when both plaques are beta-nucleated.

### 3.3. Supermolecular structure of the welding joint

The supermolecular structure of the weld joint is controlled by the actual thermal, mechanical and flow conditions, which all affect the recrystallisation of the molten layer during welding. The above conditions strongly change with the geometrical place. The complex supermolecular structure obtained at low pressure welding for the pairs AA-H7, BB-H7, AB-H7 and AA-H5, respectively, are shown in Figures 4–8. The related PLM micrographs are taken from microtomed sections cut transverse to both the plaque plane (i.e. along the cross section) and the welding joint. One can see that the non-nucleated plaques contain large alpha-spherulites, in which few negative beta-spherulites are sporadically embedded. The average size is about 50–60 micrometer (cf. Figure 4). The size of the beta-spherulites of beta-nucleated plaques is markedly lower and their size is more uniform than in the alpha plaques (Figure 6).

The shape of the joints welded at low pressure is similar for the different PP combinations: the joint

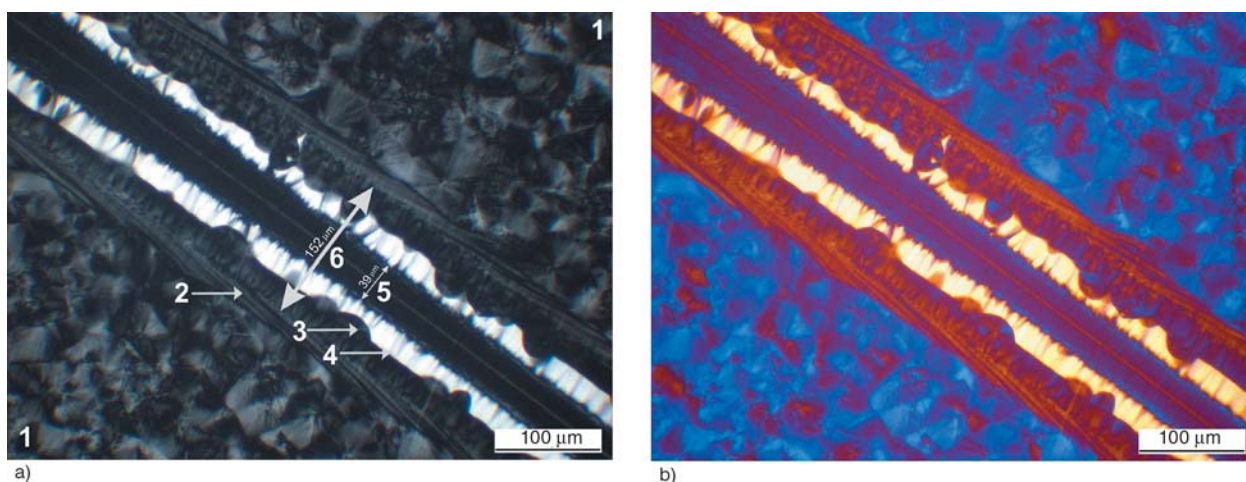


**Figure 4.** a) PLM micrograph on the morphology of the AA-H7 weld produced at a welding pressure of  $p = 0.5$  MPa (middle part of the weld). Designations: 1 – parent plaque, 2 – layer with deformed spherulites, 3 – spherulitic layer, 4 – beta-cylindrite due to shear induced nucleation, 5 – melt flow channel, 6 – overall thickness of the weld seam. b) PLM micrograph taken with lambda plate

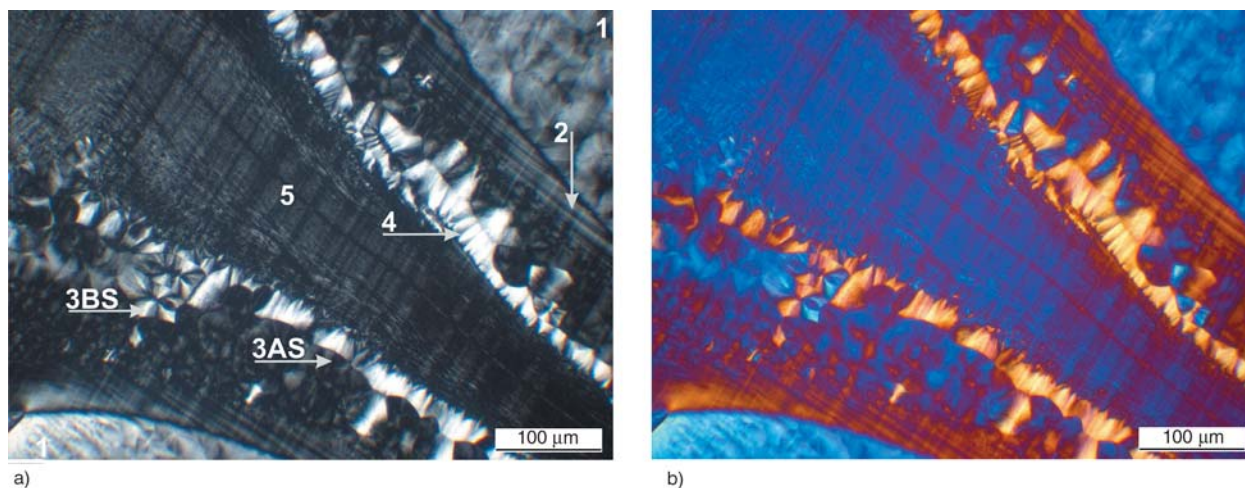


**Figure 5.** a) PLM micrograph on the morphology of the AA-H7 weld produced at a welding pressure of  $p = 0.5$  MPa (outer part, close to the flash). Designations: 1 – parent plaque, 2 – layer with deformed spherulites, 3AS and 3BS – individual alpha and beta-spherulites in the spherulitic layer, 4 – beta-cylindrite due to shear induced nucleation, 5 – melt flow channel. b) PLM micrograph taken with lambda plate

has the same thickness in the middle section and broadens somewhat only towards the edges of the plaques (Figure 5). The formation of the multilayer structure in non-nucleated iPP welds was explained in our earlier works [4, 16] by the onset of a molten layer consisting of two zones with different flowability. In the middle section of the joint a so-called flow channel developed being flanked by plastic zones from both sides. In the plastic zone the melt viscosity is high owing to the locally low temperature. So, the related zone has some restricted flow especially under low welding pressures. Crystallisation in the plastic zones occurs under quasi-quiescent melt conditions. Accordingly, microcrystalline and/or spherulitic structures appear depending on the actual thermal conditions. It is worth of noting that in the spherulitic layers the size of the spherulites is smaller than in the parent plaques. This testifies that the spherulites were recrystallised from the melt. In the flow channel flow-induced cylindritic crystallisation took place. Cylindrites are induced by row nuclei and oriented along the flow direction. Owing to the very high density of nuclei, the resulting supermolecular structure can hardly be resolved in optical level. The spherulites of the parent plaques in the vicinity of the molten layer undergo partial melting. The partially molten spherulites deform upon the acting pressure and orient themselves towards the flash. As a consequence, at the boundary of the parent plaque and the weld joint, a layer composed of deformed spherulites appears. The extent of spherulite defor-

mation and the thickness of the related layer increase towards the edges of the welded plaques (cf. Figures 4 and 5).

Apart of the above supermolecular features, a further peculiarity can be observed in the welds of the specimens AA-H7 (Figure 5) and AA-H5 (Figure 8). It both outer flanks of the flow channel a highly birefringent, negative-type beta layers can be recognised. These layers, rich in beta modification of iPP, are generated by the shear stresses developed between the flow and plastic zones. The influence of the related ‘shearing’ on the resulting supermolecular structures was the topic of our former works (e.g. [17]). It has to be emphasised that the beta-rich layers are far more prominent in the AA-H7 (cf. Figure 5) than in the AA-H5 specimens (cf. Figure 8). Moreover, no such layer could be resolved in the AA-H3 weld pairs at all. This is a clear indication that with decreasing melt viscosity (from H7 towards H3) of the iPP the evolving shear stress in the boundary layer between the flow and plastic zones decreases and thus no shear-induced beta nucleation has been triggered.

The formation of this beta-rich layer is hampered in beta-nucleated iPP owing to the beta-nucleator present (cf. Figure 6). Note that in presence of the beta nucleator the spherulitic crystallisation occurs at higher temperature and/or at higher rate than the cylindritic one.

It is clearly perceptible in Figure 7 that the non-nucleated and beta-nucleated melts in the welded AB pairs do not interpenetrate. So, the supermolec-



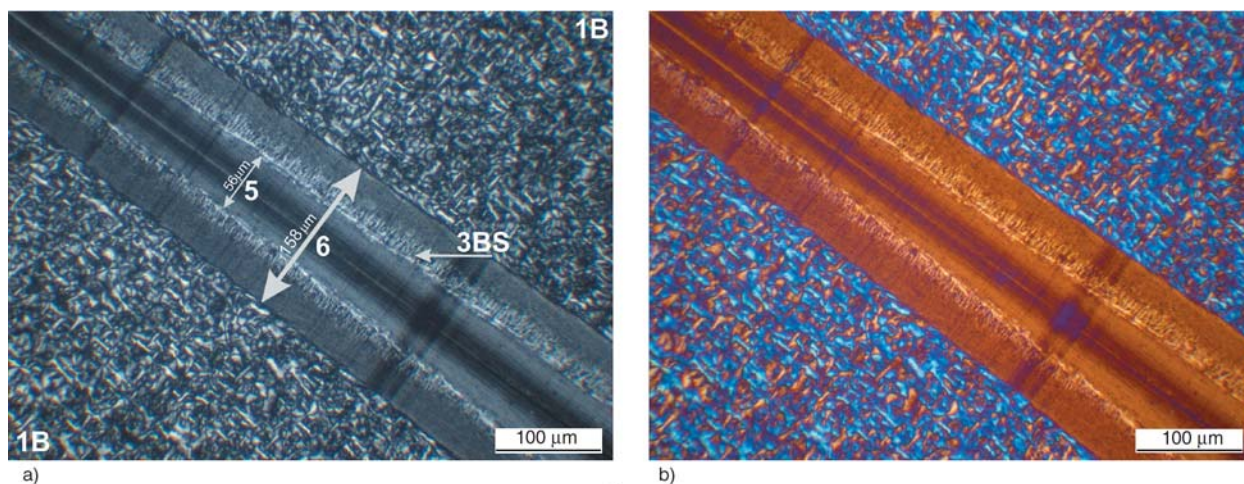


**Figure 6.** a) PLM micrograph on the morphology of the BB-H7 weld produced at a welding pressure of  $p = 0.5$  MPa. Designations: 1B – parent plaque, 3BS – beta-spherulitic layer, 5 – melt flow channel, 6 – overall thickness of the weld seam. b) PLM micrograph taken with lambda plate

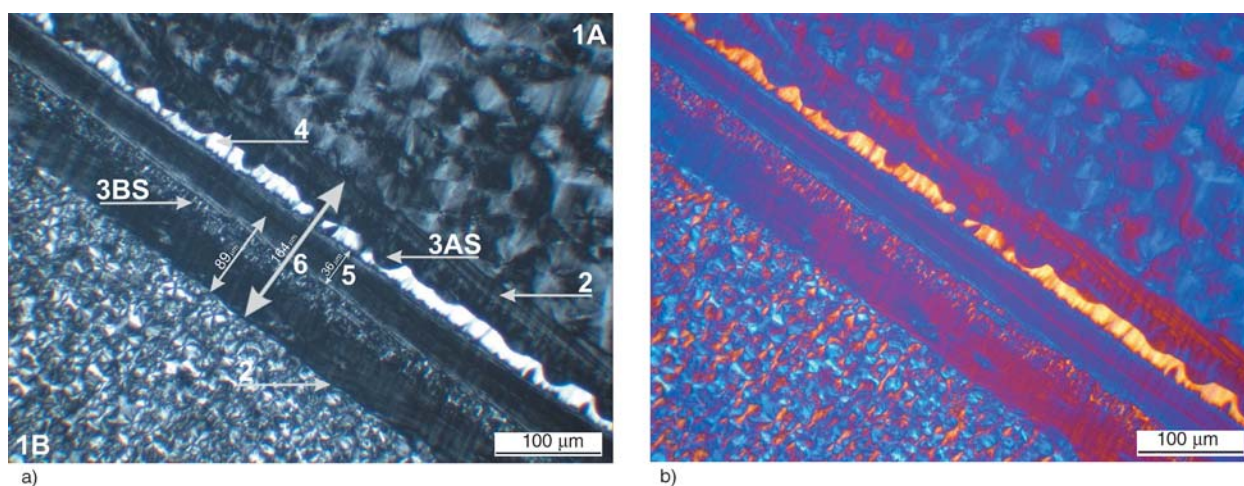


**Figure 7.** a) PLM micrograph on the morphology of the AB-H7 weld produced at a welding pressure of  $p = 0.5$  MPa. Designations: 1A and 1B – non-nucleated and beta-nucleated parent plaques, 2 – layer with deformed spherulites, 3AS and 3BS – beta-spherulites, 4 – beta-cylindrite due to shear induced nucleation, 5 – melt flow channel, 6 – overall thickness of the weld seam. b) PLM micrograph taken with lambda plate

ular structure located between the contact plane and the parent plaques on the A and B sides is identical what can be found in AA and BB pairs. The above described morphological features are well demonstrated in the PLM micrographs in Figures 4–8. The interpretation of the related morphologies is supported by the exhaustive legends of the corresponding figures. The rules of the formation of multi-layered weld appearance will be the topics of a companion contribution.

The morphology of the joint is far less complex when produced at high welding pressures ( $p = 2$  and 8 MPa). Figure 9 shows that the weld seam is smaller compared to the joint produced at low pressure (cf. Figures 4–8). The supermolecular struc-

ture, produced at high welding pressure, cannot be resolved optically – during this joint formation obviously the melt flow dominated. This induced an oriented cylindritic structure in the whole joint. The related joints show the same characteristics as described by us earlier using non-nucleated iPPs for welding [3–9]. It is noteworthy that the joint accommodates a delta shape at the edges of the welded plaques. Moreover, the weld thickness in the flash is markedly larger compared to that of the middle section. The single layer morphology due to high pressure welding contains highly oriented molecules and related supermolecular structures, the orientation of which is transverse to the static mechanical loading and parallel to the impact



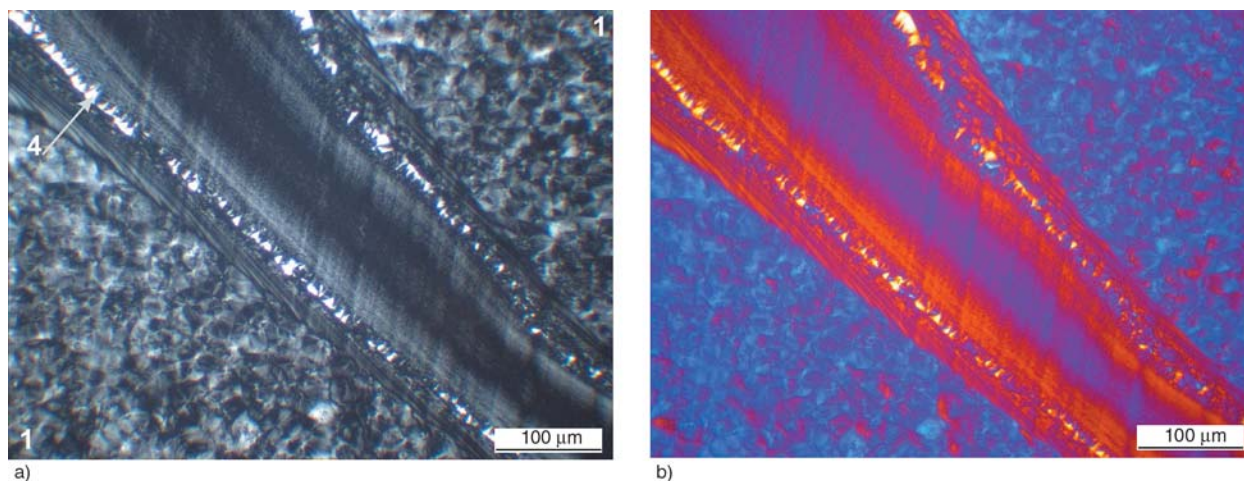


**Figure 8.** a) Shear induced beta-cylindritic layer in weld seam of AA-H5 plaques produced at a welding pressure of  $p = 0.5$  MPa. b) PLM micrograph taken with lambda plate

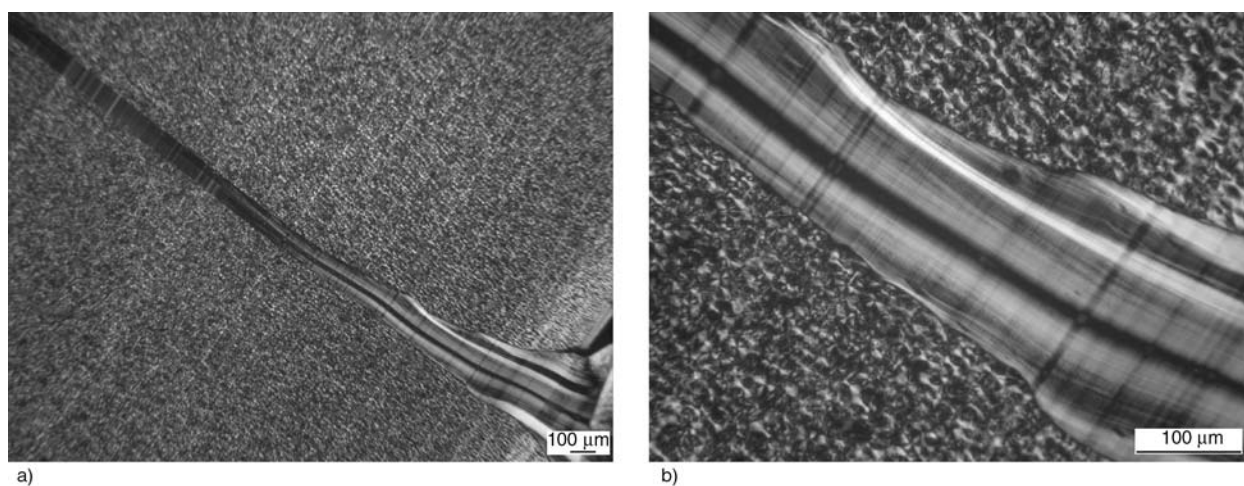


**Figure 9.** a) PLM micrographs showing the supermolecular structures in BB-H5 weld produced at a high welding pressure ( $p = 8$  MPa). b) A part of the weld at higher magnification

direction. This is disadvantageous for both cases, which is well reflected by the related results. One can thus speculate that this layer has some stress concentration effect. By contrast, the multiple layer structure of the welds, generated by low pressure welding, has some gradient structure in mechanical sense. The stress imposed can be more efficiently spread, transferred to a large area, due to which the load bearing capacity of the welds is strongly improved (cf. data in Tables 2 and 3).

#### 4. Conclusions

Based on this work addressing the property-structure relationships in vibration welded polypropylene plaques without and with beta nucleation, the following conclusions can be drawn:

- The mechanical and impact strength of the joints can be markedly improved using beta-nucleated PPs. It was also found that the lower the melt flow index of the beta-iPP, the higher the property improvement under static and dynamic conditions. This beneficial effect can be, however, only triggered when both welded parts are beta-nucleated versions and relatively low welding pressures are applied.
- The outstanding weld strengths of parts joined at low welding pressure are connected with their complex multilayer structure. Its formation is due to the development of two molten zones of highly different flowability. In the vicinity of the initial contact surface a flow channel develops, which is flanked from both sides by plastic zones. In the flow channel flow-induced crystallisation occurs resulting in an oriented cylin-

dritic structure. In the plastic zone the crystallisation takes place in a quasi quiescent melt yielding spherulitic and/or microcrystalline structures. This multilayer structure ensures an efficient stress transfer via its complex morphology so that the corresponding weld shows excellent static and dynamic mechanical properties.

- High welding pressure results in a single layer weld with strongly aligned molecules and supermolecular structures. As their orientation is disadvantageous in respect to the static and dynamic loadings and the oriented layer acts as stress concentrator, the welds exhibit low performance.

## Acknowledgements

The authors thank the Volkswagen Foundation for the financial support of this project. Thanks are also to M. Giese, J. Vetter and I. Mudra for their involvement in the experimental works.

## References

- [1] Andrew W.: Handbook of plastics joining: A practical guide. Plastic Design Library, Norwich (1997).
- [2] Potente H., Michel P., Ruthmann B.: Eine Analyse des Vibrationsschweißens. *Kunststoffe*, **77**, 711–716 (1987).
- [3] Schlarb A. K., Ehrenstein G. W.: Vibrationsschweißen – Ein Serienschweißverfahren aus werkstofftechnischer Sicht. *Kunststoffe*, **78**, 541–545 (1988).
- [4] Schlarb A. K., Ehrenstein G. W., Varga J.: Vibration welding of polypropylene (in Hungarian). *Plastics and Rubber*, **25**, 339–347 (1988).
- [5] Schlarb A. K.: Zum Vibrationsschweißen von Polymerwerkstoffen. PhD Dissertation, Universität Kassel (1989).
- [6] Schlarb A. K., Ehrenstein G. W.: The impact strength of butt welded vibration welds related to microstructure and welding history. *Polymer Engineering and Science* **29**, 1677–1682 (1989).
- [7] Giese M., Ehrenstein G. W.: Studies of the deformation and failure behavior of vibration welded polypropylene welds. in 'Antec 92, Conference Proceedings, Detroit, USA' 349–352. (1992).
- [8] Giese M.: Fertigungs- und werkstofftechnische Betrachtungen zum Vibrationsschweißen von Polymerwerkstoffen. PhD Dissertation, Universität Erlangen-Nürnberg (1995).
- [9] Vetter J., Ehrenstein G. W.: Online-Qualitäts-Erkennung beim Vibrationsschweißen: Neuronale Netzwerke klassifizieren Schweißnahtfestigkeit. *Kunststoffe*, **88**, 986–989 (1998).
- [10] Varga J.:  $\beta$ -Modification of isotactic polypropylene: preparation, structure, processing, properties, and application. *Journal of Macromolecular Science, Part B: Physics*, **41**, 1121–1171 (2002).
- [11] Varga J., Mudra I., Ehrenstein G. W.: Morphology and properties of  $\beta$ -nucleated injection molded isotactic polypropylene. in 'Antec 98, Conference Proceedings, Atlanta, USA' Vol. III., 3492–3496 (1998).
- [12] Karger-Kocsis J., Varga J., Ehrenstein G. W.: Comparison of the fracture and failure behavior of injection-molded  $\alpha$ - and  $\beta$ -polypropylene in high-speed three-point bending tests. *Journal of Applied Polymer Science*, **64**, 2057–2066 (1997).
- [13] Varga J., Mudra I., Ehrenstein G. W.: Highly active thermally stable  $\beta$ -nucleating agents for isotactic polypropylene. *Journal of Applied Polymer Science*, **74**, 2357–2368 (1999).
- [14] Karger-Kocsis J., Friedrich K.: Effect of skin-core morphology on fatigue crack propagation in injection-moulded polypropylene homopolymer. *International Journal of Fatigue*, **11**, 161–168 (1989).
- [15] Turner-Jones A., Aizlewood J. M., Beckett D. R.: Crystalline forms of isotactic polypropylene. *Macromolecular Chemistry*, **75**, 134–154 (1964).
- [16] Varga J.: Supermolecular structure of isotactic polypropylene. *Journal of Materials Science*, **27**, 2557–2579 (1992).
- [17] Varga J., Karger-Kocsis J.: Rules of supermolecular structure formation in sheared isotactic polypropylene melts. *Journal of Polymer Science, Part B: Polymer Physics*, **34**, 657–670 (1996).

# Viscoelastic characterization of an EPDM rubber and finite element simulation of its dry rolling friction

D. Felhős<sup>1\*</sup>, D. Xu<sup>1</sup>, A. K. Schlarb<sup>1</sup>, K. Váradi<sup>2</sup>, T. Goda<sup>3</sup>

<sup>1</sup>Institut für Verbundwerkstoffe GmbH (Institute for Composite Materials), University of Kaiserslautern, D-67663 Kaiserslautern, Germany

<sup>2</sup>Department of Machine and Product Design Budapest University of Technology and Economics H-1111, Műegyetem rkp.3, Budapest, Hungary

<sup>3</sup>Institute of Mechanical Engineering and Safety Techniques, Bánki Donát Faculty of Mechanical Engineering, Budapest Tech, H-1081 Budapest, Népszínház u. 8, Hungary

Received 30 October 2007; accepted in revised form 12 January 2008

**Abstract.** The viscoelastic properties of an ethylene/propylene/diene rubber (EPDM) containing 30 parts per hundred parts rubber [phr] carbon black (CB) were determined by dynamic mechanical thermal analysis (DMTA) measurements. A 15-term Maxwell-model was created to describe the time-dependent material behavior of this rubber. The frictional behavior under dry rolling conditions was studied on a home-built rolling ball (steel)-on-plate (rubber) (RBOP) test rig. Both normal and tangential forces were detected during the measurements. The rolling test was simulated with the MSC.Marc finite element (FE) software using the evaluated viscoelastic material properties. Results of the experimental tests and of the simulation were compared and a good agreement was found between them.

**Keywords:** modeling and simulation, rubber, viscoelasticity, finite element method (FEM), rolling friction

## 1. Introduction

Rubbers are utilized widely in mechanical engineering. Tires, v-belts, belts, rollers are made of rubbers or of rubber-based composite materials. The water-, heat- and chemical-resistances, the excellent and tailorable elastic properties, the high coefficient of friction make them as first-choice materials for the above applications. However the construction and design of the related rubber parts need profound knowledge on the non-linear and viscoelastic properties of the related rubbers. The internal damping of rubbers can be useful, but the same phenomenon can cause unfavorable energy dissipation during rolling or cyclic fatigue-type loading of rubbery elements.

The exact analytical calculation of the observed strains during mechanical loading of rubbery ele-

ments is a great challenge due to the complexity of the viscoelastic material models. Although some simplified analytical methods were developed to evaluate for example the friction resistance or internal heat generation in viscoelastic materials during rolling contact, they failed for more complex stress states or for repeated stresses [1–9]. On the other hand the finite element (FE) method is able to handle complex viscoelastic material models owing to the permanent advancement of the software and hardware background. This progress makes possible to perform more complex and at the same time, accurate simulations [10–12].

The aim of this study was to investigate the rolling friction whereby a steel ball is rolling on a rubber plate.

\*Corresponding author, e-mail: felhoes@ivw.uni-kl.de  
© BME-PT and GTE



The linear-viscoelastic properties of the rubber were determined by dynamic mechanical thermal analysis (DMTA). On the basis of DMTA measurements a master curve was created and a 15-term Maxwell-model was fitted to this master curve. To describe the incompressibility and the non-linear behavior of the rubber, i.e. the non-linear stress-strain curve, the Mooney-Rivlin material model was used. The constants of the two term Mooney-Rivlin material law were calculated by simplified equations [20–21].

For the simulations the FE software MSC.Marc was used.

The rolling friction of an ethylene/propylene/diene rubber (EPDM) was measured in an oscillating rolling ball (steel)-on-plate (rubber) configuration (Oscillating-RBOP) and simulated by FEM. Friction force, normal load and coefficient of friction (COF) were determined. The results of the tests and the simulations were compared with each other and discussed.

## 2. Experimental

### 2.1. Rolling friction test

Rolling friction tests were carried out on a home built test rig with oscillating rolling ball (100Cr6,  $d = 2r = 14$  mm,  $R_a = 1$   $\mu$ m) and stationary rubber plate (cf. Figure 1). The steel ball is driven by the

driver part to conduct oscillating rolling motion on the rubber plate. The load is applied by a lever system. The reciprocating linear rolling of the ball occurred with an amplitude of  $A = 25.06$  mm, a cyclic frequency of  $f = 1/30$  Hz under a normal load of 140 N. The normal and friction load are measured by load cells. The load cell which measures the normal load (Load cell 1, cf. Figure 1) is placed under the base plate, while the other load cell which measures the friction force (Load cell 2) is placed at the driver element. The ball is rolling in the guiding edges of the driver part (cf. Figure 1c).

#### 2.1.1. Test conditions

The linear reciprocating movement of the driver part and the reciprocating rolling of the ball have different amplitudes and speeds due to the set-up. As starting point of our calculations we used the known movement of the driver part, which reciprocated with a given amplitude and frequency. The ball's kinematical and contact geometry is shown in Figure 2. One could see the original and the end position of the ball and the direction of the oscillation shown by arrows. Figure 2 also shows the change of the ball's displacement and the change of the curve of rolling velocity versus the time, where  $T$  is the period (30 sec). On the right side one can see the contact geometry, where  $r$  is the radius of the rolling steel ball (7 mm),  $g$  is the width of the

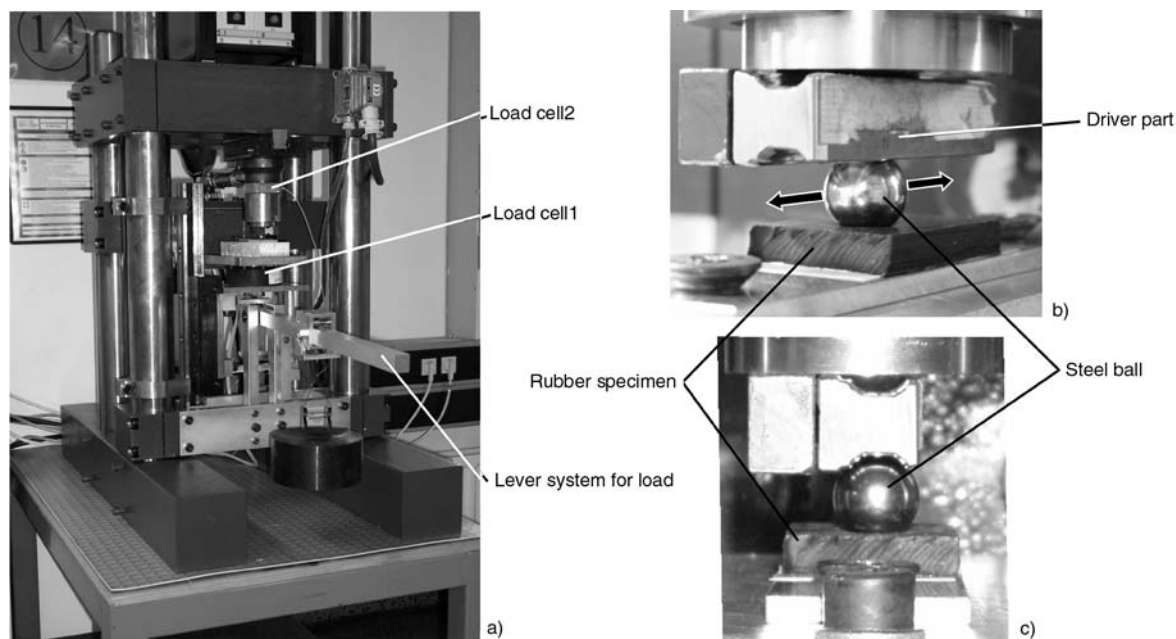


**Figure 1.** Overview of the Oscillating-RBOP machine (a), detailed view of steel ball rolling on a flat rubber specimen (b), front view of the set-up (c)

guiding groove on the driver part (8.6 mm),  $h$  is the vertical distance from the center point to the upper contact point of the ball, calculated by Equations (1) and (2):

$$h = r \cdot \cos \alpha \quad (1)$$

where

$$\alpha = \arcsin \frac{g}{2 \cdot r} \quad (2)$$

We assumed the pure rolling of the ball without any slip at the contact both with the driver part and with the rubber specimen. With this assumption the position and the velocity of the driver part could be calculated using Equations (3) and (4):

$$s_D(t) = -A \cdot \cos\left(\frac{2\pi}{T} \cdot t\right) \quad (3)$$

$$v_D(t) = \frac{2\pi}{T} \cdot A \cdot \sin\left(\frac{2\pi}{T} \cdot t\right) \quad (4)$$

The ratio of the driver part's displacement and velocity to those of the rolling ball is constant. The displacement ( $s(t)$ ) and the velocity ( $v(t)$ ) of the rolling ball is smaller than that of the driver part. This ratio is given by the Equation (5):

$$\frac{s(t)}{s_D(t)} = \frac{v(t)}{v_D(t)} = \frac{r}{r+h} \quad (5)$$

Using Equations (3), (4) and (5), the displacement and the speed of the rolling ball can be described by Equations (6) and (7):

$$s(t) = -A \cdot \left(\frac{r}{r+h}\right) \cos\left(\frac{2\pi}{T} \cdot t\right) \quad (6)$$

$$v(t) = \frac{2\pi}{T} \cdot A \cdot \left(\frac{r}{r+h}\right) \sin\left(\frac{2\pi}{T} \cdot t\right) \quad (7)$$

The maximum of the displacement ( $s(t)_{\max}$ ) of the rolling ball means the amplitude of the reciprocating motion. This will be reached at  $t = 0$ ,  $t = T/2$  and  $t = T$ . The maximum of the rolling velocity is reached at  $t = T/4$  and  $t = 3T/4$  (cf. Figure 2). Substituting the data into Equations (6) and (7), the displacement and the velocity of the rolling ball can be described by Equations (8) and (9):

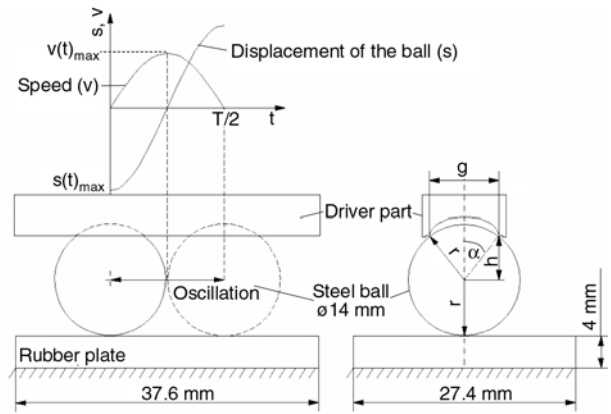


**Figure 2.** Schematic sketches of the contact geometry and of the ball's kinematics in a half cycle

$$s(t) = -0.007019 \cdot \cos\left(\frac{2\pi}{T} \cdot t\right) \quad [\text{m}] \quad (8)$$

$$v(t) = -0.00147 \cdot \sin\left(\frac{2\pi}{T} \cdot t\right) \quad \left[\frac{\text{m}}{\text{s}}\right] \quad (9)$$

If we fixed the center point of the coordinate system at the middle point of the ball, the apparent angular velocity of the ball ( $\omega(t)$ ) could be calculated as Equation (10):

$$\omega(t) = \frac{v(t)}{r} \quad (10)$$

This value will be needed later by the description of the boundary conditions of the FE simulation.

### 2.1.2. Results of the rolling frictiontest

During the measurement the normal and the tangential force were registered (cf. Figure 3). It shows the change of the normal and tangential forces in one cycle and the calculated coefficient of

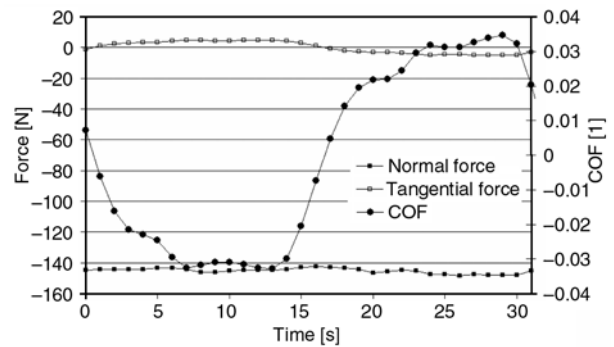


**Figure 3.** Change of the normal- and tangential forces vs. the time in one cycle and the change of the calculated coefficient of friction (COF)

friction (COF). The COF is calculated as the ratio of the friction force to the normal load (Equation (11)):

$$\text{COF} = \frac{F_T}{F_N} \quad (11)$$

where  $F_T$  is the tangential force,  $F_N$  is the normal force.

The sign of the friction force is changing, due to the changing rolling direction. The normal force is constant; however a small deviation was observed at the end of the cycle. The highest and smallest values of the tangential force are approximately  $\pm 4.8$  N. Between the direction changes of the rolling ball a plateau can be seen in the tangential force vs. time curve. The COF vs. time curve has also an oscillation, the maximal and minimal value of it are approximately +0.034 as well as -0.034.

## 2.2. Material characteristics

An EPDM rubber, containing 30 parts per hundred parts rubber [phr] carbon black (CB) was investigated in this study. The investigated EPDM stock was prepared in a laboratory internal mixer and the curatives were introduced on a laboratory open mill. The recipe used was as follows: EPDM (Keltan® 512 of DSM Elastomers, Sittard, The Netherlands): 100 parts; carbon black (N550): 30 parts; ZnO: 5 parts; stearic acid: 1 part, sulfur: 1.5 parts, N-cyclohexyl-2-benzothiazole sulfenamide (CBS, Vulkacit CZ of Bayer, Leverkusen, Germany): 0.6 part; 2-mercapto benzothiazole (MBT, Vulkacit Mercapto by Bayer): 0.6 part; zinc dibenzyl dithiocarbamate (Rhenogran ZBEC-70 of Rhein Chemie): 1.5 parts and zinc dicyanatodi-amine (Rhenogran Geniplex 80 of Rhein Chemie, Mannheim, Germany): 0.6 part. Rubber sheets (ca. 2 and 4 mm thick) were produced by compression molding at 160°C and 7 MPa pressure using a Satim press (Rion des Landes, France). The vulcanization time was adjusted by considering the time needed for the 90% crosslinking at  $T = 160^\circ\text{C}$ . The material characteristics were determined in the Institut für Verbundwerkstoffe (IVW) [13].

To be able to simulate the rolling friction of the rubber specimen, it is inevitable to determine the viscoelastic properties of the investigated material. Usually a dynamic mechanical thermal analysis

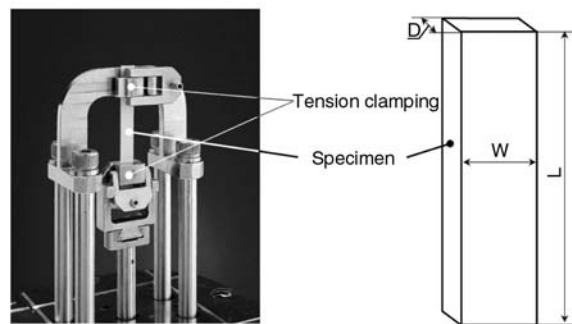


**Figure 4.** Picture of the tension grip with the specimen.

Note: The specimen dimension is the following:  
 $W = 10$  mm,  $L = 20$  mm,  $D \approx 2$  mm

(DMTA) test is carried out [14] where the frequency of the applied stress or strain and the temperature are changed in parallel. Another method is the stress relaxation measurement where a constant strain is applied on the specimen and the reaction force is detected as a function of the time. This measurement is repeated at different temperatures in a wide temperature range.

In our case the DMTA spectra was recorded on rectangular specimens (length  $\times$  width  $\times$  thickness =  $20 \times 10 \times \text{ca. } 2 \text{ mm}^3$ ) in tensile mode (cf. Figure 4) as a function of temperature (from  $-100$  to  $+100^\circ\text{C}$ ) and frequency at 1, 10 and 100 Hz using a Q800 device of TA Instruments (New Castle, DE, USA). The conditions set were: strain 0.01%, temperature step:  $5^\circ\text{C}$ , time for temperature equilibration at each step: 3 sec. According to the user's manual of the DMTA device, the storage ( $E'$ ), the loss moduli ( $E''$ ) and the loss factor ( $\tan\delta$ ) were calculated using Equations (12), (13) and (14):

$$E' = E^* \cdot \cos\delta \quad (12)$$

$$E'' = E^* \cdot \sin\delta \quad (13)$$

$$\tan\delta = \frac{E''}{E'} \quad (14)$$

where,  $E^*$  is the measured complex moduli of the sample and  $\delta$  is the phase angle which is calculated by Equation (15):

$$\delta = 2\pi \cdot f \cdot \Delta t \quad (15)$$

where  $f$  is the frequency of the dynamic excitation and  $\Delta t$  is the time delay between stress and strain.



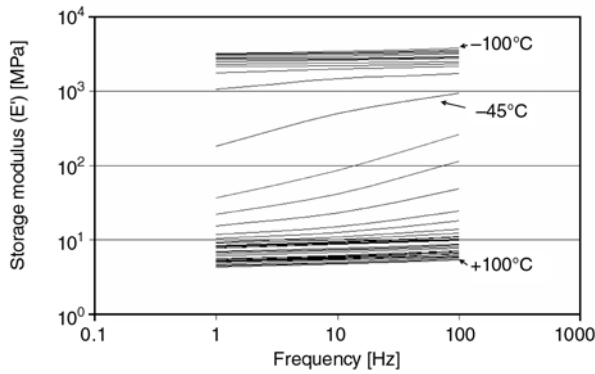


**Figure 5.** Storage modulus curves at different temperatures

As a result of the DMTA measurements, one can get the change of the storage ( $E'$ )-, and of the loss moduli ( $E''$ ) as well as of the loss factor ( $\tan\delta$ ) versus the applied frequency and versus the temperature. Figure 5 illustrates the change of the storage moduli ( $E'$ ) versus the frequency at different temperatures. In the figure, one can see that the highest moduli are measured at the lowest temperature, while the lowest moduli were measured at the highest temperature. The glass transition temperature ( $T_g$ ) can be clearly seen ( $-45^\circ\text{C}$ , cf. Figure 5), because the variation of the storage modulus is most intensive at  $T_g$ . The noteworthy temperatures are shown by arrows in Figure 5.

From the storage moduli curves, based on the Williams-Landel-Ferry (WLF) equation, we were able to create a storage modulus master curve (cf. Figure 6) [15]. The reference temperature was chosen for  $20^\circ\text{C}$ . Every other curve was shifted into the right direction with the right shift factor. From the master curve (cf. Figure 6) one can observe the change of the storage moduli versus the time in logarithmic scale.

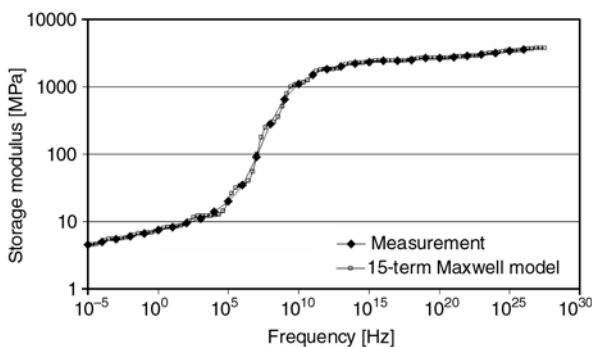


**Figure 6.** Storage moduli master curve of the EPDM rubber; reference temperature  $T_{ref} = 20^\circ\text{C}$

**Table 1.** Parameters of the fitted 15-term Maxwell-model

$E_0$ [MPa]	$3.7 \cdot 10^{+03}$	$E_\infty$ [MPa]	$4.5 \cdot 10^{+00}$
$t$ [sec]		Coefficients	
$t(1)$	$1.61 \cdot 10^{+03}$	$e(1)$	$2.83 \cdot 10^{-04}$
$t(2)$	$1.29 \cdot 10^{+01}$	$e(2)$	$3.12 \cdot 10^{-04}$
$t(3)$	$1.53 \cdot 10^{-01}$	$e(3)$	$4.45 \cdot 10^{-04}$
$t(4)$	$9.89 \cdot 10^{-04}$	$e(4)$	$1.03 \cdot 10^{-03}$
$t(5)$	$1.18 \cdot 10^{-06}$	$e(5)$	$6.09 \cdot 10^{-03}$
$t(6)$	$8.51 \cdot 10^{-09}$	$e(6)$	$6.74 \cdot 10^{-02}$
$t(7)$	$1.42 \cdot 10^{-10}$	$e(7)$	$2.22 \cdot 10^{-01}$
$t(8)$	$1.80 \cdot 10^{-12}$	$e(8)$	$1.90 \cdot 10^{-01}$
$t(9)$	$1.27 \cdot 10^{-14}$	$e(9)$	$1.12 \cdot 10^{-01}$
$t(10)$	$2.00 \cdot 10^{-16}$	$e(10)$	$5.07 \cdot 10^{-02}$
$t(11)$	$1.10 \cdot 10^{-19}$	$e(11)$	$6.91 \cdot 10^{-02}$
$t(12)$	$1.38 \cdot 10^{-22}$	$e(12)$	$4.59 \cdot 10^{-02}$
$t(13)$	$1.62 \cdot 10^{-24}$	$e(13)$	$8.62 \cdot 10^{-02}$
$t(14)$	$6.62 \cdot 10^{-26}$	$e(14)$	$6.76 \cdot 10^{-02}$
$t(15)$	$1.82 \cdot 10^{-27}$	$e(15)$	$7.87 \cdot 10^{-02}$

The mathematical description of the viscoelastic material behaviour is a complex task. With the help of the ViscoData software [16] we have fitted a 15-term Maxwell-model to the measured storage moduli master curve [17–19]. The detailed description of the Maxwell-parameter optimization is described in ref. [16]. The parameters of the Maxwell-model are summarized in Table 1. The storage modulus master curve of the DTMA measurements and the fitted master curve of the 15-term Maxwell-model can be seen in Figure 6. The listed Maxwell-parameters in Table 1 (relaxation time ( $t$ ) and dimensionless elastic moduli (coefficients of each Maxwell-element) are formulated specifically for the MSC.Marc FE software.

During the FE-simulation the 15-term Maxwell-model was combined with a two parameter Mooney-Rivlin material model. According to the MSC.Marc software the constants of the two term Mooney-Rivlin material law were calculated from the Young's modulus of the material measured at  $-100^\circ\text{C}$  (see  $E_0$  in Table 1) using Equations (16) and (17) [20, 21]:

$$E = 6(C_{10} + C_{01}) \quad (16)$$

$$4 = \frac{C_{10}}{C_{01}} \quad (17)$$

where,  $C_{10}$  – is the first Mooney-Rivlin parameter,  $C_{01}$  – is the second Mooney-Rivlin parameter,  $E$  – is Young's modulus.

Adjusted to the formulation of the FE software, the Mooney-Rivlin parameters were calculated based on the highest modulus of the EPDM rubber material. Using Equations (16) and (17), the calculated Mooney-Rivlin constants are the following:

$$C_{10} = 123 \text{ MPa},$$

$$C_{01} = 493 \text{ MPa}.$$

### 2.3. FE simulation of the rolling friction test

The model used in the simulation is shown in Figure 7. The rubber plate was defined as deformable body; the sphere was defined as a rigid body.

The dimension for the rubber plate is 37.6 mm×27.4 mm×4 mm, divided into 4256 elements (38×28×4). To increase the accuracy of the simulation and to decrease the computing time at the same time, the so called LOCAL ADAPTIVITY of MESH ADAPTIVITY was turned on, which was applied only to the deeper color elements shown in Figure 7. This method increases the number of elements in the chosen region when a given mean strain energy density was reached. In our case this value was 1.5 N/mm<sup>2</sup>. In that way the mesh will be changed during the simulation. The original and the automatically modified mesh can be seen in Figure 7. The first picture shows the rubber plate and the rigid sphere in its starting position. The second picture (front view) shows the sphere and rubber plate pushed together (the upper sphere mesh represents the original position of the sphere). The third picture shows the position of the sphere at  $t = T/2$ , where the re-meshed part of the rubber plate is also visible.

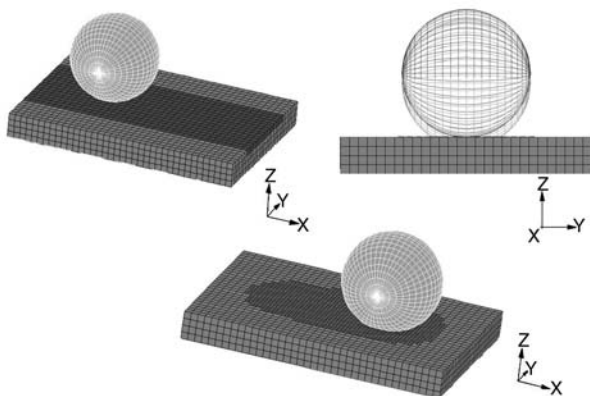


**Figure 7.** FE model at  $t = 0$  and at  $t = T/2$  for the Oscillating-RBOP friction simulation

The model was built up from 8-node solid Hermann type elements. There was no friction applied between the rigid sphere and the rubber plate. A rigid flat surface was fixed onto the bottom of the rubber plate. This rigid surface and the bottom of the rubber plate were glued together.

The load was applied by the prescribed displacement of the ball. The ball moved vertically ( $-z$  direction, cf. Figure 7) till a fixed position and pressed onto the rubber plate. The horizontal movement (prescribed velocity in direction  $x$ , cf. Figure 7) was applied to the rigid surface which was glued to the bottom of the rubber plate. Parallel to this horizontal reciprocating motion, an angular velocity was applied onto the rigid sphere. The driving time curves of the prescribed displacements and velocities are summarized in Figure 8. The time curve for the vertical movement of the rigid sphere (tc1) is linear. At  $t = 0$  s the value of the curve is zero. Subsequently it increases linearly until  $t = 1$  s, where it will be 1. After this the value remains constant until the end of the cycle ( $t = 31$  s). To ensure a normal force of 140 N, this value (1) will be multiplied with a proper displacement value (1 mm). The movement of the rigid surface at the bottom of the rubber plate and the angular velocity of the sphere can be driven by the same time curve (tc2). To prescribe the right velocity and right angular velocity, the values of the sinusoidal time curve will be multiplied by 1.47 mm/s for the horizontal velocity of the rubber plate, and by 0.21 rad/s for the angular velocity of the sphere. The value of the sinusoidal time curve (tc2) is zero from  $t = 0$  s to  $t = 1$  s. In this way, the velocity of the rubber plate will be (Equation (18)):

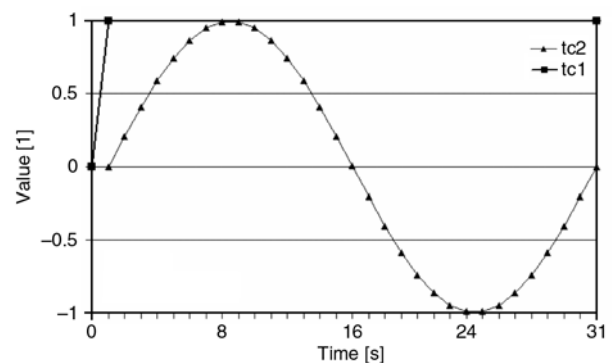


**Figure 8.** The driving time curves for the vertical displacement of the sphere (tc1), for the horizontal velocity of the rubber plate (tc2) and for the angular velocity of the sphere (tc2)

$$v(t) = 1.47 \sin\left(\frac{\pi}{15}(t-1)\right) \left[ \frac{\text{mm}}{\text{s}} \right] \quad (18)$$

while the angular velocity of the sphere can be described with Equation (19):

$$\omega(t) = 0.21 \sin\left(\frac{\pi}{15}(t-1)\right) \left[ \frac{\text{rad}}{\text{s}} \right] \quad (19)$$

if  $1 \text{ s} \leq t \leq 31 \text{ s}$ .

### Results of the simulation

Friction force, normal load and the calculated COF from the simulation are shown in Figure 9. The FE-calculated reaction force in vertical ( $z$ ) direction at the rigid sphere (cf. Figure 7) is defined as the normal force. The friction or tangential force is the reaction force in  $x$ -direction (cf. Figure 7) which is calculated at the rigid surface gluing to the rubber plate. One can see in Figure 9 that the direction of the friction force was reversed when the ball moved back and COF shows clear oscillating characteristic. The COF was calculated using Equation (11).

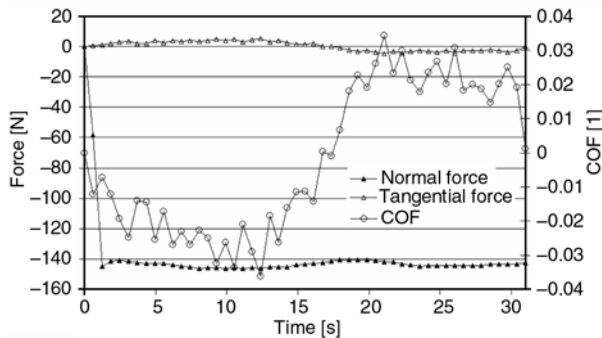


**Figure 9.** Friction force, normal force and coefficient of friction (COF) calculated by FE simulation

### Comparison of the measured and the FE simulated results

The measured and FE-calculated friction and normal forces are displayed in Figure 10. The curves from the simulation show a fair agreement with the experimental ones. It means that the FE simulation is usable to analyze the rolling process on the rubber plate and get a well quantitative description of the rolling friction.

A more spectacular comparison is the collation of the measured and FE-simulated COF results (cf. Figure 11). Although the measured and the FE cal-

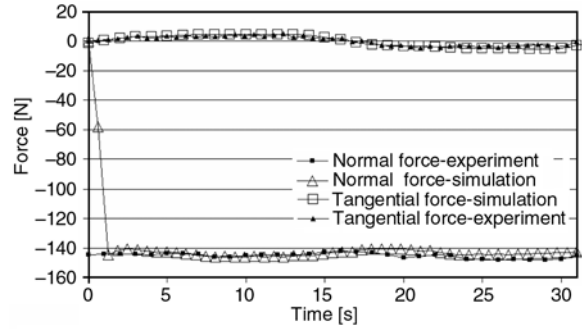


**Figure 10.** Comparison of friction force and normal loads between experiment and simulation in one cycle

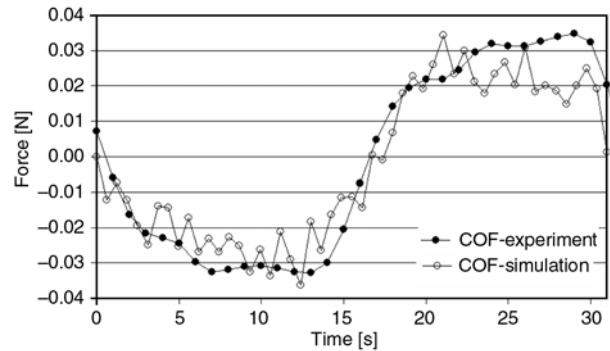


**Figure 11.** Comparison of COF between experiment and simulation in one cycle

culated values don't cover each other perfectly, the difference between the results is very small. One explanation may relate to the assumption of pure rolling, because in the contact area the micro-slip phenomenon [22] produces stick-slip around the pure rolling lines. At the same time, under lubricated conditions, this effect is not dominant.

### 3. Conclusions

This study describes a general method on how to consider the viscoelastic behavior of rubber materials. The description of the viscoelastic material behavior can be realized, for example, with proper number of Maxwell elements, by which the simulation results can well be adjusted to those of the experiments. Increasing number of elements in the FE-model and/or increasing number of steps during the simulation may further improve the accuracy of the calculations. However, both of the listed refinements can lead to a pronounced increase of the CPU time. Based on the results presented in this work the following conclusions can be made:



- The viscoelasticity of the EPDM material was determined by DMTA measurements successfully.
- The fitted 15-term Maxwell-model is able to describe the viscoelastic behavior of the investigated EPDM rubber.
- The FE method used is powerful tool to consider the viscoelastic properties of rubbery materials accordingly and to simulate their process of rolling friction.

## Acknowledgements

One of the authors, namely Tibor Goda, is a grantee of the János Bolyai Research Scholarship of the Hungarian Academy of Sciences. This work was performed in the framework of an integrated project of EU (KRISTAL; Contract Nr.: NMP3-CT-2005-515837; [www.kristal-project.org](http://www.kristal-project.org)).

## References

- [1] Tabor D.: The mechanism of rolling friction II. The elastic range. *Proceedings of the Royal Society of London, Series A: Mathematical and Physical Sciences*, **229**, 198–220 (1955).
- [2] Flom D. G., Bueche A. M.: Theory of rolling friction for spheres. *Journal of Applied Physics*, **30**, 1725–1730 (1959).
- [3] May W. D., Morris E. L., Atack D.: Rolling friction of a hard cylinder over a viscoelastic material. *Journal of Applied Physics*, **30**, 1713–1724 (1959).
- [4] Morland L. W.: Exact solutions for rolling contact between viscoelastic cylinders. *The Quarterly Journal of Mechanics and Applied Mathematics*, **20**, 73–106 (1966).
- [5] Knothe K., Wang G.: Zur Theorie der Rollreibung zylindrischer Kunststoffräder. *Konstruktion*, **41**, 193–200 (1989).
- [6] Morland L. W.: A plane problem of rolling contact in linear viscoelasticity theory. *Journal of Applied Mechanics*, **29**, 345–352 (1962).
- [7] Severin D., Lütkebohle H.: Rollreibung zylindrischer Laufräder aus Kunststoff. *Konstruktion*, **37**, 177–184 (1985).
- [8] Severin D., Kühlken B.: Tragfähigkeit von Kunststoffrädern unter Berücksichtigung der Eigenerwärmung Teil 1. *Konstruktion*, **43**, 65–71 (1991).
- [9] Severin D., Kühlken B.: Tragfähigkeit von Kunststoffrädern unter Berücksichtigung der Eigenerwärmung Teil 2. *Konstruktion*, **43**, 153–160 (1991).
- [10] Kulkarni S. M., Rubin C. A., Hahn G. T.: Elasto-plastic coupled temperature-displacement finite element analysis of two-dimensional rolling-sliding contact with a translating heat source. *Journal of Tribology*, **113**, 93–101 (1991).
- [11] Severin D., Qiao L.: The thermomechanical calculation of polymer roller with finite element method. in 'Advances in Computational Methods for Simulation' (ed.: Topping B. V. H.) Civil-Comp Press, Edinburgh 73–77 (1996).
- [12] Bederna C., Engst W.: Analyse des Eindruck-Rollwiderstandes bei Gurtförderern mit der Methode der Finiten Elemente. *Kautschuk und Gummi, Kunststoffe*, **51**, 690–699 (1998).
- [13] Karger-Kocsis J., Mousa A., Major Z., Békési N.: Dry friction and sliding wear of EPDM rubbers against steel as a function of carbon black content. *Wear*, **264**, 359–367 (2008).
- [14] Komalan C., George K. E., Kumar P. A. S., Varughese K. T., Thomas S.: Dynamic mechanical analysis of binary and ternary polymer blends based on nylon copolymer/EPDM rubber and EPM grafted maleic anhydride compatibilizer. *Express Polymer Letters*, **1**, 641–653 (2007).
- [15] Ferry J. D.: *Viscoelastic properties of polymers*. John Wiley and Sons, New York (1971).
- [16] <http://www.viscodata.de/> - accessed June 2007.
- [17] Aklonis J. J., MacKnight W. J.: *Introduction to polymer viscoelasticity*. Wiley Interscience Publication, New York (1983).
- [18] Ward I. M.: *Mechanical properties of solid polymers*. John Wiley and Sons, Chichester (1971).
- [19] Tschoegl N. W.: *The phenomenological theory of linear viscoelastic behavior*. Springer-Verlag, Berlin (1989).
- [20] MSC Software Corporation: *MSC.MARC Poroduct documentation, Help Volume A: Theory of user information, Version 2001* (2001).
- [21] Treloar L. R. G.: *The physics of rubber elasticity*. Oxford University Press, London (1975).
- [22] Johnson K. L.: *Contact mechanics*. Cambridge University Press, London (1985).

# Stimuli-responsive poly(ampholyte)s containing L-histidine residues: synthesis and protonation thermodynamics of methacrylic polymers in the free and in the cross-linked gel forms

M. Casolaro<sup>1\*</sup>, Y. Ito<sup>2,3</sup>, T. Ishii<sup>2</sup>, S. Bottari<sup>4</sup>, F. Samperi<sup>5</sup>, R. Mendichi<sup>6</sup>

<sup>1</sup>Dipartimento di Scienze e Tecnologie Chimiche e dei Biosistemi, Via Aldo Moro 2, Università degli Studi di Siena, I-53100 Siena, Italy

<sup>2</sup>RIKEN (The Institute of Physical and Chemical Research), Hirosawa 2-1, Wako, Saitama 351-0198, Japan

<sup>3</sup>Kanagawa Academy of Science and Technology, KSP East 309, Sakado 3-2-1, Takatsu-ku, Kawasaki, Kanagawa 213-0012, Japan

<sup>4</sup>Dipartimento di Fisica, Via Roma, Università degli Studi di Siena, I-53100 Siena, Italy

<sup>5</sup>Istituto di Chimica e Tecnologia dei Polimeri – Sez. Catania (CNR) – Dipartimento di Chimica, Università di Catania, Viale A. Doria 6, I-95125 Catania, Italy

<sup>6</sup>Istituto per lo Studio delle Macromolecole (CNR), Via E. Bassini 15, I-20133 Milano, Italy

Received 12 November 2007; accepted in revised form 14 January 2008

**Abstract.** Methacrylate-structured poly(ampholyte)s were synthesized in the homopolymer and copolymer forms starting from the *N*-methacryloyl-L-histidine (MHist) and the *N*-isopropylacrylamide (NIPAAm). They were also obtained in the cross-linked (hydrogel) form, showing a close thermodynamic behaviour as that shown by the corresponding soluble free polymer analogues. Viscometric data revealed that the minimum hydrodynamic volume of the polymer at its isoelectric point (pH 5) shifted to lower pHs as the NIPAAm content increased, and beyond a critical low MHist content the reduced viscosity decreased, even at low pHs. The phenomenon was attributed to hydrophobic forces between the isopropyl groups outweighing the repulsive electrostatic interactions of the polymer in the positively charged form. A similar behaviour was shown by the corresponding hydrogel. The latter also revealed a different phase transition phenomenon induced by external stimuli (temperature, pH, ionic strength, electric current) when compared to the acrylate-structured analogues. The polyMHist, as well as the corresponding monomer, was found for two days to be non toxic against the mouse osteoblasts (MC3T3-E1).

**Keywords:** biocompatible polymers, smart polymers, polymer gels, protonation thermodynamics, polyampholytes

## 1. Introduction

Vinyl compounds carrying aminoacid residues have been widely synthesized to obtain functional polymers for practical purposes [1]. The presence of the carboxyl [2] or the amino [3] functionality made these polymers sensitive to the pH in a range that was closely related to their basicity constants. Moreover, the presence of the hydrophilic amido

functionality and the hydrophobic isopropyl groups in the side chain made these polymers also sensitive to the temperature [4, 5].

Recently, new vinyl acrylate polymers based on the L-histidine residues have been developed in order to have poly(ampholyte)s responding in different pH-ranges [6]. The imidazole-containing methacrylate polymers with different functions were investi-

\*Corresponding author, e-mail: [casolaro@unisi.it](mailto:casolaro@unisi.it)  
© BME-PT and GTE

gated in the catalytic activities towards the solvolyses of a series of activated phenyl esters [7]. Besides the buffering capacity of proteins in the physiological pH range, the imidazole group is also able to form coordination compounds with metal ions [8]. These compounds are considered as models for the understanding of the biological activity of proteins involved in fatal disorders such as the Alzheimer's disease or the prion infection [9, 10]. Synthetic polymers containing the imidazole functionality have recently been reported as thermosensitive, reusable displacers for immobilized metal affinity chromatography of proteins [11, 12]. The incorporation of the imidazole functionality in the highly branched poly(*N*-isopropylacrylamide), the polyNIPAAm, showed interest as a thermally responsive 'smart' polymer for the purification of a histidine-tagged protein fragments [13, 14]. Moreover, the absence of toxicity makes these ampholyte polymers useful candidates in the development of loosely cross-linked hydrogels to be used as injectable polymer scaffolds for tissue engineering applications [15]. The non toxic effect of the poly(MHist) against the osteoblast cells enables the corresponding hydrogels to be tailored in medical treatment for more efficient routes in the administration of pharmaceutical compounds, especially metal-based drugs [16], and improves the absorption of loaded amino-bisphosphonates (BPs) in the bone resorption process [17, 18]. In the latter case, the poor absorption of bisphosphonates via the paracellular route may be improved by a slow releasing process of BPs loaded into the hydrogel. Previous reported papers described the thermodynamic behaviour of acrylate polymers with the L-histidine residues in the free and in the cross-linked forms [6]. Copolymers with the *N*-isopropylacrylamide were also prepared to obtain multiple stim-

uli-sensitive hydrogels for biomedical applications [19, 20]. In fact, besides the pH, they were sensitive to the temperature, the electric potential, the salt-type and the ionic strength.

Following our interest in these kind of polymers, we thought to study the methacrylate-structured polymer analogues because, as a rule, the solution behaviour of acrylate compounds differs to some extent from that of the corresponding methacrylate [21]. Thus, the aim of this paper is devoted to the protonation behaviour study of the synthetic methacrylic poly(ampholyte)s containing the L-histidine residues, the poly(MHist) (Figure 1).

A series of copolymers with a variable amount of NIPAAm was studied in order to clarify their thermodynamic behaviour in view of the potential applications of the corresponding hydrogels. The thermodynamic study of either the soluble or the cross-linked polymers allowed to evaluate the basicity constants along with the enthalpy and entropy changes during the protonation of the imidazole nitrogen. Moreover, the results of the swelling properties of three different cross-linked hydrogels were reported along with their protonation behaviour. They were strictly compared to the previously reported acrylate analogues [6, 19].

The hydrophilic behaviour of the non toxic poly(MHist) allowed the preparation of a new type of copolymer for nonbiofouling surfaces [22]. The polystyrene hydrophilization with poly(MHist) and some of its copolymers was in fact shown to be higher than that of the BSA (Bovine Serum Albumin).

## 2. Experimental section

### 2.1. Materials

L-Histidine (98%), methacryloyl chloride (97%) and 2,2'-azoisobutironitrile (AIBN, 98%) were purchased from Wako Pure Chemical Industries. Ammonium peroxy-disulfate (APS, 98%) and *N,N,N',N'*-tetramethylethylenediamine (TEMED) were from Kanto Chemical Co., Inc. *N,N'*-ethylenebis-acrylamide (EBA, 98%) and triethylamine (TEA, 99.5%) were from Fluka Co. The AIBN was recrystallized from methanol and all the other reagents were used as received. The *N*-isopropylacrylamide (NIPAAm, Wako Co.) was purified by recrystallization from *n*-hexane and then dried in vacuo. Buffer solutions (tris, phosphate, acetate)

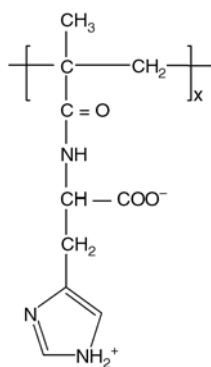


**Figure 1.** Structure of the monomer unit of poly(MHist)



were prepared at a concentration of 0.01M in twice-distilled water and in 0.15M NaCl. The sodium chloride salt was of analytical grade from Fluka Co.

## 2.2. Syntheses

### *Synthesis of MHist*

The *N*-methacryloyl-L-histidine, MHist, was prepared according to the previously reported synthetic routes [22, 24]. To an aqueous solution of L-histidine (5.0 g, 32 mmol) and sodium hydroxide (1.6 g, 40 mmol) in twice-distilled water (20 ml), the methacryloyl chloride (3.67 ml, 38 mmol), diluted in dioxane (10 ml), was added dropwise. During addition, the reaction mixture was kept under 5°C by the external ice-bath cooling, and then the temperature was raised to room temperature for 1 hour. After removing the dioxane by a rotary evaporator, the mixture was acidified to pH 2 with concentrated hydrochloric acid and extracted with ether. The aqueous layer was adjusted to pH 5 and concentrated in vacuo to obtain crude MHist. The crude monomer was purified by repeated precipitations from ethanol to acetone and dried in vacuo.

### *Synthesis of polyMHist*

The poly(*N*-methacryloyl-L-histidine), polyMHist, was synthesized by a conventional free-radical polymerization [25]. The polymer was obtained as follows. A mixture of MHist (0.5 mmol) in ethanol (20 ml) containing AIBN (0.05 mmol) was purged with N<sub>2</sub> gas and then allowed to react under nitrogen atmosphere at 70°C for 20 h. The obtained polymer was purified by using a dialysis cellophane tubing-seamless (MWCO 3500 g/mol) in twice-distilled water for 2 days and then lyophilized to give a white powder.

### *Synthesis of poly(MHist-co-NIPAAm)*

The poly(*N*-methacryloyl-L-histidine-*co-N*-isopropylacrylamide), poly(MHist-*co*-NIPAAm), copolymers were synthesized by the conventional free-radical polymerization reaction. Three different samples of the NIPAAm/MHist copolymers with decreasing amounts of MHist, namely co-3, co-2, and co-1, were synthesized. The mixture of MHist and NIPAAm with different molar ratio (the

total mole was adjusted to 20 mmol) in twice-distilled water (40 ml), and containing 30 µl of TEMED 10 mM solution, was purged with N<sub>2</sub> gas and then 100 µl of APS 5 mM solution were added and allowed to react under nitrogen atmosphere at room temperature for 18 h. The polymer obtained was purified by using a dialysis cellophane tubing-seamless (MWCO 3500 g/mol) in twice-distilled water for 2 days and then lyophilized to give a white powder.

### *Synthesis of hydrogels*

Three hydrogel samples containing only MHist (MH2) and a mixture of NIPAAm/MHist (CMH2, CMH10), were prepared according to a previously reported procedure [6, 19, 26]. The two poly(MHist-*co*-NIPAAm) hydrogels, at a NIPAAm/MHist molar ratio of 12, were synthesized by cross-linking with 2 (CMH2) and 10 (CMH10) mol% of EBA. The hydrogel MH2 was obtained only with the MHist cross-linked with 2 mol% of EBA. The synthesis was carried out in a glass tube, containing the monomer solution at a total concentration of 15 wt%, after their degassing under vacuum and under a nitrogen atmosphere. The reaction mixture was kept at room temperature for 24 h even if the gelation was observed within 4 h. Afterwards, the gel samples were removed, thoroughly washed with twice-distilled water for two weeks, and then slowly dried at r.t. to a constant weight. In all cases, the yield was more than 90%.

## 2.3. Spectroscopic and molecular characterization

The molecular characterization of polyMHist homopolymer and related copolymers was performed by a multi-angle laser light scattering (MALS) Dawn DSP-F photometer from Wyatt (Santa Barbara, CA, USA) on-line to a size exclusion chromatography (SEC) system. The SEC-MALS experimental conditions were the following: 0.2M NaCl + 0.1M Tris buffer pH 8.0 as mobile phase, two TSKgel PW G4000 and G3000 columns from Tosoh Bioscience (Stuttgart, D), 35°C of temperature, 0.8 ml/min of flow rate and 150 µl of injection volume. The wavelength of the MALS He-Ne laser was 632.8 nm. The light scattering signal was simultaneously detected at fifteen

scattering angles ranging in the solvent from  $14.5^\circ$  to  $151.3^\circ$ . The calibration constant was calculated using toluene as standard assuming a Rayleigh Factor of  $1.406 \cdot 10^{-5} \text{ cm}^{-1}$ . The angular normalization was performed by measuring the scattering intensity of a concentrated solution of a BSA globular protein in the mobile phase assumed to act as an isotropic scatterer. The refractive index increment,  $dn/dc$ , of polyMHist homopolymer and copolymers with respect to the used solvent was measured by a KMX-16 differential refractometer from LDC Milton Roy (Riviera Beach, FL, USA). The  $dn/dc$  values were: polyMHist: 0.190 ml/g, co-1: 0.175 ml/g, co-2: 0.177 ml/g, co-3: 0.182 ml/g. Proton NMR spectra of the monomer and the polymers were recorded in  $D_2O$  on a 400 MHz spectrometer (JEOL EX400, Japan). The FT-infrared spectra of the same compounds were recorded on a FTS 6000 Biorad spectrophotometer. The MALDI-TOF mass spectra were recorded in the reflection mode, using a Voyager-DE STR instrument (Perseptive Biosystem) mass spectrometer, equipped with a nitrogen laser ( $\lambda = 337 \text{ nm}$ , pulse width = 3 ns), working in a positive ion mode. The accelerating voltage was 25 kV, the grid voltage and the delay time (delayed extraction, time lag) were optimized for each sample to achieve the higher mass resolution (FWHM). The laser irradiance was maintained slightly above threshold. The samples used for the MALDI analyses were prepared as follows: 10  $\mu\text{l}$  of polymer solution (10 mg/ml in  $H_2O$  or  $C_2H_5OH$ ) were mixed with 30  $\mu\text{l}$  of HABA solution (0.1M in  $C_2H_5OH$ ), then 1  $\mu\text{l}$  of each analyte/matrix mixture was spotted on the MALDI sample holder and slowly dried to allow the analyte/matrix co-crystallization. A mass resolution of about 4000 Da was obtained in the best MALDI mass spectra recorded.

## 2.4. Viscometric measurements

Viscometric measurements were carried out with an AVS 310 automatic Schott-Gerate viscometer at  $25^\circ\text{C}$  on a dilute aqueous polymer solution. The solution was freshly prepared by weighing and dissolving a known amount of the polymeric compound (MHist content, mmol: polyMHist, 0.2154; co-3, 0.2258; co-2, 0.2258; co-1, 0.1368) in 25 ml of 0.15M NaCl containing a measured volume of standard 0.1M NaOH solution. A standard 0.1M HCl solution was stepwise delivered by a Metrohm

Multidosimat piston buret. The evaluation of the pH, at each neutralization step, was made with the program Fith [27] from the  $\log K^\circ$  and the  $n$  values of the corresponding polymer and copolymers (see basicity constants, section 3.2). Viscometric data at different temperatures were obtained on polymer solutions at three different significant pHs (9, 5, and 2). A weighed amount of copolymer (co-1, 336 mg; co-2, 282 mg; co-3, 97.9 mg) was dissolved in 25 ml of 0.15M NaCl and the pH was controlled by adding the stoichiometric quantity of standard NaOH or HCl solutions. The temperature was monitored by the Haake DC10 thermostat (Thermo Electr. Corp.).

## 2.5. Potentiometric measurements

The acid-base potentiometric measurements were carried out in aqueous media at  $25^\circ\text{C}$ , following a previously reported procedure [6, 19]. A TitraLab 90 titration system (from Radiometer Analytical), consisting of three components (Titration Manager, TIM900; high-precision autoburet, ABU901; and the sample stand) and connected to the TimTalk 9 (a Windows based software, for remote control) was used to record the potentiometric titration data of the monomer, the polymers, and the hydrogel. All the titrations were carried out in a thermostated glass cell filled with 100 ml of 0.15M NaCl in which a weighed quantity of solid material and a measured volume of standard HCl solution were dispersed by magnetic stirring, under a presaturated nitrogen stream. Forward titrations were carried out with a standard 0.1M NaOH solution and reliable results were obtained for the back-titration with a standard 0.1M HCl solution. Unlike the monomer and the polymers, which, being soluble over the whole pH-range investigated were titrated at the equilibration time of 300 s for each titration step (0.04 ml), the MH2 roughly and finely crushed hydrogel sample (0.1205 mmol) was titrated at different equilibration times (1500 and 3000 s). In the case of the roughly crushed hydrogel, hysteresis loops were obtained during the forward and backward titrations with NaOH and HCl standard solutions, respectively; the finely crushed hydrogel improved a faster response in reaching equilibrium conditions. A typical potentiometric titration curve for the soluble compounds is reported in Figure 2,

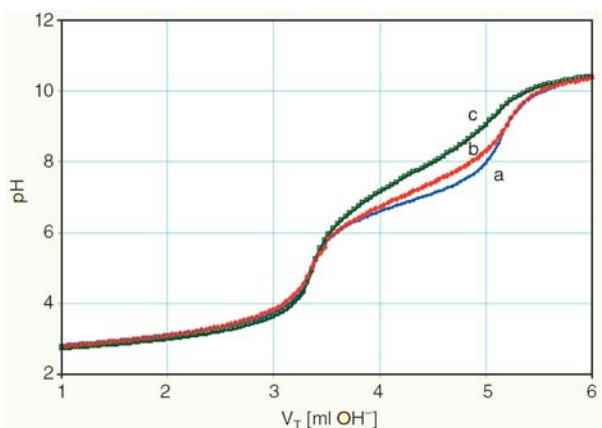


**Figure 2.** Potentiometric titration curves (pH in relation to the volume of standard NaOH 0.1084M) of MHist (a, 0.1997 mmol), co-3 (b, 0.2090 mmol), and polyMHist (c, 0.1864 mmol) in 0.15M NaCl at 25°C

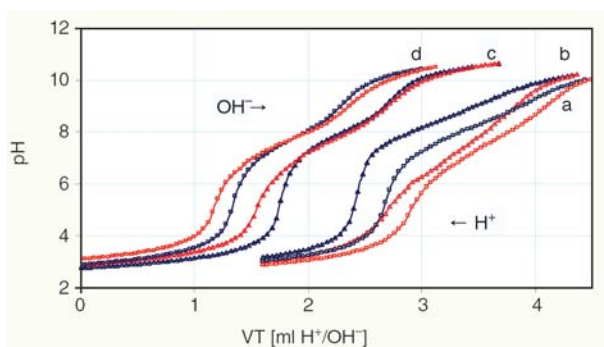


**Figure 3.** Potentiometric titration curves of the MH2 hydrogel (a, b: roughly crushed; c, d: finely crushed) protonation in 0.15M NaCl at 25°C. Equilibration time for each titrant addition (0.04 ml of 0.1205M NaOH forward, blue curves; 0.04 ml 0.1123M HCl backward, red curves): 1500 s (triangle) and 3000 s (square)

while Figure 3 shows the titration curves of the MH2 hydrogel in the rough and fine crushing state. The basicity constant ( $\log K$ ) values of the monomer were evaluated with the Superquad program [28] taking into account all the points of three independent potentiometric titration curves (ca. 300 data points) carried out with a different amount of ligand (0.13–0.20 mmol). On the other hand, the basicity constants of the free (polyMHist, 0.15–0.19 mmol; co-3, 0.21 mmol; co-2, 0.23 mmol; co-1, 0.13 mmol) and the cross-linked polymers (MH2, 0.12–0.15 mmol) were evaluated with the AppaK program [27]. In these cases each potentiometric titration was computed to evaluate both the  $\log K$ s into a separated pH-buffered region. In all cases, the  $E^\circ$  calibrations were performed before

and after each titration with the standard Tris grade-reagent. Three replicates were averaged and their standard deviations calculated.

## 2.6. Calorimetric measurements

Calorimetric measurements were carried out in aqueous solution at 25°C, following a previously reported procedure [6], by the use of a Tronac titration calorimeter (mod 1250) operating in the isothermal mode. A stainless steel reaction vessel was filled with 25 ml of 0.15M NaCl (containing a measured amount of standard NaOH solution) in which a weighed quantity of solid material (MHist content, mmol: monomer MHist, 0.12–0.24; polyMHist, 0.14–0.22; co-3, 0.13–0.23; co-2, 0.13–0.23; co-1, 0.14) was dissolved and titrated with a standard 0.1M hydrochloric acid solution at a BDR (buret delivery rate) of 0.0837 ml/min through a Gilmont buret. The titrations were performed at high and low MHist content for the protonation of the only imidazole nitrogen and for the protonation of both the imidazole and the carboxylate groups, respectively. Before and after each experiment, the chemical calibration with Tris/HCl and the corrections for the heats of the titrant dilution were made. All the experiments were automatically controlled by the Thermal program (from Tronac, Inc.) which was renewed to operate through a NI-DAQ driver software in Windows (from National Instruments). The graphical programming language LabVIEW was used to create the application. The evaluation of the enthalpy change ( $-\Delta H^\circ$ ) values was obtained with the Fith program [27] by taking into account the linear dependence of the  $\log K$ s on  $\alpha$  (the degree of protonation) for the polymeric compounds. The entropy change ( $\Delta S^\circ$ ) values were calculated. The results of at least two replicates were averaged.

## 2.7. Swelling measurements

Swelling measurements of the hydrogels (MH2 and CMH2) were carried out in different conditions of pH and temperature, at equilibrium conditions. The equilibrium degree of swelling (EDS) was measured every 24 h because the kinetic DS/time curves reached a plateau in these conditions. A weighed sample of dry gel (MH2, 30.4 mg; CMH2, 28.7 mg), contained in a Strainer cell (100  $\mu$ m pore size), was immersed in a thermostated glass cell filled with

100 ml of aqueous solution at the desired pH, under stirring by the magnetic bar. The temperature probe and the pH glass electrode were controlled by the TimTalk 9 software. The EDS in relation to pH for both the hydrogels was monitored at different pHs of the proper buffer. The EDS in relation to the sodium chloride concentration was monitored at 25°C and in Tris/HCl buffered solution at pH 9.02 by the daily addition of weighed portions of the salt to produce the desired final concentration. The effect of the temperature for the CMH2 gel was monitored in buffered solutions at three different pHs (9.02, 5.01, and 3.07) and at a constant ionic strength (0.15M NaCl). In all cases, the gel sample and its container were removed from the bath at intervals, blotted with a tissue paper to remove any surface droplets, and weighed (wet weight,  $W_{wet}$ ). The procedure was repeated at 12–24 h intervals. The EDS value was calculated by the relation:  $EDS = (W_{wet} - W_{dry})/W_{dry}$ , where  $W_{dry}$  is the weight of the dry gel sample.

## 2.8. Electric measurements

Hydrogels contraction measurements were carried out at 25°C according to the previously reported procedure [19]. A constant voltage was applied between two gold electrodes (16 mm diameter) in a cylindrical nylon cell, and with a mobile cathode positioned on the gel sample. The hydrogels (CMH2 and CMH10) were swollen in a 0.01M Tris/HCl buffer solution at pH 9, then a specimen of 5 mm thick was cut and used for contractile experiments for a period of 10 min. Under the application of the electric field, each hydrogel change in the thickness was controlled by a digital comparator that was sensitive to displacements of  $10^{-2}$  mm (Digimatic indicator 266-2745, Mitutoyo). All the experiments were controlled through a NI-DAQ driver software in Windows (from National Instruments) and the graphical programming language LabView was used to create the application. The gel deformation was recorded at intervals of 1 s under the applied voltage (2.5, 5.0, and 7.0 V) by a dc power supply.

## 2.9. Evaluation of cytotoxicity

### Cell culture

Mouse osteoblast cells (MC3T3-E1) obtained from the RIKEN Cell Bank (Tsukuba, Ibaraki, Japan) were cultured to confluence in culture dishes (Corning Co., Ltd.) containing a medium composed of Minimum Essential Medium, alpha modified (MEM- $\alpha$ , Kohjin Bio Co. Ltd., Japan) supplemented with 10% fetal bovine serum (FBS, BioWest, France) in a fully humidified atmosphere with a volume fraction of 5% CO<sub>2</sub> at 37°C.

### Cytotoxicity evaluation

The cell viability was evaluated by using a Cell Counting Kit [29] (WST-1 method, Dojindo Lab., Tokyo, Japan). Briefly, after the MC3T3-E1 cells reached confluency, they were trypsinized and seeded at  $1 \cdot 10^4$  cells/cm<sup>2</sup> onto 96-well multiplate (Corning Co., Ltd.) then incubated for 2 days in a humidified atmosphere containing 5% CO<sub>2</sub> at 37°C. After removing the cultured medium, 100  $\mu$ l of fresh culture medium supplemented with 10% [v/v] FBS and containing each MHist sample were added to each well and allowed to stand for in a fully humidified atmosphere with a volume fraction of 5% CO<sub>2</sub> at 37°C. After 24 h of incubation, 10  $\mu$ l of WST-1 reagent were added to each well and the wells incubated for 2 h at 37°C; then 10  $\mu$ l of 0.1N HCl aqueous solution were added to each well to stop the reaction. The absorbance of aliquot of the solution was measured at 450 nm, with a reference of the absorbance at 655 nm, with a multiplate reader (Bio-Rad model 650, Tokyo, Japan). The results were expressed as viability [%] related to a control containing no MHist samples. The error bar means standard error of four experiments.

## 3. Results and discussion

### 3.1. Syntheses and characterization

#### Monomer

The *N*-methacryloyl-L-histidine (MHist) was prepared according to the synthetic route to obtain vinyl monomers from  $\alpha$ -aminoacids [2, 4–6, 22–24]. The reaction between methacryloyl chloride and L-histidine at low temperature (< 5°C) allowed to obtain a white powder freely soluble in water. The



**Table 1.** Main IR frequencies [ $\text{cm}^{-1}$ ] and protonNMR chemical shifts ( $\delta$  [ppm]) of *N*-methacryloyl-L-histidine

	Assignments
IR	1709 ( <i>w</i> ) C=O stretch of COOH group;
	1656 ( <i>s</i> ) Amide I; 1620 ( <i>sh</i> ) C=C;
	1600 ( <i>vs</i> ) Imidazole group;
	1534 ( <i>s</i> ) Amide II; 1437 ( <i>w</i> ) $-\text{CH}_3$ ;
	1393 ( <i>vs</i> ) C=O stretch of $\text{COO}^-$
	<i>w</i> : weak; <i>s</i> : strong; <i>sh</i> : shoulder; <i>vs</i> : very strong
$^1\text{H}$ NMR	1.75 ( <i>s</i> , 3H $\text{CH}_3\text{C}(=\text{CH}_2)\text{H}-$ );
	2.95–3.23 ( <i>m</i> , 2H $-\text{CH}_2-$ Imidazole);
	4.41–4.46 ( <i>q</i> , H $-\text{NHCH}(\text{COOH})\text{CH}_2-$ );
	5.31–5.52 ( <i>m</i> , 2H $\text{CH}_2=\text{C}(\text{CH}_3)-$ );
	7.12 ( <i>s</i> , 1H Imidazole, $-\text{C}=\text{CHN}=-$ );
	8.44 ( <i>s</i> , 1H Imidazole, $-\text{N}=\text{CHNH}-$ )

potentiometric purity revealed that the imidazole nitrogen was protonated more than 92 wt%, while the carboxyl group was mostly in the ionized form. The expected structure was confirmed by the  $^1\text{H}$  NMR and FT-IR spectroscopy. Table 1 summarizes the observed main infrared frequencies and the chemical shifts of the MHist.

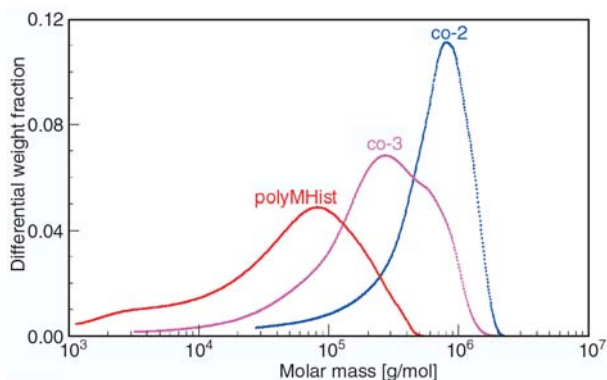
Unlike the previously reported acrylate monomer, the *N*-acryloyl-L-histidine (Hist), the MHist showed the presence of a great amount of amphoteric molecular species [6]. The lower chemical shifts of the imidazole protons and the very strong band at  $1600\text{ cm}^{-1}$  are indicative of the prevailing zwitterionic molecules [19]. This is also supported by the greater basicity constant.

### Polymers

The *N*-methacryloyl-L-histidine, MHist, was used as the starting pH-sensitive monomer to synthesize free and cross-linked polymers together with the thermoresponsive *N*-isopropylacrylamide, NIPAAm, by a radical polymerization [4–6]. Unlike the poly(*N*-methacryloyl-L-histidine), the polyMHist, that was obtained in ethanol and using the AIBN initiator, the three copolymers with NIPAAm (co-3, co-2, and co-1), along with the three hydrogels (MH2, CMH2, and CMH10), were obtained in water solution by the use of the APS initiator [19–26]. While the free polymers remained in solution during the polymerization process, the cross-linked compounds gelified within 4 hrs. Compared to the acrylate analogue [6, 19], the polymerization of the methacrylate MHist to the corresponding

**Table 2.** Results of molecular characterization of polyMHist homopolymer and copolymers by SEC-MALS

Sample	MHist content [weight %]	dn/dc [ml/g]	$M_p$ [kg/mol]	$M_w$ [kg/mol]	$M_w/M_n$
PolyMHist	96.5	0.190	81.4	83.2	3.2
co-1	9.1	0.175	481.3	–	–
co-2	17.9	0.177	792.2	831.6	2.0
co-3	51.5	0.182	304.0	380.0	2.2

**Figure 4.** Comparison of the differential molar mass distribution of polyMHist homopolymer, co-2 and co-3 copolymers by SEC-MALS

homopolymer gave rise to a relatively lower number-average molecular weight, while the polydispersity index remained quite high, even after the dialysis process (Table 2).

This may be ascribed to the different solvent used in the polymerization procedure [25]. Figure 4 shows the comparison of the differential molar mass distribution (DMM) of the polyMHist homopolymer and the two copolymers (co-2 and co-3) by SEC-MALS.

Unfortunately, the chromatographic elution of the copolymers depends on the NIPAAm content. In particular, Figure 4 does not report the DMM of co-1 copolymer because the chromatogram presents a long tail in consequence of a very high NIPAAm content (about 90%). Consequently, for the co-1 copolymer Table 2 reports only the peak molar mass  $M_p$ . It is important to note that the molar mass values from MALS are absolute and do not depend on an eventual non-steric chromatographic elution. As a result the  $M_w$  and  $M_p$  molar mass values are substantially correct, while the polydispersity index  $M_w/M_n$  (see Table 2) and in general the DMM shape (see Figure 4) are only approximate.

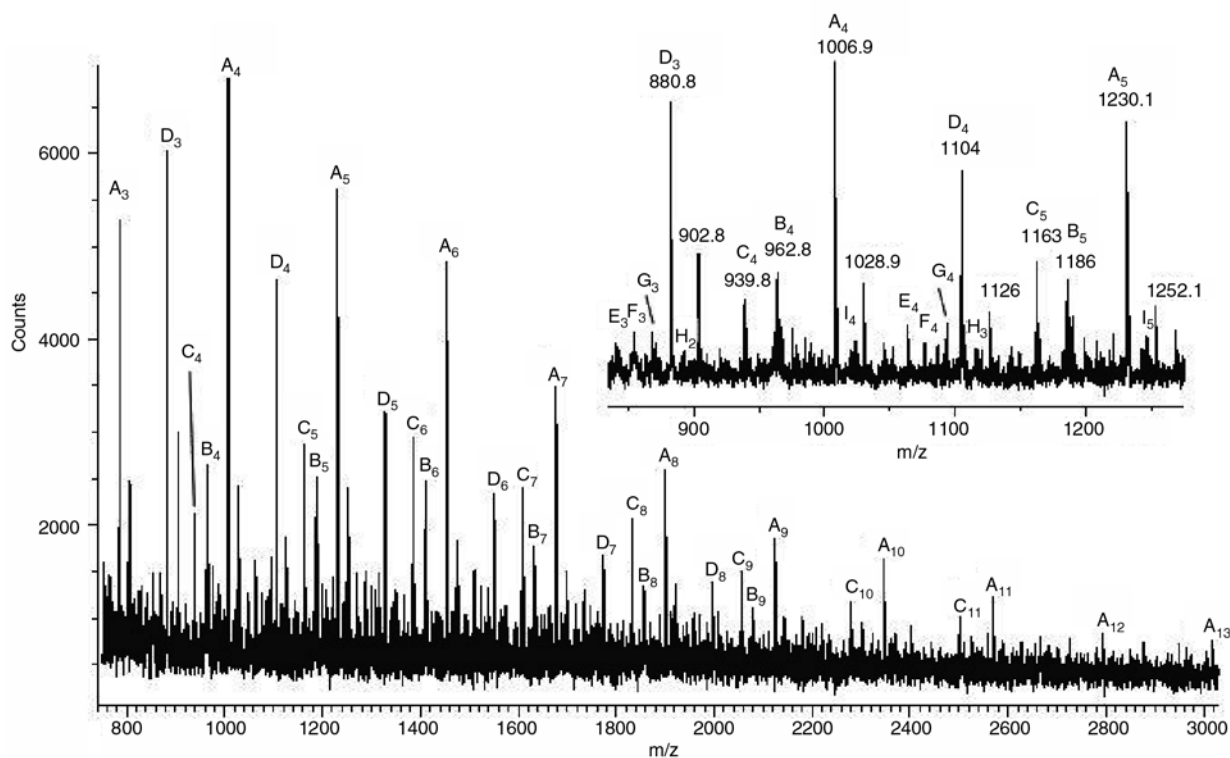
**Table 3.** Molar composition of vinyl polymers containing L-histidine residues

Compd	MHist purity, [mol%]	
	Potentiometry	Proton NMR
PolyMHist	96.5	100.0
co-3	35.0	36.5
co-2	10.0	8.2
co-1	4.9	3.5

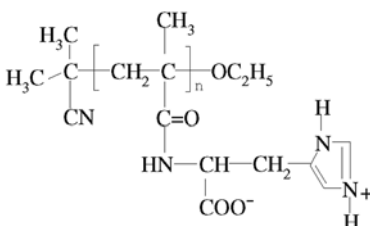
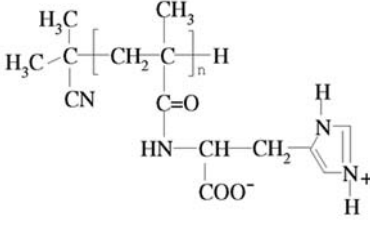
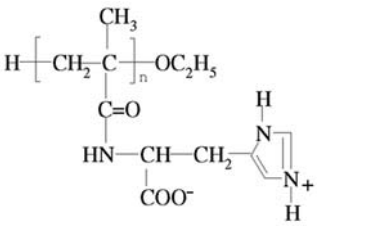
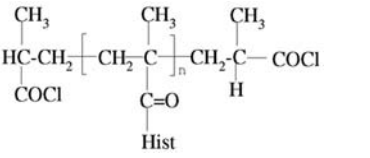
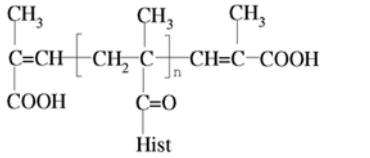
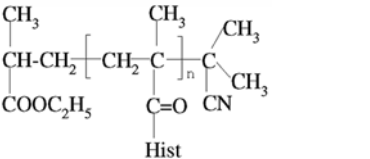
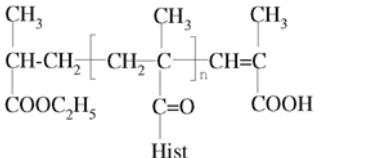
The copolymers with NIPAAm produced higher molecular weight compounds that in general increased with the NIPAAm content. This led also to a greater viscosity in a wide range of pH (see the protonation section). However, in all cases the  $^1\text{H}$  NMR spectra showed that the chemical shifts of the vinyl double bond (5.31–5.52 ppm) completely disappeared, and the broad lines were consistent with the presence of a slowly tumbling macromolecular species in  $\text{D}_2\text{O}$  solution. The FT-IR spectra confirmed the total conversion of the monomers into the corresponding polymers. The band intensity at  $1599\text{ cm}^{-1}$  present in the polyMHist decreased as the NIPAAm unit increased in the copolymers. In the meantime, the new band of the NIPAAm Amide I increased and slightly shifted to greater wavenumbers, in the same way as happened for the  $1459\text{ cm}^{-1}$  band of the isopropyl group [31, 32].

Based on the NMR and potentiometric results, the relative comonomer MHist/NIPAAm incorporation level reflected the comonomer feed ratio. Table 3 shows that the amount [mol%] of titrated MHist in the polymers is in agreement with that evaluated by the proton signals of the methyl groups.

These results suggest a presumably total conversion of the monomers into the corresponding polymers, being the reaction of radical type. A random distribution of MHist units in copolymers with NIPAAm may be expected because the basicity constants and the  $n$  values showed a decreasing trend (see protonation section). When both the monomers had a close structure, a random distribution of charged units was observed in the copolymer. This reflects lower electrostatic effects due to a lower content of charged groups. [25, 30, 32]. Moreover, the hydrogels were obtained at the fixed amount of cross-linking agent (EBA, 2 and 10 mol%) and with a NIPAAm/MHist molar ratio of 0 and 12, in order to have, respectively, a greater content of pH- or temperature-responsive comonomer content. After the polymerization procedure, the samples were slowly dried at r.t. for a week and then under vacuum. As expected, the acid/base potentiometric titrations of the gel MH2 revealed that the imidazole nitrogen content of

**Figure 5.** Positive ions MALDI-TOF mass spectrum of the polyMHist sample

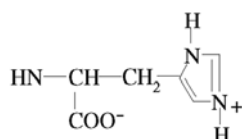
**Table 4.** Structural assignments of peaks displayed in the MALDI-TOF mass spectrum of the polyMHist

Structures <sup>a</sup>	[MH] <sup>+</sup> (n) <sup>b</sup>	[M+Na] <sup>+</sup> (n) <sup>b</sup>
A= 	783.7 (3)	805.7 (3)
	1006.9 (4)	1028.9 (4)
	1230.1 (5)	1252.1 (5)
	1453.3 (6)	1475.3 (6)
	1676.5 (7)	1698.5 (7)
	1899.7 (8)	1921.7 (8)
	2122.9 (9)	2144.9 (9)
	2346.1 (10)	2368.1 (10)
	2569.3 (11)	2591.3 (11)
	2792.5 (12)	2814.5 (12)
	3015.7 (13)	3037.7 (13)
B= 	962.8 (4)	984.8 (4)
	1186.0 (5)	1208.0 (5)
	1409.2 (6)	1431.2 (6)
	1632.4 (7)	1654.4 (7)
	1855.6 (8)	1877.6 (8)
	2078.8 (9)	2100.8 (9)
	2302.0 (10)	2324.0 (10)
	2525.2 (11)	2547.2 (11)
	2748.4 (12)	
	2971.6 (13)	
C= 	939.8 (4)	961.8 (4)
	1163.0 (5)	1185.0 (5)
	1386.2 (6)	1408.2 (6)
	1609.4 (7)	1631.4 (7)
	1832.6 (8)	1854.6 (8)
	2055.8 (9)	2077.8 (9)
	2279.0 (10)	2301.0 (10)
	2502.2 (11)	2524.2 (11)
	2725.4 (12)	2747.4 (12)
	2948.6 (13)	2970.6 (13)
D= 	880.8 (3)	902.8 (3)
	1104.0 (4)	1126.0 (4)
	1327.2 (5)	
	1550.4 (6)	
	1773.6 (7)	
	1996.8 (8)	
E= 	840.6 (3)	
	1063.8 (4)	
F= 	853.6 (3)	
	1076.8 (4)	
G= 	870.6 (3)	
	1093.8 (4)	

**Table 4.** Continued

Structures <sup>a</sup>		[MH] <sup>+</sup> (n) <sup>b</sup>	[M+Na] <sup>+</sup> (n) <sup>b</sup>
H=	$  \begin{array}{c}  \text{CH}_3 \quad \quad \text{CH}_3 \quad \quad \text{CH}_3 \\    \quad \quad   \quad \quad   \\  \text{C}=\text{CH} - \left[ \text{CH}_2 - \text{C} \right]_n - \text{CH}=\text{C} \\    \quad \quad   \quad \quad   \\  \text{C}=\text{O} \quad \quad \text{C}=\text{O} \quad \quad \text{C}=\text{O} \\    \quad \quad   \quad \quad   \\  \text{Hist} \quad \quad \text{Hist} \quad \quad \text{Hist}  \end{array}  $	893.8 (2) 1117.0 (3)	
	$  \begin{array}{c}  \text{CH}_3 \quad \quad \text{CH}_3 \\    \quad \quad   \\  \text{C}_2\text{H}_5\text{O} - \left[ \text{CH}_2 - \text{C} \right]_n - \text{CH}=\text{C} \\    \quad \quad   \\  \text{C}=\text{O} \quad \quad \text{COOH} \\    \quad \quad   \\  \text{Hist} \quad \quad \text{Hist}  \end{array}  $	1023.8 (4) 1247.0 (5)	

a) Hist =



b) Values in parentheses are the repeating units

MHist was in agreement with the feed composition. The potentiometric curves showed large hysteresis loops [4] during the forward and backward titrations with NaOH and HCl solutions, respectively (Figure 3). This may be ascribed to the grinded state of the sample, considering that the MH2 gel particles were large and compact. The large size distribution of the material, along with its compactness, may slow down the equilibration for the protonation mechanism of the gel MH2, due to a hard deep diffusion of the hydrated  $\text{H}^+/\text{OH}^-$  ions into the interior of the gel particles. The potentiometric curves reached a faster equilibrium condition when a finely crushed sample of MH2 was titrated at the equilibration time of 1500 s and 3000 s for each titrant ( $\text{H}^+/\text{OH}^-$ ) addition (Figure 3).

The MALDI-TOF mass spectrometry technique [33–35] has been used to characterize the chemical structures of the polyMHist oligomer components. Figure 5 reports a typical mass spectrum of the polyMHist, recorded in reflection mode, using HABA (0.1N in  $\text{C}_2\text{H}_5\text{OH}$ ) as a matrix and the polymer dissolved in water. This spectrum exhibits a series of peaks from 750 up to 3000 Da corresponding to the protonated and sodiated ions of the polyMHist oligomers with a variety of the end groups, and they have been assigned (Table 4) to a specific oligomer structure. The identification of the structure and the end groups attached to the oligomers produced in the free-radical polymeriza-

tion process is of utmost importance, since the end groups reveal the particular mechanisms that have been active in the polymerization process. The structures of the oligomers corresponding to the mass peak series A, and B in Figure 5, belonging to the expected oligomers terminated with isobutyronitrile (IBN) groups at one end (Table 4), are due to the initial reaction of the radical initiator with the monomer MHist. The oligomers A are also terminated with an etoxyl group ( $-\text{OC}_2\text{H}_5$ ) at the other end chain, indicating that a reaction between macroradicals and the ethanol used as solvent occurred. The oligomers B, besides the IBN groups, are terminated with H and are maybe generated by a H-extraction reaction, that occurs in a typical free-radical polymerization. The last two reactions led to the oligomers C which are terminated with  $-\text{H}$  and  $-\text{OC}_2\text{H}_5$  species (Table 4). The intense peaks belonging to the mass series D were assigned to the unexpected oligomers terminated with methacryloyl chloride groups at both the ends. These are due to the metacryloyl chloride unit present as not detectable trace in the purified MHist used as monomer in the synthesis of the polyMHist sample. These peaks disappeared when the crude polyMHist sample was dissolved in ethanol to prepare the sample for the MALDI analysis, giving in this case intense mass peaks due to the corresponding oligomers with ethyl methacrylate end chains. Looking at the inset in Figure 5, we observe the



presence of weak mass peaks labelled as E, F, G and I (Table 4) corresponding to the oligomers that could be generated from oligomers terminated with metacryloyl chloride groups. Finally, the oligomers species indicated as H and I, as well as the species G, bearing unsaturated end groups (see Table 4) could be formed by the disproportionation reactions that occur during the conventional free radical polymerization.

### 3.2. Protonation study

Potentiometry, viscometry, and solution calorimetry were the main techniques used to study the protonation behaviour of the monomer, the polymer, the copolymers and the hydrogels at 25°C in aqueous 0.15M NaCl.

#### Basicity Constants and viscometry

The basicity constant values for the protonation of the basic imidazole nitrogen ( $\log K_1$ ) and the carboxylate group ( $\log K_2$ ) in the MHist and in the related polymer and copolymers are reported in Table 5. In the same table the basicity constants for the MH2 hydrogel is also reported.

The presence of the methyl groups in the main chain of the polymer structure strongly reduces the polyelectrolyte behaviour because of the increased hydrophobicity. The  $\log K_1$  of the MHist (6.88) showed a greater value than that of the Hist (6.48) for inductive effects. On the other hand, the corresponding polymeric compound showed a quite similar  $\log K$  value. The hydrogel MH2 showed greater  $\log K$ s and a lower  $n$  value; this trend, being similar to the previously studied acrylate hydrogels, may be attributed to the reduced conformational freedom because of the cross-linked network structure.

However, in all cases the  $\log K$ s follow the modified Henderson-Hasselbalch equation [36] showing a linear decreasing pattern on the degree of protonation  $\alpha$  of the whole macromolecule. The experimental data, i.e. pH in relation to  $\alpha$ , fitted very well the generalized Henderson-Hasselbalch equation (1):

$$\text{pH} = \log K_i^\circ + n \cdot \log[(1 - \alpha)/\alpha] \quad (1)$$

which has been checked experimentally for a number of polyelectrolytes [37, 38]. The linear relationship between pH and  $\log[(1 - \alpha)/\alpha]$ , over a wide range of  $\alpha$  values, gives a straight line for all the compounds studied (Figure 6).

This led to exclude any transition region between the coil to compact structure, as occurred for other class of polyelectrolytes [37, 38]. The  $n$  value for the protonation of the imidazole nitrogen in the polyMHist and the corresponding copolymers, being related to the magnitude of the electrostatic interactions as well as being a measure of the hydrophilic influence [39], is always much lower than that reported for the acrylate analogue. Fur-

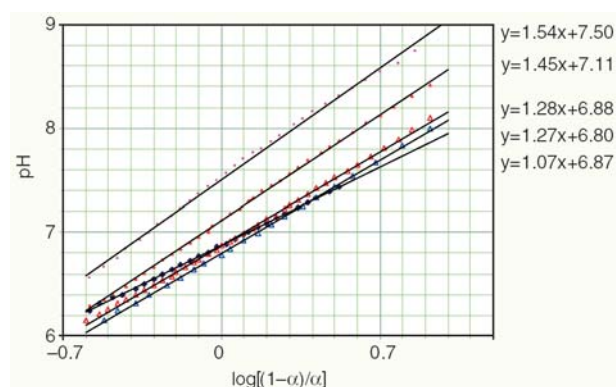


**Figure 6.** Typical Henderson-Hasselbalch plots of the MHist soluble compounds in 0.15M NaCl at 25°C

**Table 5.** Basicity constants of vinyl compounds containing L-histidine residues at 25°C in 0.15M NaCl

Compd	$\log K_1^\circ$	$n_1$	$\log K_2^\circ$
MHist	6.878 (2)		2.772 (6)
Hist <sup>a</sup>	6.48		—
PolyMHist	7.53 (7)	1.49 (5)	2.0
MH2	7.66 (18)	1.29 (9)	2.5
PolyHist <sup>a</sup>	7.64	2.22	2.3
co-3	7.06 (6)	1.41 (6)	2.5
co-2	6.84 (6)	1.23 (7)	2.8
co-1	6.70 (12)	1.15 (12)	2.8
Poly(Hist-co-NIPAAm) <sup>a</sup>	7.11	1.76	2.9
$\log K_1 = \log K_1^\circ + (n_1 - 1) \log[(1 - \alpha)/\alpha]$			

<sup>a</sup>Values in parentheses are standard deviations. Ref. 6.

thermore, as the protonation of the imidazole nitrogen is concerned, the linear decreasing pattern of the  $\log K_1$ , and also of the  $n_1$ , in relation to the MHist content in copolymers with NIPAAm, is a result of the increased distance between the charges along the chain. This reduces the electrostatic contribution of the charges and shows as the monomers are randomly distributed with a predominance of block-like NIPAAm units. Similar results were previously reported for vinyl related copolymers containing *L*-valine residues [30, 31]. In the latter case, the decreasing trend of the  $\log K$  for the acrylates was ascribed to the increased distance between the charges, while methacrylate compounds showed a closer homopolymer polyelectrolyte behaviour. A block-like distribution of the charged methacrylic units was hypothesized in view of their different monomeric structures. In the case of the poly(ampholyte)s, any increase of the uncharged NIPAAm units, leads to a decrease of the proton up-take by the basic imidazole nitrogen. The  $\log K_1$  decrease is always due to the lower decreased electrostaticity exerted by the charged carboxylate anions. When the MHist content is very low, the  $\log K_1$  value approaches that of the corresponding

monomer. On the other hand, the protonation of the carboxylate group in the copolymers cannot be well depicted because of the low basicity constants. These values account only for a limited degree of protonation in the experimental condition of this study.

The viscometric data well support the protonation-like mechanism of the polymers containing MHist. Figure 7 shows the reduced viscosity pattern at different pHs of the homopolymer polyMHist, while Figure 8 shows the conformational behaviour of the corresponding three copolymers.

In all cases, the fully ionized macromolecule ( $L^-$ ) is in the extended chain conformation. As the protonation of the basic imidazole nitrogen occurs, the coiling is sharp at pH close to the  $\log K_1$  and becomes the lowest at the maximum formation of the zwitterionic  $L^\pm$  species. In the polyMHist, as the protonation proceeds, with the neutralization of the carboxylate anion, the coil dimension increases again for the presence of a net positive charge on the macromolecule ( $L^+$ ). This trend, even if present in the copolymers co-3 and co-2, having relatively a greater amount of MHist content, was not shown in the copolymer co-1. Moreover, as the MHist

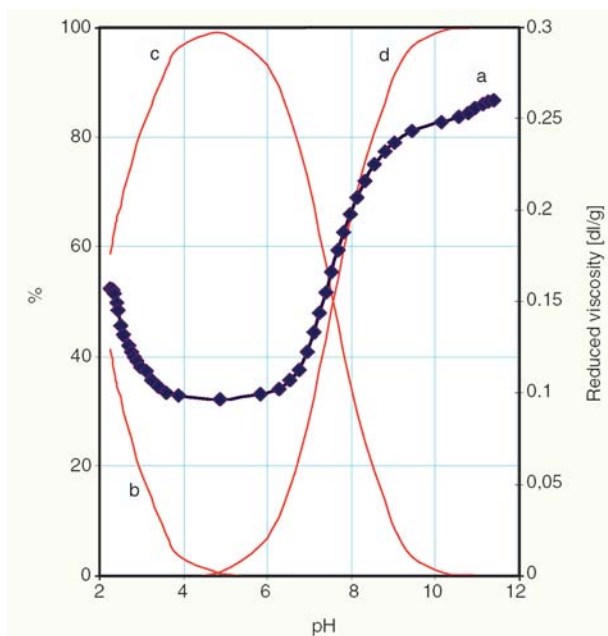


**Figure 7.** Reduced viscosity ( $\eta/C$  [dl/g]) of the polyMHist in relation to the pH (a) with the superimposed species distribution curves [%] obtained by the  $\log K$ s evaluated at 25°C in 0.15M NaCl (b – deprotonated  $L^+$ ; c – mono-protonated, zwitterionic  $L^\pm$ ; d – un-protonated  $L^-$ , where  $L$  is the monomer unit of the polymer)

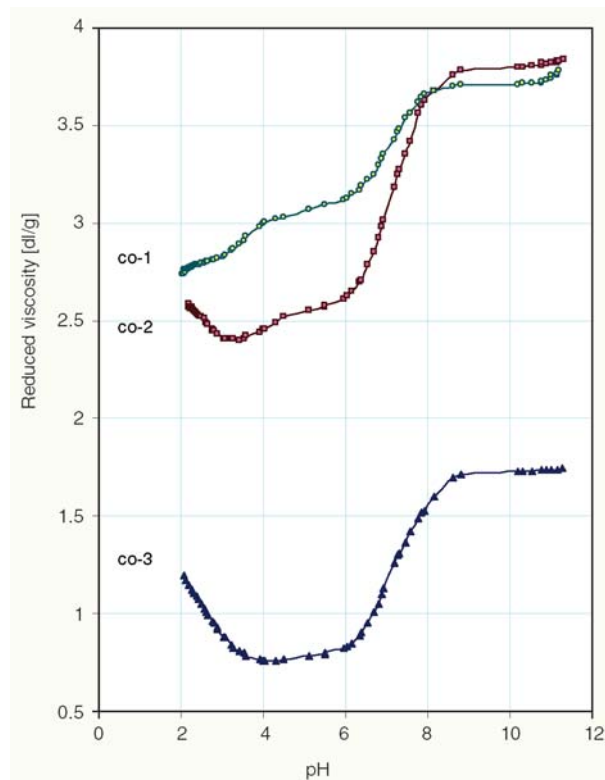


**Figure 8.** Reduced viscosity in relation to the pH for the poly(MHist-co-NIPAAm) copolymers at 25°C in 0.15M NaCl

content in the copolymers decreased, the lowest minimum of the reduced viscosity was shifted at lower pHs, with the disappearance in the *co*-1. Even if this behaviour seems to be quite interesting, the further collapse of the macromolecular coil at lower pH may be due to more competitive electrostatic-hydrophobic forces. During the protonation process, the polymer gradually uncoils, due to the increased electrostaticity of the protonated imidazole nitrogen. The hydrophobic forces between the isopropyl groups in NIPAAm are able to outweigh the repulsive electrostatic interactions when they are present at a critical concentration. A similar behaviour was already observed for vinyl poly (acid)s containing  $\alpha$ -aminoacids with lateral isopropyl groups [30].

#### Enthalpy and entropy changes

The results of the calorimetric titrations revealed, for all the compounds considered, similar enthalpograms during the protonation of the basic groups present in the MHist moiety. The exothermic protonation reaction of the imidazole nitrogen revealed a well defined break-point corresponding to the amount of MHist close to that found by the potentiometry. The further protonation of the carboxylate anion showed a rather negligible endothermicity. Thus, we evaluated the enthalpy ( $-\Delta H^\circ$ ) and the entropy ( $\Delta S^\circ$ ) change values only for the imidazole nitrogen protonation (Table 6). The results of the methacrylate compounds (MHist and polymers containing MHist) showed rather similar protonation behaviour also when compared to the previously reported acrylate analogues [6].

Unlike the reported study on poly(Hist) [6], that showed a peculiar  $-\Delta H^\circ/\alpha$  plot and the protonation process of which was likely attributed to the formation of hydrogen bonds between adjacent monomer

units, the poly(MHist) revealed a ‘real’  $-\Delta H^\circ$  that was independent on the degree of protonation  $\alpha$ . The different behaviour may be ascribed only to the presence of the further methyl group in the backbone macromolecular chain. Its hydrophobic character was evident in the greater  $\Delta S^\circ$  value of the MHist and the polyMHist when compared to the corresponding acrylate analogues [6]. However, the lower polyelectrolyte effect reported for the polyMHist during the protonation of the basic imidazole nitrogen is reflected in a lower  $\Delta S^\circ$  decrease on  $\alpha$ , involving thus the release of further water molecules surrounding closer monomer units. In Figure 9 is reported the decreasing trend of  $\Delta S^\circ$  in relation to  $\alpha$  for the protonation of the imidazole nitrogen in polyMHist and its copolymers with NIPAAm.

The trend is similar to that shown by the corresponding logKs, and, being the  $-\Delta H^\circ$  ‘real’ (i.e. independent on  $\alpha$ ), the polyelectrolyte effect is only attributed to entropy contributions. In fact, the protonation of the imidazole nitrogen led to a sharp decrease of the macromolecular coil with the for-

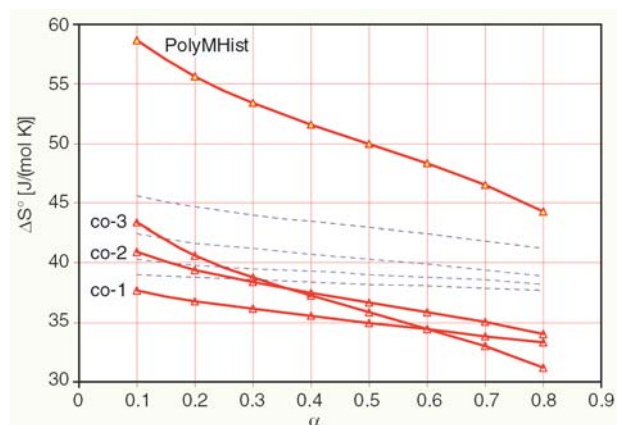


**Figure 9.** Entropy change ( $\Delta S^\circ$  [J/(mol·K)]) values in relation to  $\alpha$  for the protonation of the imidazole nitrogen in polyMHist and related copolymers in 0.15M NaCl and 25°C. (Dotted lines refers to  $-\Delta G^\circ$  of the same compounds)

**Table 6.** Thermodynamic functions of the imidazole nitrogen protonation in vinyl compounds containing L-histidine residues (25°C in 0.15M NaCl)

Compd	$-\Delta G^\circ$ , [kJ/mol]	$-\Delta H^\circ$ , [kJ/mol]	$\Delta S^\circ$ , [J/(mol·K)]	Ref.
MHist	39.26 (1)	29.3 (2)	33.4 (7)	This work
Hist	37.0	30.5	21.8	[6]
PolyMHist	43.0 (4)	28.1 (4)	50 (1)	This work
PolyHist	43.6	30.6	44	[6]
co-3	40.3 (3)	29.6 (6)	36 (2)	This work
co-2	39.0 (3)	28.1 (6)	37 (2)	This work
co-1	38.2 (7)	28.7 (7)	35 (2)	This work
Poly(Hist-co-NIPAAm)	40.6	29.5	37	[6]

mation of zwitterionic species. Besides the likely ordering to some extent of the zwitterions, the process led to a release of water molecules because the macromolecule becomes tightly coiled. This was seen in some cases because phase separation occurred at the isoelectric point. As a matter of fact, the corresponding hydrogels decreased their degree of swelling for the loss of water molecules.

### 3.3. Swelling behaviour of hydrogels

The swelling behaviour of the hydrogels was studied in relation to the pH, the temperature, the electric current, and the concentration of the simple NaCl salt at pH 9, i.e. in the completely ionized form of the MHist units. The sample slabs swelling kinetics for the two different cross-linked CMH2 and CMH10 hydrogels was recorded at constant ionic strength (0.15M NaCl) and at two different pHs (1.9 and 8.8). The results, reported in Figure 10, show the different hydration ability in the different pH conditions. It is evident that the degree of swelling (DS) is greater for the less cross-linked CMH2 gel and at higher pHs. In both cases, the equilibrium DS was reached within few hours. Both the gels are friable in the dry state and become transparent as the water content increases.

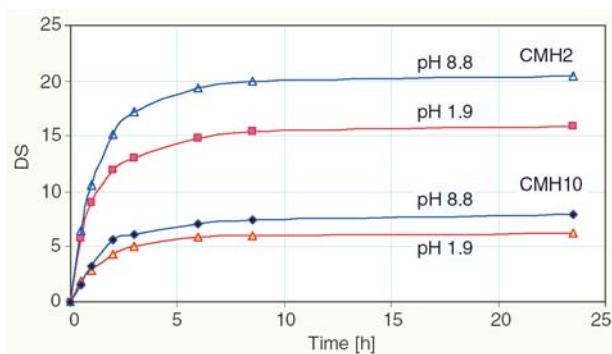


**Figure 10.** Swelling kinetics of the hydrogels CMH2 (slabs of 50 mg) and CMH10 (slabs of 55 mg) at two different pHs in 0.15M NaCl and 24°C

#### *Effect of pH, temperature, ionic strength, and electric current*

The swelling behaviour of the hydrogel MH2 in relation to pH, at 25°C in 0.15M NaCl, is reported in Figure 11. The EDS/pH plot, being similar to that reported for the viscometric data of polyMHist in Figure 7, sensitively reveals a decreasing pattern by increasing the pH in the narrow range 4 to 6. In

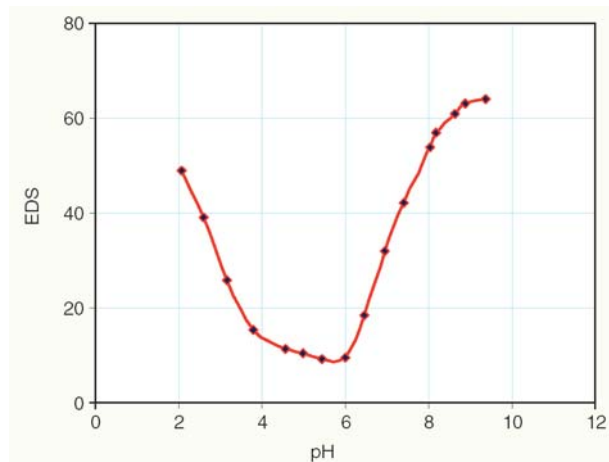


**Figure 11.** Equilibrium degree of swelling (EDS) in relation to the pH of the gel MH2 in 0.15M NaCl at 25°C

this pH-range the zwitterionic form predominates with its maximum at the isoelectric point (i.p., pH 5). It is likely that the greater logK values of the hydrogel, with its lower polyelectrolyte behaviour, may lead to more stable ionized species of greater hydrophilic quality. As the pH shifts-out from this range, the gel MH2 swells as a consequence of its water content increase, due to the predominance of net positive or negative charges.

On the other hand, the hydrogel CMH2 behaves likewise the copolymer co-2, having the latter a similar comonomer composition. In Figure 12 the EDS/pH profile of the hydrogel CMH2 at 25°C in 0.15M NaCl is reported. Compared to the previously reported acrylate CH1 hydrogel containing Hist [19], the lower EDS value is due to the greater cross-link density in CMH2. The striking similarity of the swelling behaviour with the reduced viscos-

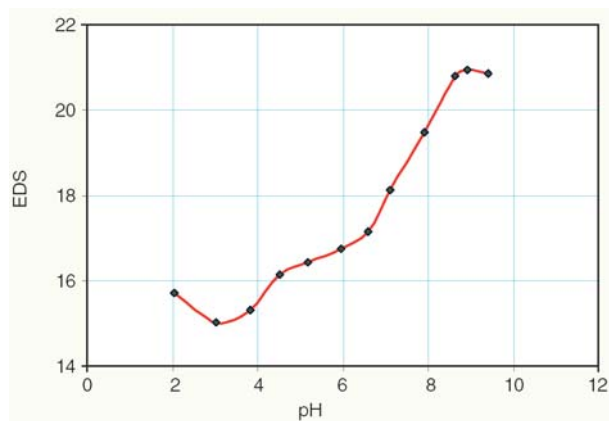


**Figure 12.** Equilibrium degree of swelling (EDS) in relation to the pH of the gel CMH2 in 0.15M NaCl at 25°C



ity (Figure 8) suggests a similar polyelectrolyte behaviour of the two polymers, even in the different free and cross-linked forms. On the basis of these results it is likely to hypothesize any tailoring hydrogel system to collapse at desired pHs, by introducing the right amount of the two comonomers. Of course, if in these copolymers the MHist content becomes less than a critical value (about 5 mol%), the polyampholyte quality vanishes because of the superimposing effect of the hydrophobic interactions exerted by the isopropyl groups of the NIPAAm moieties.

As regards the effect of the temperature, Figure 13 shows the swelling behaviour of the CMH2 hydrogel in a wide range of temperatures. The hydrogel swelling was studied in 0.15M NaCl and in three different buffered solutions of significant pHs.

Any increase of the temperature resulted in a deswelling ability of the hydrogel. It retained its hydration state at high as well as at low pHs. Contrary to the previously reported acrylate hydrogel CH1 [19], the CMH2 hydrogel showed a phase separation at higher temperatures and at lower pHs. The presence of the hydrophobic MHist unit, instead of decreasing the LCST (Lower Critical Solution Temperature) [40] of the NIPAAm based hydrogels (32°C), revealed a greater temperature increase. This point will be better investigated even though the behaviour may be further on ascribed to the peculiar protonation mechanism of the MHist based hydrogels. A similar greater increase of the phase separation temperature was observed for the

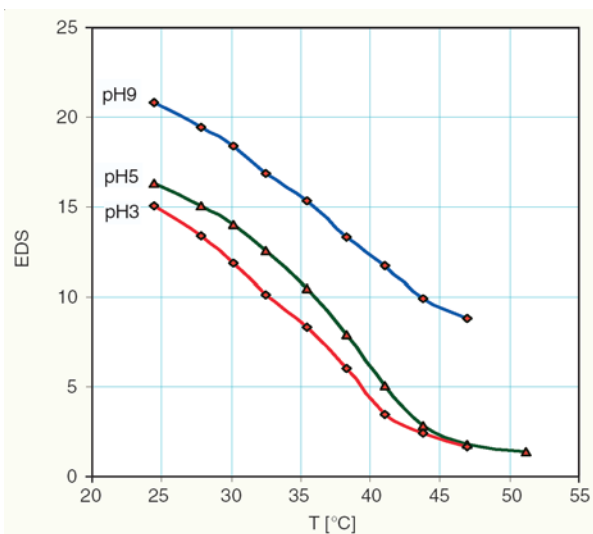


**Figure 13.** EDS of the gel CMH2 in relation to the temperature [°C] at three different pHs in 0.15M NaCl

soluble copolymers. In Figure 14 is reported the relationship between the viscometric data and the temperature (in the range 25–46°C) of the three copolymers (co-1, co-2, and co-3) at the three significant pHs (9, most negatively ionized; 5, zwitterionic; 2, most positively ionized).

Unlike the straight line observed in all cases by co-3, the copolymer co-2 showed an increased negative line slope at pH 5, close to 38°C; on the other hand, the co-1 showed more negative line slopes at different temperatures, depending on the pH. Table 7 summarizes the obtained results. The observed differences are due to the different content of the MHist units in the copolymers; lower MHist content displayed greater responsiveness to pH and temperature. It is worthwhile noting the

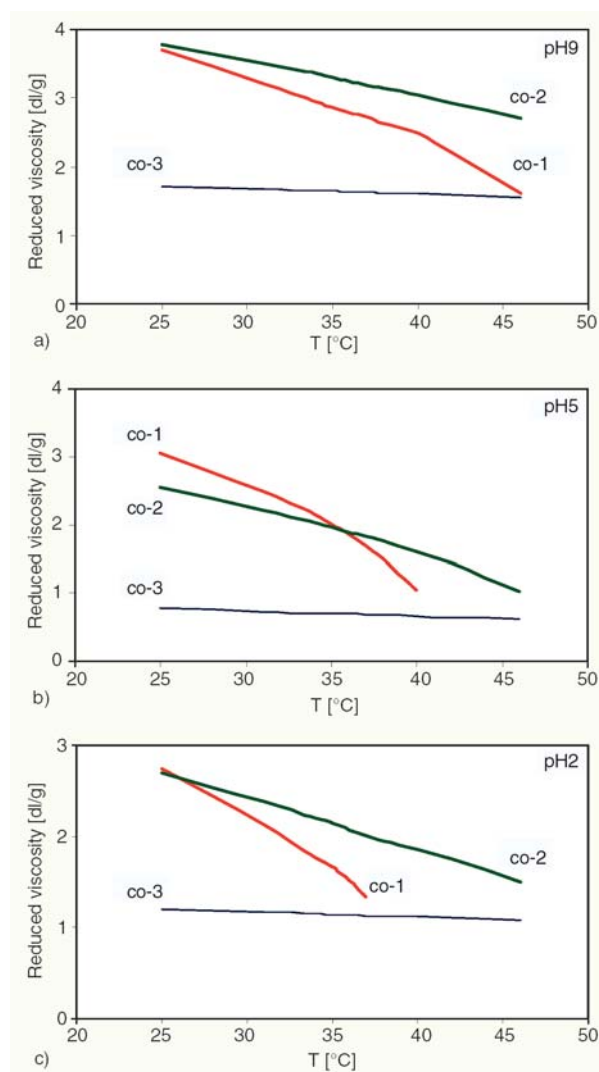


**Figure 14.** Reduced viscosity ( $\eta/C$  [dl/g]) of the three copolymers (co-1, red curves; co-2, green curves; co-3, blue curves) in relation to the temperature at three different pHs (9, 5 and 2) in 0.15M NaCl

**Table 7.** Straight line parameters from the reduced viscosity values of the three copolymers co-1, co-2, and co-3

Copolymer	pH	Line slope	R <sup>2</sup>	Range of temperatures [°C]
co-3	2	−0.0054	0.990	25–46
	5	−0.0074	0.989	25–46
	9	−0.0079	0.995	25–46
co-2	2	−0.057	0.999	25–46
	5	−0.072	0.982	25–46
	5	−0.061	0.998	25–38
	5	−0.094	0.995	38–46
	9	−0.052	0.999	25–46
co-1	2	−0.115	0.994	25–46
	2	−0.109	0.998	25–35
	2	−0.166	0.993	35–37
	5	−0.126	0.964	25–46
	5	−0.105	0.996	25–35.5
	5	−0.205	0.997	35.5–46
	9	−0.096	0.981	25–46
	9	−0.083	0.999	25–40
	9	−0.146	0.999	40–46

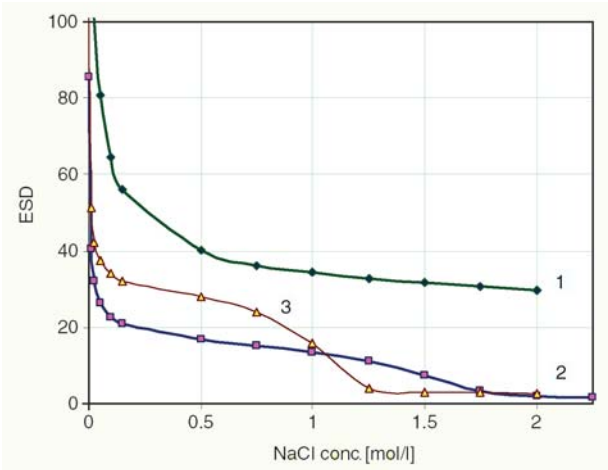


**Figure 15.** EDS of gels MH2 (1), CMH2 (2), and CH1 (3) [19] in relation to the concentration of NaCl (pH 9 and 25°C)

similar behaviour between the viscosity of the soluble co-1 and the EDS of the cross-linked gel CMH2 (Figure 13), having both the compounds similar MHist content. At the three different pHs, either the reduced viscosity and the EDS values follow the same trend and collapse almost at the same temperatures.

Moreover, the effect of the ionic strength, i.e. the concentration of sodium chloride, on the swelling properties of the MH2 and CMH2 hydrogels at pH 9, is reported in Figure 15 along with the results previously obtained with the gel CH1 [19], for comparison.

Unlike the hydrogel MH2, which shows only poly-electrolyte behaviour for the shielding effect of the

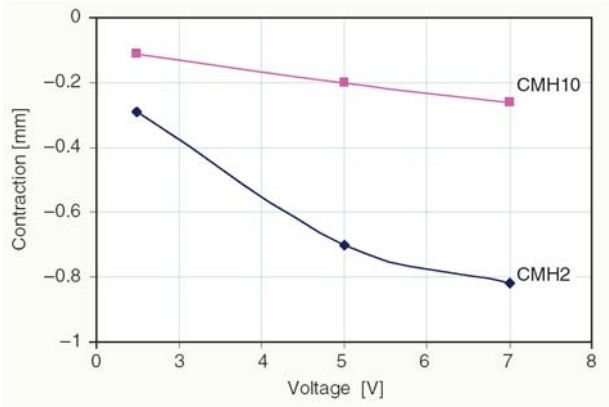


**Figure 16.** Hydrogel contraction [mm] in relation to the electric stimulation (2.5, 5.0, and 7.0 V) at 10 minutes elapsed time and pH 9

carboxylate groups negative charges, the CMH2 showed a volume phase transition phenomenon at a NaCl concentration of 1.75 mol/l. This concentration resulted greater than that shown by the Hist-based CH1 hydrogel [19].

The electric current effect on the two hydrogels is reported in Figure 16. Any increase of the applied potential linearly increased the gel contraction. Moreover, the contraction of the gel CMH2 was higher than that of CMH10, because of the lower cross-links amount. These results, although more effective, are in agreement with the previously reported ones on the gels containing the acrylate Hist analogues.

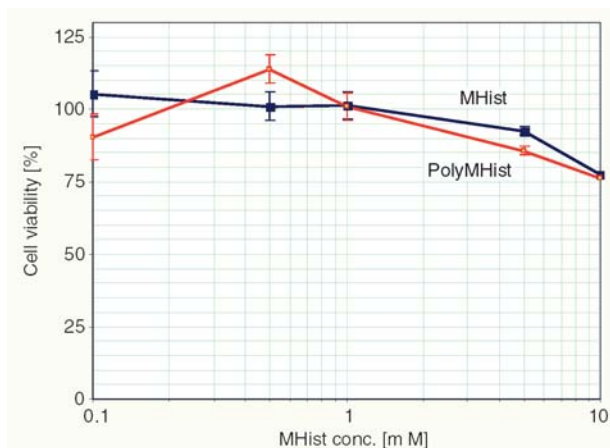


**Figure 17.** Cytotoxicity of the MHist and poly(MHist) against MC3T3-E1 (mouse osteoblast) cells

### 3.4. In vitro cytotoxicity

The cytotoxic effect of the poly(MHist) was evaluated by the cell culture of osteoblasts from mouse (MC3T3-E1). Figure 17 shows the cell proliferation in the presence of the polymer and its low-molecular weight precursor.

It is noticeable that no significant cytotoxicity was observed for two days at concentration up to 5 mM. Thus, these zwitterionic compounds in the cross-linked hydrogel form may show potential applications in bone resorption when implanted in specific tissues, for the releasing of loaded amino-bisphosphonate drugs [17].

## 4. Conclusions

This paper, concerning with our research interest on poly(ampholyte)s [6, 19, 41], developed a thermodynamic study for the protonation of basic groups in the free and cross-linked methacrylate polymers carrying the L-histidine residues. As a rule, methacrylate polyelectrolytes, particularly poly(carboxyl acid)s, show more complex thermodynamic data than the corresponding acrylates [42]. In the case of poly(ampholyte)s, the more hydrophobic character of the main polymer chain was evident in both the free and the cross-linked hydrogels. Unlike the corresponding acrylate, these new ligands show a lower polyelectrolyte behaviour. The ‘real’ enthalpy changes and the lower  $n$  values of the modified Henderson-Hasselbalch equation are the two main thermodynamic data showing the difference. Moreover, the volume phase transition behaviour of the hydrogels, based on the pH-

responsive poly(ampholyte)s and on the temperature-responsive *N*-isopropylacrylamide, revealed that the thermodynamic data are close to the soluble analogues ones. The LCST of the polyNI-PAAm, that is close to the body temperature, may be tuned by the pH and the proper amount of the purposely synthesized ampholyte monomer. Thermodynamic and biological characterization, along with the salt-induced phase transition and the dc electroshrinking phenomenon shown by the methacrylate hydrogels, are indicative of a suitability of these materials for tissue engineering applications [15]. The increasing hydrophobic character makes some poly(ampholyte)s suitable for the preparation of nonbiofouling surfaces against proteins and cells [22].

## Acknowledgements

The research work was supported by a grant of the Italian MIUR, as a project within PRIN 2004, and by a grant of the PAR 2005 (Siena University). Thanks are due to Miss Ilaria Casolaro for having carefully read the manuscript.

## References

- [1] Casolaro M.: Stimuli-responsive polymers (thermodynamics in drug delivery technology). in ‘Polymeric Materials Encyclopedia’ (Ed.: Salamone J. C.), CRC Press, Boca Raton, vol. **10**, 7979–7992 (1996).
- [2] Casolaro M., Paccagnini E., Mendichi R., Ito Y.: Stimuli-responsive polymers based on L-phenylalanine residues: the protonation thermodynamics of free polymers and cross-linked hydrogels. *Macromolecules*, **38**, 2460–2468 (2005).
- [3] Barbucci R., Casolaro M., Magnani A.: Ionic and ionizable synthetic polymers: interactions in aqueous solution. *Coordination Chemistry Reviews*, **120**, 29–50 (1992).
- [4] Casolaro M.: Thermodynamics of multiple-responsive polyelectrolytes with complexing ability towards the copper(II) ion. *Reactive Polymers*, **23**, 71–83 (1994).
- [5] Bignotti F., Penco M., Sartore L., Peroni I., Mendichi R., Casolaro M., D’Amore A.: Synthesis, characterization and solution behaviour of intelligent polymers bearing L-leucine residues in the side chains. *Polymer*, **41**, 8247–8256 (2000).
- [6] Casolaro M., Bottari S., Cappelli A., Mendichi R., Ito Y.: Vinyl polymers based on L-histidine residues. Part 1.: The thermodynamics of poly(ampholyte)s in the free and in the cross-linked gel form. *Biomacromolecules*, **5**, 1325–1332 (2004).
- [7] Cho I., Shin J-S.: Hydrophobic and ionic interactions in the ester hydrolysis by imidazole-containing polymers. *Bulletin of Korean Chemical Society*, **3**, 34–36 (1982).

- [8] Bertini I., Scozzafava A.: Copper(II) as probe in substituted metalloproteins. in 'Metal ions in biological systems' (Ed.: Sigel H.) Marcel Dekker, New York, **12**, 31–74 (1981).
- [9] Kowalik-Jankowska T., Ruta-Dolejsz M., Wisniewska K., Lankiewicz L., Kozłowski H.: Copper(II) complexation by human and mouse fragments (11–16) of  $\beta$ -amiloid peptide. *Journal of the Chemical Society, Dalton Transactions*, 4511–4519 (2000).
- [10] Aronoff-Spencer E., Burns C. S., Avdievich N. I., Gerfen G. J., Peisach J., Antholine W. E., Ball H. L., Cohen F. E., Prusiner S., Millhauser G. L.: Identification of the  $\text{Cu}^{2+}$  binding sites in the N-terminal domain of the prion protein by EPR and CD spectroscopy. *Biochemistry*, **39**, 13760–13771 (2000).
- [11] Kumar A., Kamihira M., Galaev I. Y., Iijima S., Mattiasson B.: Binding of Cu(II)-poly(*N*-isopropylacrylamide)/vinylimidazole copolymer to histidine-tagged protein: a surface plasmon resonance study. *Langmuir*, **16**, 865–871 (2003).
- [12] Kumar A., Wahlund P.-O., Kepka C., Galaev I. Y., Mattiasson B.: Purification of histidine-tagged single-chain Fv-antibody fragments by metal chelate affinity precipitation using thermoresponsive copolymers. *Biotechnology and Bioengineering*, **84**, 494–503 (2003).
- [13] Carter S., Rimmer S., Sturdy A., Webb M.: Highly branched stimuli responsive poly[(*N*-isopropylacrylamide)-co-(1,2-propandiol-3-methacrylate)]s with protein binding functionality. *Macromolecular Bioscience*, **5**, 373–378 (2005).
- [14] Carter S., Rimmer S., Rutkaite R., Swanson L., Fairclough J. P. A., Sturdy A., Webb M.: Highly branched poly(*N*-isopropylacrylamide) for use in protein purification. *Biomacromolecules*, **7**, 1124–1130 (2006).
- [15] Stile R. A., Burghardt W. R., Healy K. E.: Synthesis and characterization of injectable poly(*N*-isopropylacrylamide)-based hydrogels that support tissue formation in vitro. *Macromolecules*, **32**, 7370–7379 (1999).
- [16] Cini R., Defazio S., Tamasi G., Casolaro M., Messori L., Casini A., Morpurgo M., Hursthouse M.: *fac*-( $\text{Ru}(\text{CO})_3$ )<sup>2+</sup>-core complexes and design of metal-based drugs. Synthesis, structure, and reactivity of Ru-thiazole derivative with serum proteins and absorption-release studies with acryloyl and silica hydrogels as carriers in physiological media. *Inorganic Chemistry*, **46**, 79–92 (2007).
- [17] Casolaro M., Casolaro I., Spreafico A., Capperucci C., Frediani B., Marcolongo R., Margiotta N., Ostuni R., Mendichi R., Samperi F., Ishii T., Ito Y.: Novel therapeutic agents for bone resorption. Part 1. Synthesis and protonation thermodynamics of poly(amidoamine)s containing bis-phosphonate residues. *Biomacromolecules*, **7**, 3417–3427 (2006).
- [18] Lin J. H.: Bisphosphonates: A review of their pharmacokinetic properties. *Bone*, **18**, 75–85 (1996).
- [19] Casolaro M., Bottari S., Ito Y.: Vinyl polymers based on L-histidine residues. Part 2. The swelling and electric behaviour of smart poly(ampholyte) hydrogels for biomedical applications. *Biomacromolecules*, **7**, 1439–1448 (2006).
- [20] Nitschke M., Götz T., Gramm S., Werner C.: Detachment of human endothelial cell sheets from thermoresponsive poly(NiPAAm-co-DEGMA) carriers. *Express Polymer Letters*, **1**, 660–666 (2007).
- [21] Morcellet-Sauvage J., Morcellet M., Loucheux C.: Polymethacrylic acid derivatives. 1. Preparation, characterization, and potentiometric study of poly(*N*-metacryloyl-L-alanine-co-N-phenylmethacrylamide). *Die Makromolekulare Chemie*, **182**, 949–963 (1981).
- [22] Ishii T., Wada A., Tsuzuki S., Casolaro M., Ito Y.: Copolymers including L-histidine and hydrophobic moiety for preparation of nonbiofouling surface. *Biomacromolecules*, **8**, 3340–3344 (2007).
- [23] Okamoto Y.: Hydrolyses of  $\alpha$ -amino acid p-nitrophenyl esters by poly(*N*-methacryloyl-L-histidine) (in Japanese). *Journal of The Chemical Society of Japan*, **6**, 870–873 (1978).
- [24] Iwakura Y., Toda F., Suzuki H.: Synthesis of *N*-[1-(1-substituted 2-oxopropyl)]acrylamides and -methacrylamides. Isolation and some reactions of intermediates of the Daikin-West reaction. *Journal of Organic Chemistry*, **32**, 440–443 (1967).
- [25] Rempp P., Merrill E. W.: Polymer synthesis. Huthig and Wepf, Basel (1991).
- [26] Penco M., Bignotti F., Sartore L., Peroni I., Casolaro M., D'Amore A.: Stimuli-responsive polymers based on *N*-isopropylacrylamide and *N*-methacryloyl-L-leucine. *Macromolecular Chemistry and Physics*, **202**, 1150–1155 (2001).
- [27] Barbucci R., Casolaro M., Danzo N., Barone V., Ferruti P., Angeloni A.: Effect of different shielding groups on polyelectrolyte behaviour of polyamines. *Macromolecules*, **16**, 456–462 (1983).
- [28] Gans P., Sabatini A., Vacca A.: Superquad: an improved general program for computation of formation constants from potentiometric data. *Journal of the Chemical Society, Dalton Transactions*, 1195–1200 (1985).
- [29] Ishiyama M., Tominaga H., Shiga M., Sasamoto K., Ohkura Y., Ueno K.: A combined assay of cell viability and in vitro cytotoxicity with a highly water-soluble tetrazolium salt, neutral red and crystal violet. *Biological and Pharmaceutical Bulletin*, **19**, 1518–1520 (1996).
- [30] Casolaro M.: Vinyl polymers containing L-valine and L-leucine residues: thermodynamic behaviour of homopolymers and copolymers with *N*-isopropylacrylamide. *Macromolecules*, **28**, 2351–2358 (1995).
- [31] Casolaro M., Barbucci R.: Thermodynamic behaviour of polyelectrolytes with the lower critical solution temperature (LCST) phenomena. *Polymers for Advanced Technologies*, **7**, 831–838 (1996).



- [32] Casolaro M.: Intelligent polymer systems for molecular separation and controlled delivery of drugs. In 'Frontiers in biomedical polymer applications' (Ed.: Ottenbrite R. M.) Technomic Publishing Co. Inc., Lancaster, Vol. 1, 109–122 (1998).
- [33] Montaudo G., Montaudo M. S.: Polymer characterization methods. in 'Mass Spectrometry of Polymers' (Eds.: Montaudo G., Lattimer R. P.) CRC Press, Boca Raton, 41–111 (2002).
- [34] Montaudo G., Montaudo M. S., Samperi F.: Matrix-assisted laser desorption ionization/mass spectrometry of polymers (MALDI-MS). in 'Mass Spectrometry of Polymers' (Eds.: Montaudo G., Lattimer R. P.) CRC Press, Boca Raton, 419–521 (2002).
- [35] Montaudo G., Samperi F., Montaudo M. S.: Characterization of synthetic polymers by MALDI-MS. *Progress in Polymer Science*, **31**, 277–357 (2006).
- [36] Morawetz H.: *Macromolecules in Solution*, Wiley-Interscience, New York (1980).
- [37] Katchalsky A., Spitnik P.: Potentiometric titrations of polymethacrylic acid. *Journal of Polymer Science*, **2**, 432–446 (1947).
- [38] Murai N., Sugai S.: Side-chain effect on conformation of ionizable polypeptides in aqueous solution. *Biopolymers*, **13**, 1161–1171 (1974).
- [39] Barbucci R., Casolaro M., Magnani A., Roncolini C.: Different protonation behaviour of two poly(methacrylic acid) derivatives containing *N*-acylglycine and *N*-acyl- $\beta$ -alanine residues: Thermodynamic and FT-IR studies. *Macromolecules*, **24**, 1249–1257 (1991).
- [40] Schild H. G., Tirrel D. A.: Microcalorimetric detection of lower critical solution temperatures in aqueous polymer solutions. *The Journal of Physical Chemistry*, **94**, 4352–4356 (1990).
- [41] Kudaibergenov S. E.: *Polyampholytes: synthesis, characterization and application*. Kluwer Academic, New York (2002).
- [42] Bekturov E. A., Bakauova Z. Kh.: *Synthetic water-soluble polymers in solution*. Huethig and Wepf Verlag, Basel (1986).

# Poly(CL/DLLA-b-CL) multiblock copolymers as biodegradable thermoplastic elastomers

T. Ryyänen<sup>1</sup>, A. Nykänen<sup>2</sup>, J. V. Seppälä<sup>1\*</sup>

<sup>1</sup>Helsinki University of Technology, Department of Chemical Technology, Laboratory of Polymer Technology, P.O. Box 6100, FI-02015 TKK, Finland

<sup>2</sup>Helsinki University of Technology, Department of Engineering Physics and Mathematics, Laboratory of Optics and Molecular Materials, P. O. Box 2200, FI-02015 TKK, Finland

Received 23 October 2007; accepted in revised form 19 January 2008

**Abstract.** Lactic acid and  $\epsilon$ -caprolactone based polymers and their derivatives are widely used in biomedical applications. Different properties are introduced by modifying the composition. In this study, poly( $\epsilon$ -caprolactone/D,L-lactide)-b-poly( $\epsilon$ -caprolactone) multiblock copolymers were synthesized as poly(ester-urethane)s (PEUs) by polymerizing in two steps involving ring-opening polymerization of precursors and by diisocyanate linking of precursors to produce thermoplastic elastomers (TPEs). The precursors and products were characterized by SEC, <sup>1</sup>H-NMR and DSC, and dynamic mechanical study (by dynamic mechanical analysis, DMA) as well as morphological characterization (by transmission electron microscopy, TEM) of the product TPEs was carried out. Tensile and creep recovery properties of them were also studied. According to the characterizations, all the polymerizations were successful, and the prepared TPEs showed clear elastic behavior. In the DMA scans, rubbery plateau in the storage modulus curves between  $T_g$  and terminal flow region was clearly detectable indicating elasticity. The TEM images demonstrated phase separation of amorphous and crystalline blocks when the degree of crystallinity of the hard blocks was high enough. The elongations of TPEs varied between 800–1800%, while the modulus was 7–66 MPa. Two different types of recovery tests indicated the creep properties of TPEs to be highly dependent on the degree of crystallinity.

**Keywords:** biodegradable polymers, lactide,  $\epsilon$ -caprolactone, poly(ester-urethane)s (PEUs), thermoplastic elastomers (TPEs)

## 1. Introduction

Widening the range of mechanical properties of biodegradable polymers has been increasingly studied for last decades. Ever-growing applications scope of biomaterials runs efforts to design polymers with new more sophisticated characteristics. One of often favorable characteristic for biomedical materials is elasticity. Elasticity is traditionally achieved by cross-linking techniques and the rubbery properties are resulting from the chemical network structure of thermosets [1]. However, in many biomedical applications, thermoplasticity of

an elastomer is a highly favourable property enabling processing, remoulding and even injection of the elastomer *in situ*. This kind of thermoplastic elastomers (TPEs) can be prepared by introducing phase-separating blocks in the polymer chain so building up physically cross-linked reversible network [2].

TPEs typically are block copolymers consisting of amorphous soft segments and crystalline hard segments. There are only a few different polymerization methods that have been used to prepare biodegradable block copolymer structured elas-

\*Corresponding author, e-mail: [jukka.seppala@tkk.fi](mailto:jukka.seppala@tkk.fi)  
© BME-PT and GTE

tomers. One of those methods is chain extension where different types of precursors are linked to produce high molecular weight block copolymers with linking agents. Chain extension method in block copolymerization has formerly been utilized in the biopolymer group of our laboratory [3–8], and in some other groups [9–11]. The most widely used linking agents have been diisocyanates which combine hydroxyl terminated precursors to poly(ester-urethane)s. In addition to that, several research groups have prepared block copolymer structures by living ring-opening polymerization, or by something close to that, using pre-prepared macroinitiators (segment A) to initiate the ring-opening polymerization of segment B [12–16]. Newer polymerization techniques, such as atom transfer radical polymerization (ATRP), have been utilized to make the control of the resulting block copolymer architecture more precise [17].

Along with development of different polymerization methods, the variety of monomers and different compositions of block copolymers have been key factors in the design of TPEs. The use of conventional biopolymer monomers such as different lactones has been widely reported in literature [9–17]. Typically semi-crystalline poly(L-lactide) and poly(D-lactide) have been used as the hard blocks [9–18] while amorphous poly( $\epsilon$ -caprolactone) [10–12, 18], poly(1,3-trimethylene carbonate) [13–15] and poly(ethylene oxide) [19] have been often used as soft components in block structured biodegradable TPEs.

This study is natural continuum of the earlier work in the field of poly(ester-urethane)s carried by our biopolymer group in Helsinki University of Technology [1, 3–7]. In this study, poly( $\epsilon$ -caprolactone/D,L-lactide)-*b*-poly( $\epsilon$ -caprolactone) multiblock copolymers were synthesized to produce biodegradable thermoplastic elastomers. The objective was to enhance the recovery and creep properties of amorphous poly( $\epsilon$ -caprolactone/D,L-lactide) copolymers by linking semicrystalline poly( $\epsilon$ -caprolactone) blocks between linear polymer chains. In other words, the purpose was to achieve physical cross-linking by secondary hydrogen bonds between polymer chains by adding crystalline segments to an amorphous copolymer. Poly( $\epsilon$ -caprolactone) was chosen to act as hard block as it is known capable to crystallize

[7, 20]. The CL/DLLA semi-random copolymers in molar compositions of 30/70, 50/50 and 70/30 were chosen to act as soft blocks because they were known to be fully amorphous by the study of Hiljanen-Vainio *et al.* [20]. The aim was to evaluate the effect of different quantities of crystalline phase to the recovery properties of the TPEs. Thus mechanical and recovery properties of these TPEs were rather extensively studied in addition to thermal and dynamic mechanical tests.

## 2. Experimental

### 2.1. Materials

The poly( $\epsilon$ -caprolactone/D,L-lactide) and poly( $\epsilon$ -caprolactone) precursors were polymerised from D,L-lactide (DLLA; Purac) and  $\epsilon$ -caprolactone (CL; Solvay). DLLA was recrystallized from toluene and CL was dried over molecular sieves. Stannous octoate (SnOct<sub>2</sub>; Sigma) and 1,4-butanediol (BD; Fluka Chemica) were used as received in the ring-opening polymerization of precursors. In the linking reaction, 1,6-hexamethylenediisocyanate (HMDI) was used, without further treatment, as chain extender.

### 2.2. Preparation of poly( $\epsilon$ -caprolactone/D,L-lactide) and poly( $\epsilon$ -caprolactone) precursors

The poly( $\epsilon$ -caprolactone/D,L-lactide) and poly( $\epsilon$ -caprolactone) precursors, respectively amorphous and semicrystalline segments of the elastic poly(ester-urethane) multiblock copolymers, are denoted by P(CL/DLLA-BD) and P(CL-BD), and e.g., by P(30/70-1) and P(100-1). The precursors were polymerized in melt from CL and DLLA at 160°C under nitrogen atmosphere for six hours in a batch reactor designed for agitation of viscous materials. The monomers were fed to the reactor with an appropriate amount of 1,4-butanediol as co-initiator (0,5, 1,0 or 5,0 per 100 monomer units) for hydroxyl termination and control of molecular weight of the precursor. Stannous octoate was used as initiator with amount of 0,02 mol%. The reaction procedure is thoroughly discussed in the previous publication of our group by Helminen *et al.* [1].

### 2.3. Chain extension of precursors into elastic poly(ester-urethanes)

PEUs were polymerized in a 200 ml round-bottomed flask reactor equipped with one-armed stirrer. Precursors were first added to the reactor in the molar ratio of 1:1 and melted at 160°C in argon atmosphere before 30 mol% excess of 1,6-hexamethylene diisocyanate as chain extender was fed to the reactor. In earlier work by our group [3] on the chain extending reactions of isocyanates with hydroxyl groups, the high temperature was introduced as a means to avoid the use of solvents and catalysts typically used in the functionalization of hydroxyl groups with isocyanates. If high temperatures are allowed a more straightforward route to the desired products is achieved without the use of these additional components. The amount of HMDI was calculated from the theoretical molecular weight of the synthesized precursors, and the 30 mol% excess used in linking reactions results from earlier experience in diisocyanate chemistry in our group [3, 4]. The reaction time was 7–12 minutes determined of the growth rate of the viscosity of the reaction mixture.

### 2.4. Characterisations

Molecular weights ( $M_n$  and  $M_w$ ) and molecular weight distributions (MWD) were determined relative to polystyrene standards by size exclusion chromatography (SEC). The Waters Associates system was equipped with a Waters 717plus autosampler injector, a Waters 510 HPLC solvent pump, four linear PL gel columns ( $10^4$ ,  $10^5$ ,  $10^3$ , and  $100 \text{ \AA}$ ) connected in series, and a Waters 2414 refractive index detector. All samples were analyzed at room temperature. Chloroform (Riedel-de Haën; stabilized with 1% ethanol) was used as eluent, and was delivered at a flow rate of 1.0 ml/min. The samples were dissolved in chloroform at a concentration of 1.0% (w/v). The injection volume was 200  $\mu\text{l}$ .

For  $^1\text{H}$ -NMR measurements, the samples were dissolved in chloroform- $d_1$  (Aldrich; deuteration degree not less than 99.8%) in 5 mm NMR tubes at room temperature. The sample concentration was about 1.0% by weight. NMR spectra were recorded on a Varian Gemini 2000 300 MHz NMR spectrometer working at 300 032 MHz for proton.

Differential scanning calorimetric (DSC) measurements were carried out on a Mettler Toledo Star<sup>e</sup> DSC 821<sup>e</sup>. The measurements were run from –100 to 180°C at heating and cooling rates of 10°C·min<sup>–1</sup>. The glass transition temperatures ( $T_g$ ), melting temperatures ( $T_m$ ), and melting endotherms ( $\Delta H$ ) of the precursors and linked elastomers were measured during the second heating period.

Dynamic mechanical analysis (DMA) was performed on a Perkin-Elmer 7 Series instrument. The specimens were die-cut from 2.0 mm thick hot-pressed polymer plate. The measurements were carried out using the three-point bending geometry (sample size 2.0×5.0×18.0 mm) over a temperature range of –70 to 60°C at a rate of 4°C·min<sup>–1</sup>. All measurements were carried out at 1 Hz.

Transmission electron microscopy (TEM) was used in morphological studies of the TPEs. Contrast for the morphological characterization was achieved by a sample preparation technique that relies on different rates of diffusion of a RuO<sub>4</sub> stain into the amorphous and semi-crystalline regions [21]. First, the sample surface was cut at temperature of –100°C to make a smooth surface for the stain to penetrate into the sample. The samples were then stained in vapor of 0.5% RuO<sub>4</sub> stabilized aqueous solution (Electron Microscopy Science) for a period of three days. The stained sample was microtomed using a Leica Ultracut UCT ultra-microtome with a diamond knife at temperature of –100°C, and 70 nm thick sections were collected on 300-mesh sized lacey carbon coated copper grids. Bright field TEM was performed with Tecnai 12 transmission electron microscope using 120 kV accelerating voltage.

Tensile properties of the samples were measured with an Instron 4204 tensile testing machine applying the standard ISO 6239-1986 for small test specimens. The specimens were die-cut with a bone shaped die-cut head from the same 2.0 mm thick polymer plate as the specimens for DMA tests. To find out the difference on tensile properties occurred by different preparing methods of the samples, some parallel tests were also run with injection moulded specimens. The moulding temperatures were between 70 to 150°C and the injection moulding pressure was 6 bar. The tensile tester was equipped with 1 kN load cell and was operated at crosshead speed of 20 mm·min<sup>–1</sup>. The tensile strength, strain and modulus of the polymers were



measured for three to five parallel specimens that had been air-conditioned for 72 h at 23°C and 50% relative humidity.

The first series of recovery tests were run on an Instron 4204 tensile testing machine using the same type of small die-cut bone shaped test specimens as on tensile testing. The crosshead speed was 20 mm·min<sup>-1</sup> and the samples were strained to 100% elongations. After 10 minutes recovery time the permanent deformations were measured. Tests were carried out in duplicate for air-conditioned specimens. The second series of recovery tests were run by Perkin-Elmer 7 Series DMA instrument for film samples. The dimensions of the film shaped samples were 5×17 mm, and they were cut out from 0,1 mm thick hot-pressed polymer film. The samples were tested in tensile mode. Constant stress of 2 MPa (1 MPa for TPE(70/30-1)-b-(100-5)) was applied for 10 minutes and the %-strain was observed as function of time. After 10 minutes, the stress was dramatically dropped to 9 kPa which was used as zero-stress to enable observing of strain during the 20 minutes recovery time. The permanent deformations [%] were calculated from the ratio of permanent strain after 20 minutes recovery time to maximum strain of the tested film samples.

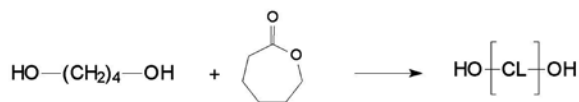
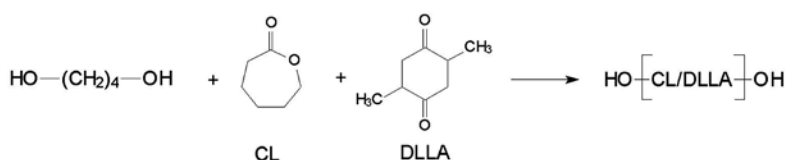
### 3. Results and discussion

#### 3.1. Polymerizations

The preparation of poly(ester-urethane)s consisted of two steps, as shown in Figure 1. The precursors, i.e. soft and hard blocks of a poly(ester-urethane) multiblock copolymer, prepared in the first step differed from each other both structurally and in molecular weights. The three types of soft blocks prepared were amorphous poly(ε-caprolactone/D,L-lactide) copolymers with number average molar masses around 13 000 g/mol. They differed from each other in molar ratios of monomers CL/DLLA by values of 30/70, 50/50 and 70/30. Each of these three soft blocks were linked separately with two semi-crystalline poly(ε-caprolactone) precursors of different molecular weight, i.e., with hard blocks of different size. The number average molecular weights of the two hard blocks were 22 900 and 11 500 g/mol. In addition, soft block P(70/30-1) was linked with a small hard block P(100-5) with size of 2400 g/mol. Copolymer precursor P(30/70-1) and PCL precursor P(100-0,5) were linked as such to act as references and enable comparison with TPEs. The compositions of precursors and TPEs are presented in Table 1.

The precursors and the PEU elastomers were characterized with SEC and <sup>1</sup>H-NMR both indicating

Formation of polyester precursors



Formation of poly(ester-urethane)

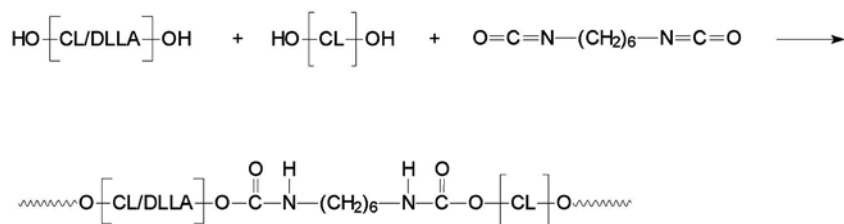


Figure 1. Reaction scheme of poly(ester-urethanes)

**Table 1.** Overview of the characterizations of precursors and TPEs

Sample P(CL/DLLA-BD)	Theoretical		SEC <sup>b</sup>			<sup>1</sup> H-NMR
	M <sub>n</sub> [g/mol]	LA <sup>a</sup>	M <sub>n</sub> [g/mol]	M <sub>w</sub> [g/mol]	MWD	LA <sup>a</sup>
P(30/70-1)	13 600	70	21 700	33 400	1.5	71.9
P(50/50-1)	13 000	50	17 200	24 600	1.4	48.8
P(70/30-1)	12 400	30	23 400	37 000	1.6	31.0
P(100-0.5)	22 900	–	39 900	59 300	1.5	–
P(100-1)	11 500	–	25 000	38 500	1.5	–
P(100-5)	2 400	–	4 900	5 800	1.2	–
TPE(30/70-1)-b-(100-0.5)	–	23.3	118 000	304 100	2.6	24.3
TPE(30/70-1)-b-(100-1)	–	35.0	64 700	188 300	2.9	35.6
TPE(50/50-1)-b-(100-0.5)	–	16.7	84 100	276 800	3.3	17.1
TPE(50/50-1)-b-(100-1)	–	25.0	91 000	212 400	2.3	24.8
TPE(70/30-1)-b-(100-0.5)	–	10.0	86 700	200 100	2.3	9.6
TPE(70/30-1)-b-(100-1)	–	15.0	113 300	258 800	2.3	15.5
TPE(70/30-1)-b-(100-5)	–	25.0	97 200	208 300	2.1	25.8
refP(100-0.5)	–	–	156 500	375 200	2.4	–
refP(30/70-1)	–	70	63 900	156 100	2.4	71.1

<sup>a</sup>D,L-lactide units per 100 monomer units<sup>b</sup>Determined relative to polystyrene standards

that the polymerizations had been successful. The results are presented in Table 1. Similarly to earlier studies of our group, the molecular weights of the precursors determined by SEC were almost twice the theoretical due to the calibration of the SEC with polystyrene standards [1]. The CL/DLLA ratios in copolymers were calculated from the <sup>1</sup>H-NMR spectra by comparing the peaks 2,28 ppm for CL and 5,14 ppm for DLLA. The compositions of copolymers were close to theoretical, as seen from

the lactide contents shown in the Table 1. After linking reaction the PEUs contained 3–8 precursors as estimated from the number average molecular weights listed in Table 1.

### 3.2. Thermal and dynamic mechanical properties

Thermal and dynamic mechanical properties of precursors and PEUs were characterized by DSC

**Table 2.** Thermal and dynamic mechanical properties of precursors and TPEs

Sample P(CL/DLLA-BD)	DSC				T <sub>g</sub> (E'') [°C]	DMA	
	T <sub>g</sub> [°C]	T <sub>m</sub> [°C]	ΔH [J/g]	DCrys [%]		T <sub>g</sub> (tanδ) [°C]	H(tanδ) <sup>a</sup>
P(30/70-1)	8	–	–	–			
P(50/50-1)	–13	–	–	–			
P(70/30-1)	–41	–	–	–			
P(100-0.5)	–	57	–72	52			
P(100-1)	–	56	–79	57			
P(100-5)	–	47	–91	65			
TPE(30/70-1)-b-(100-0.5)	–	57	–39	28	13	16	0.31
TPE(30/70-1)-b-(100-1)	–	55	–33	24	11	17	0.57
TPE(50/50-1)-b-(100-0.5)	–8	58	–41	29	–7	–3	0.25
TPE(50/50-1)-b-(100-1)	–12	54	–25	18	–10	–3	0.45
TPE(70/30-1)-b-(100-0.5)	–48	56	–48	34	–55	–33	0.09
TPE(70/30-1)-b-(100-1)	–36	53	–39	28	–44	–23	0.18
TPE(70/30-1)-b-(100-5)	–40	32	–4	3	–38	–26	0.47
refP(100-0.5)	–	60	–66	47	–	–	–
refP(30/70-1)	14	–	–	–	12	21	3.29

<sup>a</sup>Height of the tanδ peak at T<sub>g</sub>

and DMA and the results are presented in Table 2. The DSC results were obtained during the second heating scan to erase the thermal history of the sample. In the DSC spectra of copolymer precursors, no signs of melting behavior were detected, supporting the hypothesis of highly transesterified semi-random structure of copolymers leading to amorphous structure. By increasing the DLLA content [mol%] in the precursor from 30 to 70, the  $T_g$  detected increased dramatically from  $-41$  to  $+8^\circ\text{C}$ . For the semi-crystalline PCL precursors  $T_g$  could not be detected, but the melting peaks in DSC spectra were clear. The degree of crystallinity of PCL precursors varied between 52–65%. The crystallinity determination was made by comparing of melting enthalpies of precursors with melting enthalpy of 100% crystalline PCL (139,5 J/g) [22]. As assumed, the thermal properties of the precursors were combined in the TPEs. In Figure 2, the DSC spectra of two precursors P(50/50-1) and P(100-1) as well as the spectrum of the resulting poly(ester-urethane) TPE(50/50-1)-b-(100-1) are plotted one upon the other. In the spectrum of TPE both  $T_g$  and melting peaks of the precursors are obtained, indicating of successful linking. Both  $T_g$  and  $T_m$  of all TPEs were between the corresponding values of precursors. The degree of crystallinity values of TPE-PEUs increased from 3 to 34%, apparently depending on the molecular weight of the hard precursor in the TPE multiblock copolymer. The degree of crystallinity of TPEs was calculated in the same way as for PCL homopolymer precursors by comparing the melting enthalpies of the samples with 100% crystalline PCL without

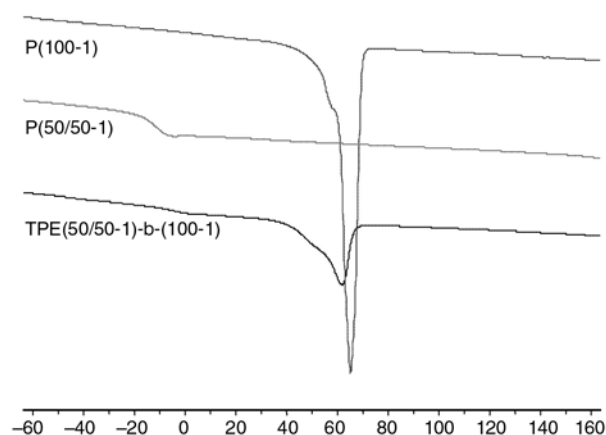


**Figure 2.** DSC spectra of TPE(50/50-1)-b-(100-1) and the precursors

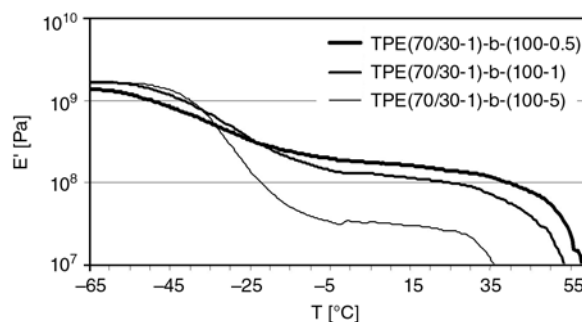


**Figure 3.** Storage modulus curves of TPEs

normalization to the PCL, the obtained values still being unexpected low ( $-10\ldots-20\%$ ).

DMA was used to study the temperature dependence of the moduli of the PEU elastomers. In a DMA scan,  $T_g$  was evaluated with two separate values presented in Table 2. These were the temperature where the peak occurred in  $\tan\delta$  curve and the temperature of the maximum in the loss modulus curve. The height of the  $\tan\delta$  peak at  $T_g$  was presented to express the magnitude of the transition. As expected, both  $T_g$  values evaluated by DMA were in good correlation with  $T_g$  values by DSC. As the degree of crystallinity increased, the height of the  $\tan\delta$  peak at  $T_g$  decreased in linear correlation. Similar to cross-linked elastomers [1], the rubbery plateau in the storage modulus curves between  $T_g$  and terminal flow region was clearly detectable indicating elastic behavior of TPEs. The storage modulus curves of elastomers TPE(70/30-1)-b-(100-5), TPE(70/30-1)-b-(100-1) and TPE(70/30-1)-b-(100-0.5) are plotted in Figure 3 to emphasize the plateau region. The increasing size of the crystalline PCL block in TPEs lengthened the rubbery plateau towards higher temperatures, as can be seen in the Figure 3.

### 3.3. Morphology studies

The contrast for morphological characterization was examined by TEM. In Figure 4, the TEM images of elastomers A: TPE(70/30-1)-b-(100-5), B: TPE(70/30-1)-b-(100-1) and C: TPE(70/30-1)-b-(100-0.5) were plotted next to each other with a view to emphasize the role of the size of the hard block, i.e., degree of crystallinity, in the separation of amorphous and crystalline phases. These and similar series of images can be taken from elastomers consisting of same type of amorphous soft block, differing from each other in the size of the

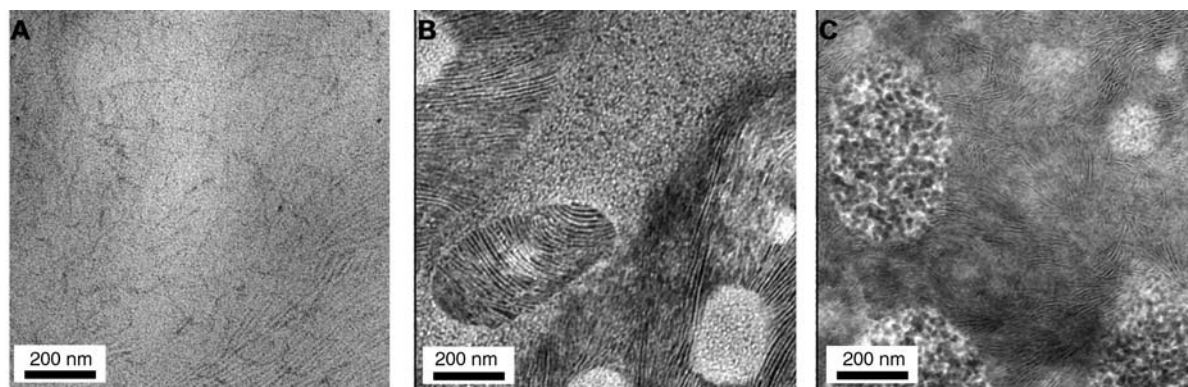


**Figure 4.** TEM images of elastomers A: TPE(70/30-1)-b-(100-5), B: TPE(70/30-1)-b-(100-1) and C: TPE(70/30-1)-b-(100-0.5)

hard block. The degree of crystallinity increases from left to right by the values: A: 3%, B: 24% and C: 34%. In the TEM images, dark color indicates the amorphous areas while white is the color of crystalline phase. This results from the tendency of amorphous materials to permeate  $\text{RuO}_4$  stain more readily than crystalline ones. In all three images, some crystallinity or lamellar areas can be detected, while the images B and C show significantly more lamellas than image A. Also, in images B and C the phase separation of amorphous and crystalline areas was clearly detectable.

### 3.4. Mechanical properties

The tensile properties of the PEU-TPEs were measured by Instron 4204 tensile testing machine, and tensile strength, strain and modulus are presented in Figure 5. In the multiblock copolymer TPEs, the tensile properties of both precursors were combined, which is easily observed by comparing the

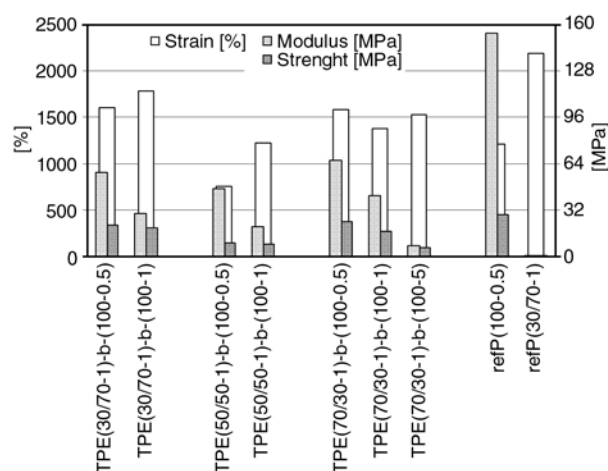


**Figure 5.** Mechanical properties of elastomers

results with results of the reference PEUs denoted refP(100-0.5) and refP(30/70-1). By increasing the molecular weight of the hard block in a PEU-TPE, i.e., increasing the degree of crystallinity, the modulus and strength increased as well. The copolymer with composition of 50/50 had slightly lowest mechanical properties. The elastomers were so resilient that when the gauge lengths of the dog-bone specimens were drawn out the specimens only did not break but also the ends of the specimens between the grip holders began to strain. This caused false strain values by increasing the actual maximum strain percent. However, this quasi-elongation was detectable in strain-stress diagrams, and it was possible to be eliminated from the results. Anyway, the maximum strain percent values of the elastomers were very high, >2000%. PCL is known to be highly elastic as proved by the reference PEU refP(100-0.5) with maximum strain of 1200%. However, D,L-lactide still increased elongation so that the PEU-TPEs with the highest lactide contents of the soft copolymer block had the highest maximum strain percent values, i.e., from 1600 to 1800%. The fully amorphous reference polymer refP(30/70-1) without crystalline PCL blocks strained >2000%.

To examine the role of preparation technique of the test specimens to the tensile test results, two TPEs were also tested with extruded specimens. Figure 6 illustrates the difference in results caused most likely by orientation of linear polymer chains during the extrusion. The die-cut samples showed dramatically lower modulus and strength values compared with extruded specimens. This can be explained by the hardening occurred by orientation of polymer chains. Some of the die-cut samples



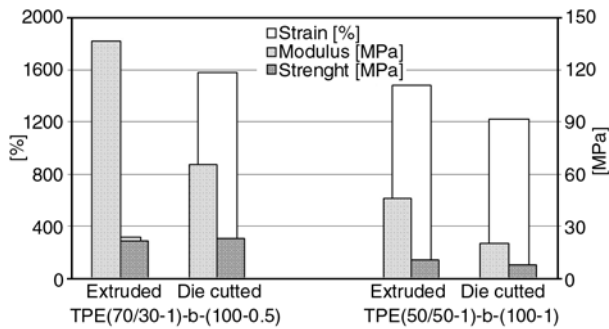


**Figure 6.** The role of different preparing techniques of the samples in mechanical properties of elastomers

were slightly blistered, and the changes in quality of the specimens might affect results as well.

### 3.5. Creep recovery properties

The creep recovery properties of the TPEs were measured with two different test procedures both using the tensile mode. The first test series were run by Instron 4204 tensile testing machine with dog-bone specimens, and second series by DMA Perkin-Elmer 7 Series instrument for film samples. In the first test series the specimens were strained to 100% elongation once, relaxed, and after 10 min relaxation time the permanent deformations were measured. The stresses needed for 100% straining varied much depending on the materials. In the second test series constant stress was applied for 10 min before relaxation to point out the effect of orientation of polymer chains. In both tests, the composition of the amorphous block of the copolymer did not have significant effect on recovery

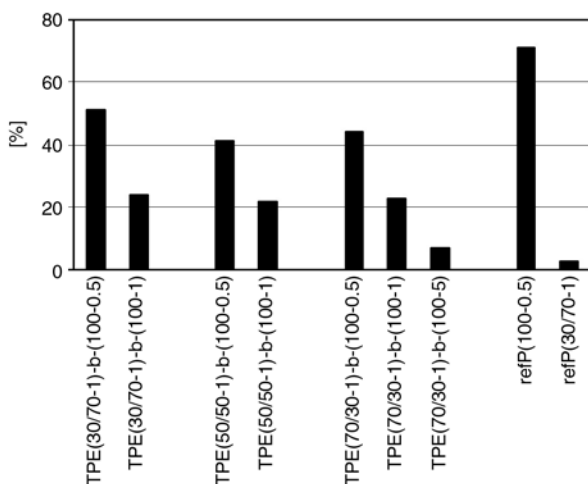


**Figure 7.** Permanent deformations of elastomers after recovery from 100% strain

properties whereas these properties were mainly dominated by the size of the hard block of them, i.e., the degree of crystallinity. The TPEs having a copolymer with CL/DLLA ratio 50/50 as soft block, recovered slightly worse than other TPEs, as could be expected on basis of tensile testing. The results of the first creep recovery test after 100 percent elongation are presented in Figure 7. The lower the overall degree of crystallinity is the smaller is the permanent deformation of the specimens. These results describe the recovery properties of single, short-term deformation of material when no orientation of polymer chains obviously occurs. When orientation apparently is involved in long-term tests, as in our second test series, the results were different as shown in Figures 8 and 9.

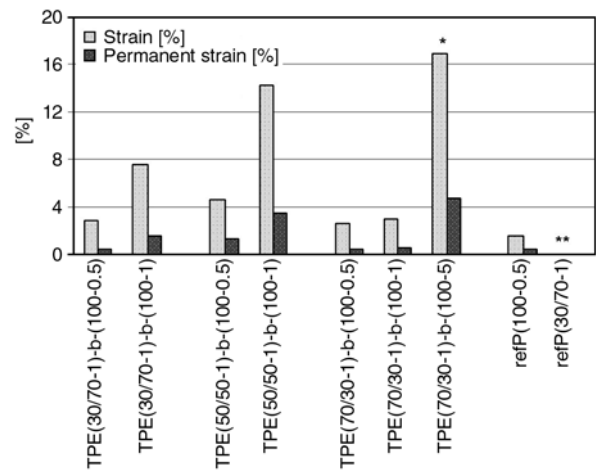


**Figure 8.** Strain after 10 minutes applied stress (2 N, \*1 N) and permanent strain after 20 minutes recovery time of elastomers. (\*Not measured, sample too soft)

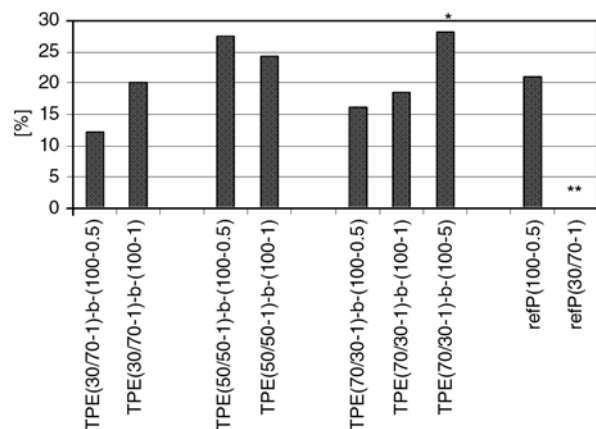


**Figure 9.** Permanent deformations after 10 minutes applied stress (2 N, \*1 N) and 20 minutes recovery time of elastomers. (\*\*Not measured, sample too soft)

Under the same constant stress, TPEs with lower overall degree of crystallinity not only strained more but also the relative permanent deformation was higher than for elastomers with higher degree of crystallinity. This supports the assumption that crystalline phases are required to enhance recovery properties of TPEs.

#### 4. Conclusions

In this study, poly(ester-urethane) thermoplastic elastomers (PEU-TPEs) were prepared by simple two-step melt polymerization technique. On basis of tensile testing the products were elastic showing at the same time feasible strength values. The TEM images of the products revealed morphological feature of elastomers by the fact that phase separation of the crystalline and amorphous phases was clearly observed when the degree of crystallinity increased. As known, phase separation is required for good creep resistance. The recovery properties of the products were promising, and by modification of the polymer composition further still better creep resistance can obviously be achieved. The distinct rubbery plateau in storage modulus curves confirmed, too, the elastic behaviour of the TPEs. However, one important feature to be studied in the future is the conservation of mechanical properties during hydrolytic degradation of PEU-TPEs.

#### Acknowledgements

This work has been carried out within the Bio- and Nanopolymers Research Group, which is funded by the Academy of Finland (CoE program code number 211493).

#### References

- [1] Helminen A. O., Korhonen H., Seppälä J. V.: Cross-linked poly( $\epsilon$ -caprolactone/*D,L*-lactide) copolymers with elastic properties. *Macromolecular Chemistry and Physics*, **203**, 2630–2639 (2002).
- [2] Bates F. S., Fredricson G. H.: Block copolymer thermodynamics: Theory and experiment. in: 'Thermoplastic elastomers' (eds.: Holden G., Legge N. R., Quirk R. P., Schroeder H. E.) Hanser/Gardner, Cincinnati, USA, 401–426 (2004).
- [3] Hiltunen K., Seppälä J. V., Härkönen M.: Lactic acid based poly(ester-urethanes): Use of hydroxyl terminated prepolymer in urethane synthesis. *Journal of Applied Polymer Science*, **63**, 1091–1100 (1997).
- [4] Hiltunen K., Seppälä J. V., Härkönen M.: Lactic acid based poly(ester-urethane)s: The effects of different polymerization conditions on the polymer structure and properties. *Journal of Applied Polymer Science*, **64**, 865–873 (1997).
- [5] Härkönen M., Hiltunen K., Malin M., Seppälä J. V.: Properties and polymerization of biodegradable thermoplastic poly(ester-urethane). *Journal of Macromolecular Science, Part A: Pure and Applied Chemistry*, **32**, 857–862 (1995).
- [6] Kylmä J., Härkönen M., Seppälä J. V.: The modification of lactic acid based poly(ester-urethane) by copolymerization. *Journal of Applied Polymer Science*, **63**, 1865–1872 (1997).
- [7] Kylmä J., Seppälä J. V.: Synthesis and characterization of a biodegradable thermoplastic poly(ester-urethane) elastomer. *Macromolecules*, **30**, 2876–2882 (1997).
- [8] Helminen A., Kylmä J., Tuominen J., Seppälä J. V.: Effect of structure modification on rheological properties of biodegradable poly(ester-urethane). *Polymer Engineering and Science*, **40**, 1655–1662 (2000).
- [9] Cohn D., Salomon A. H.: Designing biodegradable multiblock PCL/PLA thermoplastic elastomers. *Biomaterials*, **26**, 2297–2305 (2005).
- [10] Stirna U. K., Tupureina V. V., Sevast'yanova I. V., Dzene A. V., Misane M. M., Vilsone D. M.: Synthesis, structure, and properties of poly(ester-urethanes) based on glycerol monostearate. *Polymer Science, Series A*, **45**, 765–772 (2003).
- [11] Teng C., Yang K., Ji P., Yu M.: Synthesis and characterization of poly(L-lactic acid)-poly( $\epsilon$ -caprolactone) multiblock copolymers by melt polycondensation. *Journal of Polymer Science, Part A: Polymer Chemistry*, **42**, 5045–5053 (2004).
- [12] Huang M-H., Li S., Vert M.: Synthesis and degradation of PLA-PCL-PLA triblock copolymer prepared by successive polymerization of  $\epsilon$ -caprolactone and DL-lactide. *Polymer*, **45**, 8675–8681 (2004).
- [13] Zhang Z., Grijpma D. W., Feijen J.: Triblock copolymers based on 1,3-trimethylene carbonate and lactide as biodegradable thermoplastic elastomers. *Macromolecular Chemistry and Physics*, **205**, 867–875 (2004).
- [14] Kim J-H., Lee S. Y., Chung D. J.: Synthesis and properties of triblock copolymers from L-lactide and trimethylene carbonate. *Polymer Journal*, **32**, 1056–1059 (2000).
- [15] Pospiech D., Komber H., Jehnichen D., Häussler L., Eckstein K., Scheibner H., Janke A., Kricheldorf H. R., Petermann O.: Multiblock copolymers of L-lactide and trimethylene carbonate. *Biomacromolecules*, **6**, 439–446 (2005).
- [16] Frick E. M., Hillmyer M. A.: Synthesis and characterization of polylactide-block-polyisoprene-block-poly-lactide triblock copolymers: New thermoplastic elastomers containing biodegradable segments. *Macromolecular Rapid Communications*, **21**, 1317–1322 (2000).

- [17] Messman J. M., Scheuer A. D., Storey R. F.: Synthesis and characterization of A-B-A triblock copolymers derived from chloro-telechelic poly(L-lactide): Combining ring-opening polymerization (ROP) and atom transfer radical polymerization (ATRP). *Polymer*, **46**, 3628–3638 (2005).
- [18] Jeon O., Lee S-H., Kim S. H., Lee Y. M., Kim Y. H.: Synthesis and characterization of poly(L-lactide)-poly( $\epsilon$ -caprolactone) multiblock copolymers. *Macromolecules*, **36**, 5585–5592 (2003).
- [19] Cohn D., Hotohely-Salomon A.: Biodegradable multiblock PEO/PLA thermoplastic elastomers: Molecular design and properties. *Polymer*, **46**, 2068–2075 (2005).
- [20] Hiljanen-Vainio M., Karjalainen T., Seppälä J. V.: Biodegradable lactone copolymers. I. Characterization and mechanical behavior of  $\epsilon$ -caprolactone and lactide copolymers. *Journal of Applied Polymer Science*, **59**, 1281–1288 (1996).
- [21] Brown G. M., Butler J. H.: New method for the characterization of domain morphology of polymer blends using ruthenium tetroxide staining and low voltage scanning electron microscopy (LVSEM). *Polymer*, **38**, 3936–3945 (1997).
- [22] Perrin D. E., English J. P.: Polycaprolactone. in 'Handbook of Biodegradable Polymers' (eds.: Domb A. J., Kost J., Wiseman D. M.) Harwood Academic Publishers, Amsterdam, 63–77 (1997).

# Effects of silicon surfactant in rigid polyurethane foams

H. Lim<sup>2</sup>, S. H. Kim<sup>1</sup>, B. K. Kim<sup>1\*</sup>

<sup>1</sup>Department of Polymer Science and Engineering Pusan National University, Busan 609-735, Korea

<sup>2</sup>Korea Polyol Co., Ulsan 680-090, Korea

Received 28 November 2007; accepted in revised form 29 January 2008

**Abstract.** The rigid polyurethane foams (RPUFs) have been fabricated from high functional crude 4,4'-di-phenylmethane diisocyanate (CMDI) and polypropylene glycols (PPGs) for a wide range of surfactant concentration with an environmentally friendly blowing agent (HFC 365mfc). Cream time, gel time, and tack-free time increased with the addition of surfactant. Foam density decreased rapidly to a minimum at 0.5 pphp (part per hundred polyol) surfactant due to the increased blowing efficiency with surfactant. Surface tension rapidly decreased to an asymptotic value at 2 pphp surfactant. In accordance with this, cell size decreased and closed cell content increased rapidly to constant values at low surfactant concentrations (<1 pphp). The decrease of cell size was accompanied by the decrease of thermal conductivity to give a linear relationship between the two implying that the series model of heat transfer is applicable.

**Keywords:** thermal properties, rigid polyurethane foam (RPUF), cell structure, compression strength, thermal conductivity

## 1. Introduction

Polyurethanes (PUs) are used as coatings, adhesive, sealants, elastomers (CASE), and fibers as well as flexible, semi-rigid and rigid foams [1–3]. Among them, rigid PU foams (RPUFs) have closed cell structure with low thermal conductivity, high compression strength, low density, high strength-to-weight ratio, and low moisture permeability [2–4]. Consequently, RPUFs finds such applications as insulations of refrigerators, freezers, piping, tanks, ship building, and LNG cargos [5–8].

The foaming can be done by one shot or two shot methods. In one shot method, all materials are put into a mixing cup and mixed homogeneously before they are poured into a mold. In the two shot method, isocyanate is added to the mixture at the second stage. The foaming can be carried out with a physical blowing agent, chemical blowing agent, or with a mixture of the two [5]. In physical blowing, reactions between isocyanate and polyol produce

polyurethane linkages with the emission of heat of reaction. Then, the blowing agent vaporizes and the gas trapped in the closed cells of the foam [9]. Typically, thermal conductivity of the blown gas is very low. This, with small closed cell structure gives extremely low thermal conductivity of the RPUFs. In chemical blowing, water (most widely used blowing agent) reacts with isocyanate to form unstable carbamic acid which immediately decomposes into an amine and carbon dioxide [2, 10, 11]. Recently, many of the conventional blowing agents such as monofluorotrichloromethane (R11) and difluorodichloromethane (R12) have been suggested to contribute to the depletion of the stratospheric ozone layer and the use has been regulated in many countries. Consequently, the use of environmentally friendly blowing agents has become an important and urgent issue in the synthesis of polyurethane foam [12–14]. Water can in part replace such environmentally hazardous blowing

\*Corresponding author, e-mail: [bkkim@pnu.edu](mailto:bkkim@pnu.edu)  
© BME-PT and GTE



agents. However, the excessive use of water causes a negative pressure gradient due to the rapid diffusion of CO<sub>2</sub> through the cell wall causing cell deformation [2, 3, 15, 16].

The kinetics of RPUF formation mainly depends on the rates of blowing and gelling reactions, which on the other hand are respectively governed by an amine and a tin catalyst [4, 6]. On the other hand, the properties of the foam mainly depend on the type of polyol such as functionality and hydroxyl value, and type and amount of surfactant, and blowing agent. To reinforce the foam, composites with particle, clays and fiber have been considered [17–21].

As far as the present authors are concerned, systematic investigations of the effects of surfactant on various properties of RPUF are sparse, perhaps except those blown with water [7, 22]. We synthesized various types of RPUFs from CMDI and polypropylene glycols (PPGs) with an environmentally friendly physical blowing agent, viz. HFC 365mfc (CF<sub>3</sub>CH<sub>2</sub>CF<sub>2</sub>CH<sub>3</sub>), with a potential target application of insulation panel of LNG cargo where high compression strength as well as thermal insulation is highly desired. The effects of silicon surfactant concentration on the performances of the foams have been extensively analyzed in terms of reactivity, cell morphology, surface tension, and mechanical and thermal properties of the foams.

## 2. Experimental

### 2.1. Raw materials

Two types of PPG having hydroxyl value (OHV, mg KOH/g of sample) of 450 and 400 (HR-450P and KR-403) were provided by Korea Polyol Co (Korea). The CMDI was provided by Huntsman (Suprasec-5005), HFC 365mfc by Solvay Chemicals (Belgium), and Polycat-8 as foaming catalyst by Air Products. Silicon surfactant (B 8404) known to augment the closed cell content thus providing improved thermal insulation was provided by Goldschmidt. PPGs were dehydrated before use at 90°C for 24 h in a vacuum oven. Other chemicals were used as received.

### 2.2. Preparation of samples

The rigid foams were synthesized by one shot method. All raw materials were first put into a mix-

**Table 1.** Formulation to synthesize the RPUFs

Components	Compositions [g]
HR-450P	80
KR-403	20
Polycat-8	1
B 8404	Variable (0, 0.2, 0.5, 1.0, 2.0, 5.0 pphp)
HFC 365mfc	10.1
CMDI	116.9
Index	110

HR-450P; hydroxyl value 450, Initiator; glycerin and sucrose + PO  
KR-403; hydroxyl value 400, Initiator; toluene diamine + PO

ing vessel (Ultra-Turrox T-50, Ika-Werke) and mixed for 30 s at 7000 rpm. Then the mixtures were discharged to an open mold (200×200×200 mm) and the foam cake was cured for 1 week at room temperature. The NCO index (isocyanate equivalents/polyol equivalents) was fixed at 1.10. The basic formulations are given in Table 1.

### 2.3. Characterizations

Density of the foam was measured according to ASTM D 1622 with sample size of 30×30×30 mm (width×length×thickness), and an average of at least five measurements was taken to report. The density distribution [%] was calculated according to 100×(maximum density-minimum density)/average density.

The closed cell content was determined by an air pycnometer following ASTM D 2850 with specimen dimension 50×50×25 mm. Thermal conductivity was measured using HC-074 (Laser Comp) according to ASTM C 518. The cell morphology was observed under a scanning electron microscope (SEM, HITACHI S3500N). Samples were cryogenically fractured in liquid nitrogen and gold sputtered before they were scanned in the free rising direction. Mechanical properties at room temperature were measured using a Universal Testing Machine (Ametek, Lloyd). Compression strength was determined by ASTM D 1621 at a crosshead speed of 3.0 mm/min with the sample dimension of 30×30×30 mm [7]. The force required for 10% deformation based on the original thickness has been taken as the compression strength of the foam. The surface tension was measured using Tensiometer K 100 (Kruss) according to ASTM D 1331 based on bubble pressure.

**Table 2.** Reactivity

	Without silicone surfactant	With silicone surfactant
Cream time [s]	57	60~62
Gel time [s]	180	198~206
Tack-free time [s]	220	240~250

### 3. Results and discussion

#### 3.1. Kinetics of foam formation

Kinetics of the foam formation is followed by the cream time, gel time and tack-free time [4, 6, 10]. The cream time corresponds to the start of bubble rise and hence color of the mixture becomes cream-like from dark brown due to the introduction of bubbles. Gel time is the starting point of stable network formation by intensive allophanate crosslinks as well as urethane. At the tack-free time, the outer surface of the foam loses its stickiness and the foam can be removed from the mold. Table 2 shows that cream time, gel time and tack-free time increase with increasing surfactant concentration, implying that the surfactant reduces diffusion across the interfaces. The PPGs are incompatible with CMDI and the reaction mixtures are heterogeneous. For this reason surfactants should carry high surface activity to act as a nucleation supporter and good emulsifying ability for the raw materials and blowing agents [3].

#### 3.2. Foam density and density distribution

Density is a most important parameter to control the mechanical and thermal properties [23] of closed cell foams [2, 3]. With increasing surfactant concentration, foam density decreases asymptotically to a small minimum at 0.5 pphp, beyond which the increase is marginal (Figure 1). Similar results were obtained by Krupers *et al.* [22] who reported that average foam height increases, i.e., density decreases with the addition and increasing amount of fluorosurfactant. This implies that the blowing efficiency is increased with the addition of surfactant by supporting the ability to create nuclei and augmenting the stability of the foams. It seems that the surfactant in excess is not interposed at the interfaces and rather increases the heterogeneity of the system. Foam density decreases along the bubble rising direction i.e., from bottom to top due to the gravity

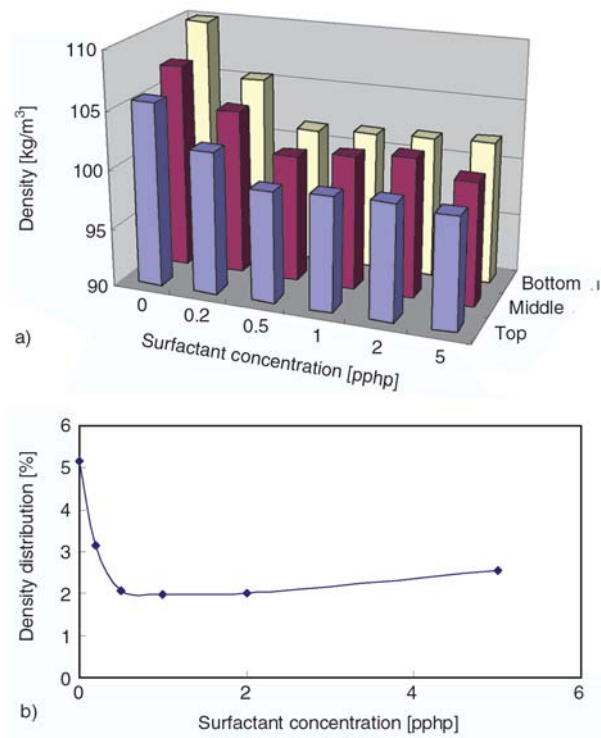


**Figure 1.** Densities (a) and density distributions (b) of the RPUFs vs. surfactant concentration

effect giving rise to great compression at bottom. The density distribution along the rise direction also shows similar surfactant dependence as density, i.e., the density variation shows a minimum at 0.5 pphp surfactant.

#### 3.3. Surface tension and cell morphology

The exothermic heat of reaction causes the supersaturation of the reactive mixture resulting in phase separation into gas, followed by diffusion into the nuclei which are small air bubbles entrapped during the mixing of raw materials [24]. Then the nuclei grow into bubbles and spherical cells by adopting

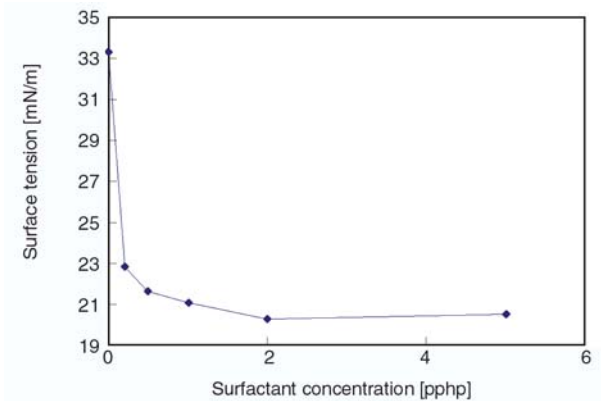


**Figure 2.** Surface tensions of the RPUFs vs. surfactant concentration

more gases or by coalescence with neighboring ones. As the blow ratio increases the spherical bubbles are eventually separated by the cell membrane and become polyhedral.

The surface tension of the polyol for various surfactant concentrations are shown in Figure 2 which shows that the surface tension decreases rapidly to an asymptotic value at 2 pphp. The asymptotic value of surface tension is approximately 2/3 of the surfactant-free value.

SEM micrograph shows that the foams consist of cells of spherical and polyhedral shape (Figure 3). Cell size (Figure 4) decreases rapidly to an asymptotic value of about 140  $\mu\text{m}$  with the addition of surfactant. Cell size as small as 100  $\mu\text{m}$  was also reported with fluorosurfactant [22]. On the other hand, the closed cell content (Figure 5) increases asymptotically with increasing surfactant concentration due to the decrease in surface tension. The increase of closed cell content is accompanied by

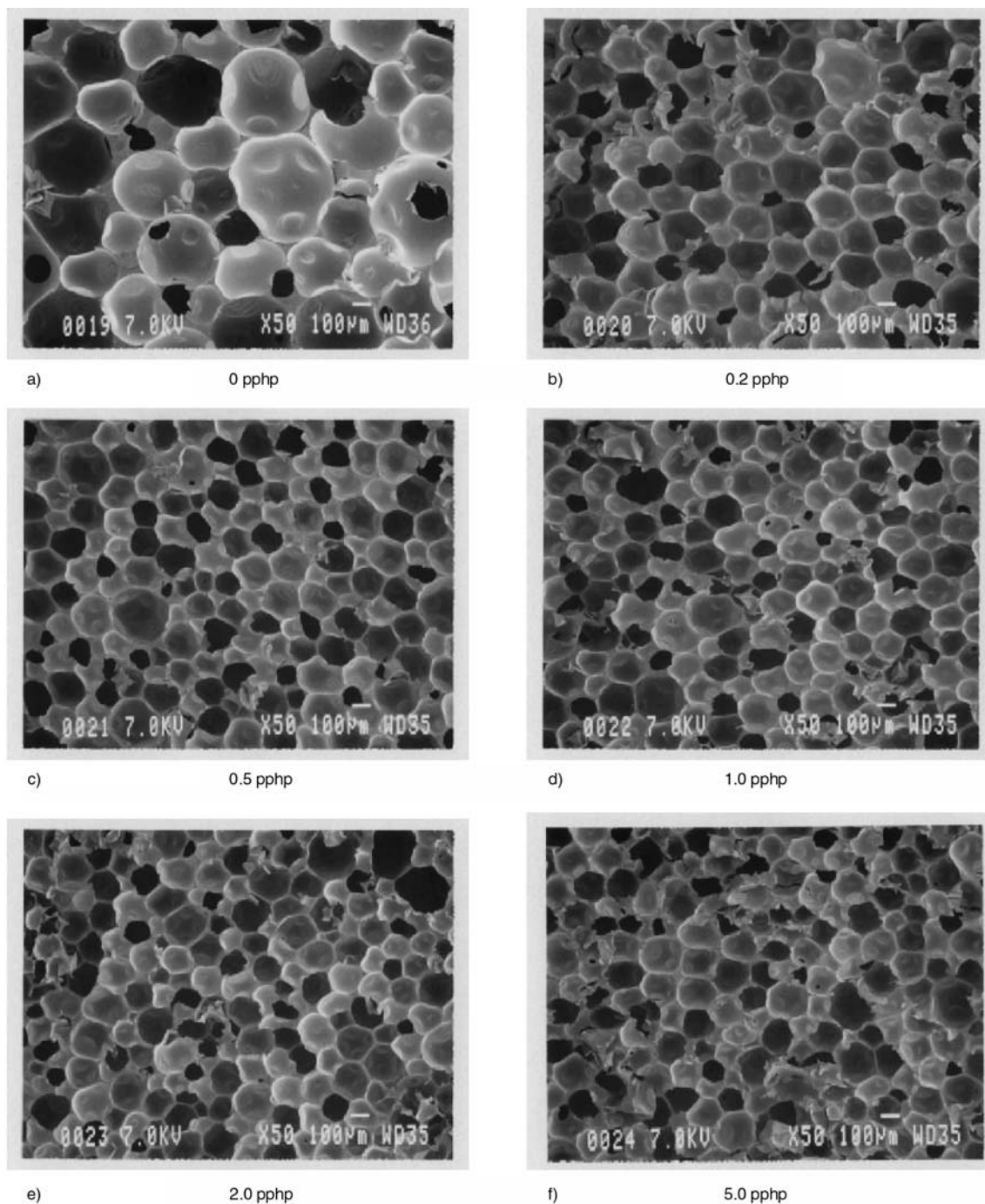


**Figure 3.** SEM micrographs of the RPUFs vs. surfactant concentration

**Table 3.** Porosities of the RPUFs

Surfactant [pphp]	0	0.2	0.5	1	2	5
Porosity [%]	89.6	89.2	90.0	90.3	89.6	89.7
Closed porosity [%]	63.3	82.8	84.3	84.7	84.1	84.6
Open porosity [%]	26.3	6.4	5.7	5.6	5.5	5.1

Porosity was calculated using the resin density of 980 kg/m<sup>3</sup>

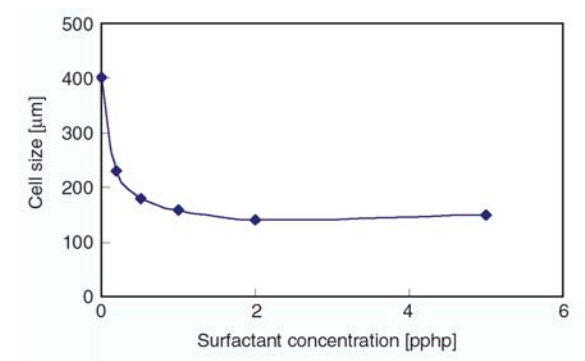


**Figure 4.** Cell size of the RPUFs vs. surfactant concentration

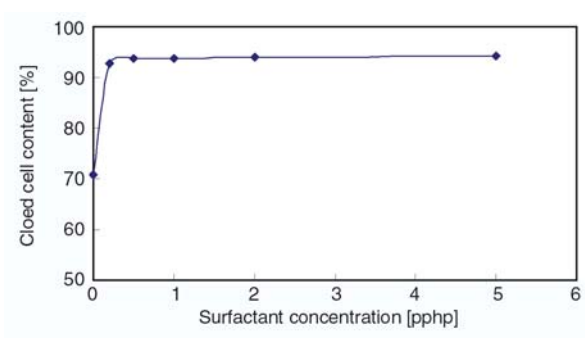


**Figure 5.** Closed cell contents of the RPUFs vs. surfactant concentration

the increase of closed porosity while the full porosity is kept almost constant (Table 3). This implies that closed cell content and porosity as well as the cell size are closely controlled by the amount of surfactant being added.

### 3.4. Compression strength

The compression strength is closely related to the dimensional stability of closed cell foams. As the temperature goes up, gas pressure inside the cell increases, and the pressure difference relative to the atmospheric pressure becomes great. If the foam is to be dimensionally stable under these conditions, the compression strength must be greater than the pressure rise [2]. The minimum compression strength of 0.1 MPa is generally recommended for closed cell foam [6].

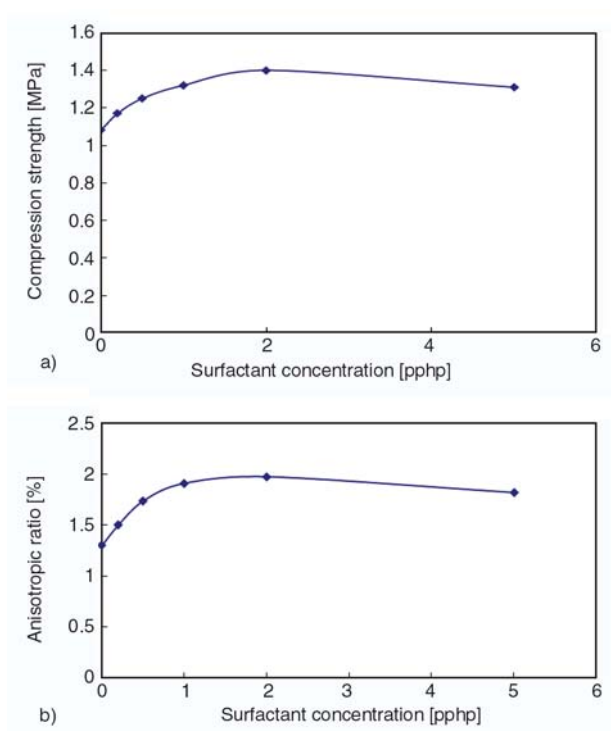


**Figure 6.** Compression strengths (a) and strength anisotropies (b) of the RPUFs vs. surfactant concentration

The compression strength of our foam is greater than 0.97 MPa (perpendicular). In contrast to the density decrease, strength and its anisotropy (strength ratio of parallel to perpendicular direction) smoothly increases with increasing concentration of surfactant with a maximum at 2 pphp (Figure 6). An earlier work showed simultaneous decreases of compression strength with increasing surfactant concentration [7]. It seems that the compression strength is closely related to the closed cell content and cell size when the density variation is insignificant

### 3.5. Thermal conductivity of the foam

Heat conduction through the closed cell foams can be approximated by a series model which is composed of polymer walls and gas cells in series [25].



Conductive heat flux ( $q$ ) through the composite wall is given by Equation (1):

$$q = \frac{\Delta T}{R} \quad (1)$$

where  $\Delta T$  is the temperature drop across the foam and  $R$  is the conduction resistance given by the following Equation (2):

$$R = \sum_{i=1}^n \left( \frac{X_{W,i}}{k_W} + \frac{X_{G,i}}{k_G} \right) \quad (2)$$

Here  $X_{W,i}$  and  $X_{G,i}$  are the cell wall thickness and cell dimension, and  $n$  is the number of polymer walls, respectively. For uniform cells, wall thickness ( $X_{W,i}$ ) and cell dimension ( $X_{G,i}$ ) are constant to give Equation (3):

$$R = n \left( \frac{X_W}{k_W} + \frac{X_G}{k_G} \right) \quad (3)$$

In the typical closed cell foam, the polymer walls occupy 3–6 volume% of the foam. In addition, the conductivity of the polymer is much greater than that of the blowing gas. So, the first term, viz. polymer wall resistance can be neglected to give Equation (4):

$$R = n \left( \frac{X_G}{k_G} \right) \quad (4)$$

The above simple analysis shows that the thermal insulation of closed cell foams increase linearly with the number of closed cells, i.e., effect of insulation increases as the cell size decreases [26].

The thermal conductivity of our foam rapidly decreases to an asymptotic value at 1pphp surfac-

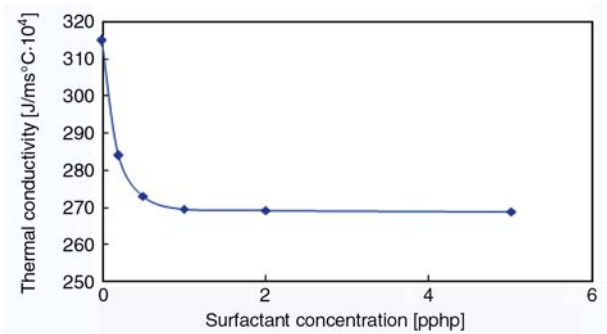


**Figure 7.** Thermal conductivities of the RPUFs vs. surfactant concentration

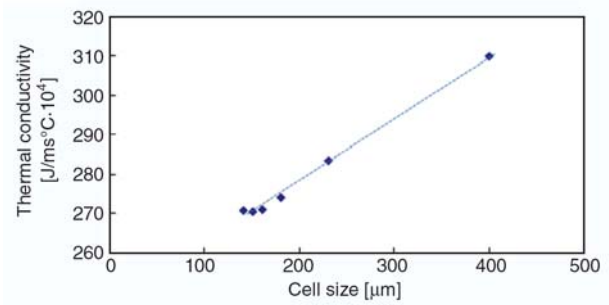


**Figure 8.** Thermal conductivities vs. cell size for the RPUFs

tant (Figure 7). The decrease is mainly due to the decreased cell size as analyzed above. To confirm this, the relationship between the thermal conductivity and cell size is plotted in Figure 8 which shows a straight line for a broad range of cell size. This implies that the series model is applicable where the wall resistance can be considered for small cells.

#### 4. Conclusions

The RPUFs have been fabricated from CMDI and PPGs as a function of surfactant concentration with an environmentally friendly blowing agent (HFC 365mfc). Cream time, gel time, and tack-free time increased with the addition of surfactant due to the increased stability of reaction mixture and rising bubbles.

Foam density and density distribution decreased rapidly to a minimum at 0.5 pphp surfactant due to the increased blowing efficiency in the presence of surfactant. Surface tension of the foam rapidly decreased to an asymptotic value at 2 pphp surfactant, implying that the reaction mixture is saturated at this concentration.

In accordance with the decreased surface tension, cell size decreased and closed cell content increased rapidly to constant values at low surfactant concentrations (<1 pphp).

The decrease of cell size was accompanied by the decrease of thermal conductivity, and a linear relationship between the two was held for a broad range of cell size. Simple analysis based on series model also gave the same result assuming the resistance of cell wall is negligible except the small cells.

## Acknowledgements

This research was supported by the Ministry of Commerce, Industry and Energy (MOCIE) and Korea Industrial Technology Foundation (KOTEF) through the Human Resource Training Project for Regional Innovation. BKK is also indebted to the National Core Research Center organized at PNU.

## References

- [1] Hepburn C.: Polyurethane elastomers. Elsevier, London (1991).
- [2] Oertel G.: Polyurethane handbook. Hanser Publishers, New York (1985).
- [3] Szycher M.: Szycher's handbook of polyurethanes. CRC Press, New York (1999).
- [4] Singh H., Sharma T. P., Jain A. K.: Reactivity of the raw materials and their effects on the structure and properties of rigid polyurethane foams. *Journal of Applied Polymer Science*, **106**, 1014–1023 (2007)
- [5] Mondal P., Khakhar D. V.: Regulation of cell structure in water blown rigid polyurethane foam. *Macromolecular Symposia*, **216**, 241–254 (2004).
- [6] Seo W. J., Park J. H., Sung Y. T., Hwang D. H., Kim W. N., Lee H. S.: Properties of water-blown rigid polyurethane foams with reactivity of raw materials. *Journal of Applied Polymer Science*, **93**, 2334–2342 (2004).
- [7] Seo W. J., Jung H. C., Hyun J. C., Kim W. N., Lee Y.-B., Choe K. H., Kim S.-B.: Mechanical, morphological, and thermal properties of rigid polyurethane foams blown by distilled water. *Journal of Applied Polymer Science*, **90**, 12–21 (2003).
- [8] Xiao Z., Guan R., Jiang Y., Li Y.: Tensile property of thin microcellular PC sheets prepared by compression molding. *Express Polymer Letters*, **1**, 217–225 (2007).
- [9] Chai J. B., Kim B. K., Shin Y. J.: Absorption of hydrophobic fluid by polyurethane foam. *Journal of Korean Industrial and Engineering Chemistry*, **9**, 648–653 (1998).
- [10] Hari Krishnan G., Khakhar D. V.: Effect of monomer temperature on foaming and properties of flexible polyurethane foams. *Journal of Applied Polymer Science*, **105**, 3439–3443 (2007).
- [11] Kwon O.-J., Yang S.-R., Kim D.-H., Park J.-S.: Characterization of polyurethane foam prepared by using starch as polyol. *Journal of Applied Polymer Science*, **103**, 1544–1553 (2007).
- [12] Antolini B., Bianchi F., Bottazzi M., Careri M., Musci M.: Development and validation of novel DH-GC-ITMS methods for the determination of freon F-141b in formulated polyol and rigid polyurethane foam. *Chromatographia*, **60**, 323–327 (2004).
- [13] Heintz A. M., Duffy D. J., Hsu S. L., Suen W., Chu W., Paul C. W.: Effects of reaction temperature on the formation of polyurethane prepolymer structures. *Macromolecules*, **36**, 2695–2704 (2003).
- [14] Widya T., Macosko C. W.: Nanoclay-modified rigid polyurethane foam. *Journal of Macromolecular Science, Part B: Physics*, **44**, 897–908 (2005).
- [15] Kim S. H., Lim H., Song J. C., Kim B. K.: Effect of blowing agent type in rigid polyurethane foam. *Journal of Macromolecular Science, Part A: Pure and Applied Chemistry*, **45**, 1–5 (2008).
- [16] Gent A. N.: Engineering with rubber: How to design rubber components. Hanser Gardner Publications, Cincinnati (2001).
- [17] Goods S. H., Neuschwanger C. L., Whinnery L. L., Nix W. D.: Mechanical properties of a particle-strengthened polyurethane foam. *Journal of Applied Polymer Science*, **74**, 2724–2736 (1999).
- [18] Cao X., Lee L. J., Widya T., Macosko C.: Polyurethane/clay nanocomposites foams: Processing, structure and properties. *Polymer*, **46**, 775–783 (2005).
- [19] Xu Z., Tang X., Gu A., Fang Z.: Novel preparation and mechanical properties of rigid polyurethane foam/organoclay nanocomposites. *Journal of Applied Polymer Science*, **106**, 439–447 (2007).
- [20] Modesti M., Lorenzetti A., Besco S.: Influence of nanofillers on thermal insulating properties of polyurethane nanocomposites foams. *Polymer Engineering and Science*, **47**, 1351–1358 (2007).
- [21] Yang Z.-G., Zhao B., Qin S.-L., Hu Z.-F., Jin Z.-K., Wang J.-H.: Study on the mechanical properties of hybrid reinforced rigid polyurethane composite foam. *Journal of Applied Polymer Science*, **92**, 1493–1500 (2004).
- [22] Krupers M. J., Bartelink C. F., Grünhauer H., Moller M.: Formation of rigid polyurethane foams with semi-fluorinated diblock copolymeric surfactants. *Polymer*, **39**, 2049–2053 (1998).
- [23] Gedde U. W.: Polymer physics. Chapman and Hall, London (1995).
- [24] Niyogi D., Kumar R., Gandhi K. S.: Water blown free rise polyurethane foams. *Polymer Engineering and Science*, **39**, 199–209 (1999).
- [25] Bird R. B., Stewart W. E., Lightfoot E. N.: Transport phenomena. Wiley, New York (2006).
- [26] Wu J.-W., Sung W.-F., Chu H.-S.: Thermal conductivity of polyurethane foams. *International Journal of Heat and Mass Transfer*, **42**, 2211–2217 (1999).

# Designing of hydroxyapatite-gelatin based porous matrix as bone substitute: Correlation with biocompatibility aspects

H. Bundela, A. K. Bajpai\*

Bose Memorial Research Laboratory, Department of Chemistry, Government Model Science College, Jabalpur (M.P), India

Received 10 December 2007; accepted in revised form 3 February 2008

**Abstract.** In the present study polyacrylamide (PAm)-gelatin-hydroxyapatite (HA) composites have been synthesized by suspension polymerization method. The prepared composites were characterized by Fourier transform spectroscopy (FTIR) which revealed the presence of functional groups in the composite. The X-ray diffraction (XRD) studies indicated that HA powder was present in nano size. Thermogravimetric analysis (TGA) revealed that composite is more thermally stable than the polymer matrix alone. The morphology of composite studied by optical microscopy (OPM) and scanning electron microscopy (SEM) suggested that pore size was between 3–20  $\mu\text{m}$ . The composites showed adequately good mechanical properties as evident from the varying compressive strength and modulus in the range  $31.57 \pm 8.16$  MPa and  $745 \pm 388$  MPa, respectively. The water sorption behavior was found to be dependent on the chemical composition of the matrix and the sorption data were used to calculate network parameters. The porosity of composite varied between 4 to 30.66%. The *in vitro* blood compatibility indicated that the adsorption of bovine serum albumin (BSA) varied from 0.11 to 0.24  $\text{mg} \cdot \text{g}^{-1}$ , the percentage haemolysis was between 2.4 to 6.9% and the weight of blood clot formed on the composite surfaces were found in the range 11 to 52 mg.

**Keywords:** polymer composites, hydroxyapatite, polyacrylamide, gelatin, blood compatibility

## 1. Introduction

Bone is a natural composite in the body, bone serves a number of functions, such as providing the cells found in the marrow that differentiate into blood cells, and also acting as a calcium reservoir. Nevertheless, its primary purpose is to provide mechanical support for soft tissues and serves as an anchor for the muscles that generate motion [1]. The incidence of fractures increases rapidly with age. This is partly due to extraosseous factors such as the impaired reflex of the elderly, their reduced proprioceptive efficiency, reduced cushioning by fat, weakened musculature and by osseous factors such as the structural changes in the shape and size of the bone and by deterioration of the condition of the bone material itself [2].

Bone graft materials are quickly becoming a vital tool in reconstructive orthopedic surgery and demonstrate considerable variability in their appearance. Functions of bone graft materials and bone healing provide a structural substrate for these processes, and serve as a vehicle for direct antibiotic delivery. The three primary types of bone graft materials are allografts, autografts, and synthetic bone grafts substitutes [3]. During the last 5 years bone cement materials have grown in popularity and are very promising osteoconductive substitutes for bone graft, they are prepared like acrylic cements.

Hydroxyapatite (HA), which has molecular stoichiometric formula  $\text{Ca}_{10}(\text{PO}_4)_6(\text{OH})_2$ , has been extensively investigated due to its excellent bio-

\*Corresponding author, e-mail: [akbmrl@yahoo.co.in](mailto:akbmrl@yahoo.co.in)  
© BME-PT and GTE

compatibility, bioactivity and osteoconductivity as well as its similarities to the main mineral component of bone. However, the poor compressive strength and fatigue failure limits its applicability to the low or non load-bearing sites in human body [4, 5]. Additionally, it has been reported that HA in the form of powders, used for the treatment of bone defects, has problem associated with migration to places other than implanted areas. It is known that various biocomposites existing in nature, such as shells and pearls, are all organic/inorganic composites with good mechanical properties, which may provide a route to resolve the above problems. Extensive research has been carried out in this regard and composite materials based on HA and a variety of polymers have been worked out [6]. Among them, hydroxyapatite is frequently used in orthopedic, dental and maxillofacial applications, meaning that it supports bone growth and osteointegration [7–9]. The development of bonelike composites with enhanced biocompatibility calls for a biomimetic approach using natural bone as a guide. Natural bone is a composite of collagen, a protein-based hydrogel template, and carbonated apatite crystals with varying compositions and microstructures. The unusual combination of a hard inorganic material and an underlying elastic hydrogel network gives bone, unique mechanical properties, such as low stiffness, resistance to tensile and compressive forces, and high fracture toughness [10]. Gelatin is a natural biopolymer obtained as a hydrolysis product of collagen, which is a fibrous protein, found abundantly in the animal kingdom in the form of hides, skins, bones and connective tissues. This natural water-soluble biopolymer has to its credit a large number of applications in pharmaceuticals, medicine, food and other allied fields [11]. However the hydrogels based on Polyacrylamide (PAm) have been widely used in drug release system, membranes for dialysis, oxidation devices, fixation of chemical enzymes etc. [12, 13]. Authors are interested in a ‘bottom-up’ approach to the design and synthesis of artificial bone. This entails the design of simple model system with well-designed chemical, physical, and biological properties, followed by an iterative increase in complexity of the system to realize a higher – order approximation of natural bone. In the present study crosslinked PAm-gelatin-HA composites have been synthesized using sedimentation approach.

Furthermore structural characterization, blood compatibility tests were also carried out. These results provide a framework for generating synthetic composites with defined organic/inorganic interfaces similar to natural bone.

## 2. Materials and methods

Calcium hydroxide  $\text{Ca}(\text{OH})_2$  was purchased from E. Merck and used as received. Ortho-phosphoric acid ( $-\text{H}_3\text{PO}_4$ , 88–93%), was purchased from Qaligens Fine Chemicals. Acrylamide (E. Merck, India) was freed from inhibitor after recrystallizing it twice from methanol and drying over anhydrous silica for a week. Gelatin purified was received from E. Merck, India. MBA (N,N-methylene bis-Acrylamide) were purchased from central drug house Mumbai (India). KPS (Potassium persulphate), obtained from Loba chemicals India, was employed as a polymerization initiator.

### 2.1. Synthesis of HA

HA was synthesized by the slow addition of 0.6 M  $\text{H}_3\text{PO}_4$  to an aqueous suspension of 1.0 M  $\text{Ca}(\text{OH})_2$  under constant heating at  $150^\circ\text{C}$  in  $\text{N}_2$  atmosphere as per the method reported in literature [14]. In order to obtain uniform size crystals of HA the pH of the reaction mixture was strictly controlled i.e. during addition of solutions the pH was maintained in the range of 11–12 while after washing off the powder the pH was below 9.

### 2.2. Preparation of PAm-gelatin-HA composites

PAm-gelatin-HA composites were prepared by free radical polymerization of acrylamide in the immediate presence of a crosslinker (MBA) and HA taken in pre-calculated amounts. In a typical experiment, 0.5 g of gelatin was dissolved into 15 ml of distilled water followed by the addition of 28.13 mM of Am, 3.0 g of HAp, 0.129 mM of MBA and 0.073 mM of KPS as free radical initiator. The whole reaction mixture was homogenized by manual mixing and poured into rectangular glass moulds of definite size (25 mm × 25 mm × 10 mm). The mould containing the reaction mixture was kept at  $70^\circ\text{C}$  for 4 h, then the upper polymer layer was separated from the lower slab which



was a white solid composite of PAm, gelatin and HA. The composite was then purified by immersing it in distilled water so as to allow the composite to swell till equilibrium. In this way the unreacted monomer and other reagents were leached out from the composite thus purifying the prepared PAm-gelatin-HA composite. The swollen soft composite was cut into desired shape, dried at 70°C for 24 h and then kept in air-tight containers.

## 2.3. Characterization

### 2.3.1. FTIR-studies

IR studies of the powdered specimens were recorded on a FTIR-8400S, Shimadzu spectrophotometer. Prior to analysis KBr pellets were prepared by mixing 1:10 of sample: KBr (wt/wt) followed by uniaxial pressing the powders under vacuum. Spectra were obtained between 4400–450  $\text{cm}^{-1}$  at 2  $\text{cm}^{-1}$  resolution.

### 2.3.2. XRD-studies

The XRD apparatus (Philips PW 1820) powder diffractometer, was used to investigate the crystallinity and phase content of PAm-gelatin-HA composites. The diffraction data were collected from 2 to 60°,  $2\theta$  values with a step size of 0.02° and counting time of 2 s/step<sup>-1</sup> at  $\lambda$  i.e. 1.54 Å.

### 2.3.3. TGA

To evaluate thermal stability of the PAm-gelatin-HA composites, TGA was performed on METTLER TA 3000 instrument in the temperature range of 50–800°C, in nitrogen atmosphere at a heating rate of 10°C·min<sup>-1</sup>. The sample weights were in the range of 15–20 mg.

### 2.3.4. Microscopy study

An approximate idea of the morphology of composites was deduced by using Optical microscope, MIOTIC DIGITAL MICROSCOPE DMWB-series. In order to study the morphology of the prepared composites SEM was carried out on STEREO SCAN, 430, Lecica SEM, USA.

### 2.3.5. Mechanical testing

Compression tests (dry test) were performed using an Universal Testing Machine (Instron series IX) possessing a load cell of 5 kN, at room temperature. The gauge length and diameter of all specimens were 6 mm and 2 mm respectively. Tests were conducted with a constant strain rate of 1 mm·min<sup>-1</sup>, and up to failure or until 60% reduction in specimen height. The modulus ( $E$ ) was determined by linear regression from the slopes in the initial elastic portion of the stress-strain diagram. A minimum number of 10 specimens were tested, and then  $E$  was averaged from the 5 measurements.

### 2.3.6. Swelling studies

The extent of swelling was determined by a conventional gravimetric procedure as reported in literature [15]. In a typical experiment, preweighed pieces of PAm-gelatin-HA composites were allowed to swell in distilled water for a predetermined time period (up to equilibrium swelling), thereafter the pieces were taken out from the water and gently pressed in-between the two filter papers to remove excess of water and finally weighed using a sensitive balance. The swelling ratio was determined by the Equation (1):

$$\text{Swelling ratio } (S_r) = \frac{\text{weight of swollen gel}}{\text{weight of dry gel}} = \frac{(S_w)}{(S_d)} \quad (1)$$

### 2.3.7. Porosity determination

The apparent porosity of a porous scaffold can influence its mechanical strength, permeability, and presence of structural defects [16]. The porosity was determined by the method reported in literature [17]. In brief, the known volume and weight of the samples noted as  $V_0$  and  $W_0$  respectively. After that samples were immersed into the dehydrated alcohol for 48 h till absorbing dehydrated alcohol saturated the samples. The weight gained by the sample is measured as  $W_1$ . Finally the porosity ( $P$ ) of the open pores in the composites were evaluated using formula given in Equation (2):

$$P = \frac{W_1 - W_0}{\rho V_0} \quad (2)$$

where  $\rho$  is the density of the dehydrated alcohol.

### 2.3.8. Blood compatibility

A biomaterial is a substance used in medical devices for contact with the living body for the intended method of application and for the intended time period. To acquire biocompatibility, the materials used in medical applications must meet certain regulatory requirements. The surface of biomaterials is believed to play an important role in determining biocompatibility. For materials that come into contact with blood, the formation of clot is the most undesirable but frequently occurring event that restricts the clinical acceptance of a material to be used as biomaterial. Therefore, certain test procedures have been developed and they need to be employed to judge the haemofriendly nature of materials.

#### 2.3.8.1. Clot formation tests

The anti-thrombogenic potential of the composite surface was judged by the blood-clot formation test, as described elsewhere [18]. In brief, the specimens were equilibrated with saline water (0.9% w/v NaCl) at 37°C for 24 h in a constant temperature bath. To these swollen samples was added 0.5 ml of ACD blood followed by the addition of 0.03 ml of  $\text{CaCl}_2$  solution ( $4 \text{ mol} \cdot \text{l}^{-1}$ ) to start the thrombus formation. Adding 4.0 ml of deionized water stopped the reaction and the thrombus formed was separated by soaking in water for 10 min at room temperature and then fixed in 36% formaldehyde solution (2.0 ml) for another 10 min. The fixed clot was placed in water for 10 min and after drying its weight was recorded. The same procedure was repeated for glass surface, blood bags and for the composites of varying compositions and respective weights of thrombus formed was recorded.

#### 2.3.8.2. % Haemolysis tests

Haemolysis experiments were performed on the surfaces of prepared PAm-gelatin-HA composites as described elsewhere [19]. In a typical experiment, dry composite pieces ( $4 \text{ cm}^2$ ) were equilibrated in normal saline water (0.9% w/v NaCl) at 37°C for 24 h and human ACD blood (0.25 ml) was added into the composites after 20 min 2.0 ml of

saline water was added into the specimens to stop haemolysis and the samples were incubated for 60 min at 37°C. Positive and negative controls were obtained by adding 0.25 ml of human ACD (acid citrate dextrose) blood and 0.9% NaCl respectively to 2.0 ml of doubly distilled water. Incubated samples were centrifuged for 45 min, the supernatant was taken and its absorbance at 545 nm was recorded using a spectrophotometer. The percentage of haemolysis was calculated using the following relationship, given in Equation (3):

$$\text{Haemolysis [\%]} = \frac{A_{\text{test-sample}} - A_{(-)\text{control}}}{A_{(+)\text{control}} - A_{(-)\text{control}}} \quad (3)$$

where  $A$  is absorbance. The absorbance of positive and negative controls was found to be 1.73 and 0.048, respectively.

#### 2.3.8.3. Protein (BSA) adsorption

Adsorption of BSA onto the composite materials was performed by the batch contact process reported elsewhere [20]. For protein adsorption experiment, protein (BSA) solutions were prepared in 0.5 M PBS (Phosphate buffer saline) at physiological pH 7.4. A fresh solution of BSA was always prepared prior to adsorption experiments. The composite of definite weights were equilibrated with PBS for 24 h. The adsorption was then carried out by gently shaking a BSA solution of known concentration containing preweighed and fully swollen composites. By taking fully swollen samples, the possibility of soaking of BSA solution within the composite becomes minimum. Shaking was performed so gently that no froth was produced, otherwise BSA would adsorb in air-water interface. After a definite time period, the samples were removed and the adsorbed protein was assayed for the remaining concentration of BSA by recording the absorbance at of protein solution at 272 nm on a UV spectrophotometer (Systronics, model no. 2201, India).

#### 2.3.8.4. Platelet adhesion test

A piece of composite of definite composition was incubated in platelet rich plasma (PRP) at 37°C for 6 min. The blood was obtained from a healthy donor and PRP was separated by automated aphaere-

sis. After incubation, the material was fixed in 2.5% glutaraldehyde aqueous solution for 10 min and kept in a 70% ethanol solution in order to avoid dehumidification and microorganism proliferation. The amount and morphology of adhered platelets were analyzed by SEM [21].

### 3. Results and discussion

#### 3.1. FTIR-studies

The FTIR spectra of native HA sintered at 70°C is shown in Figure 1a which clearly shows peaks at 602, 962, 1035  $\text{cm}^{-1}$ , corresponding to  $\text{PO}_4^{3-}$  ion [22] and a small and sharp band observed at 3572  $\text{cm}^{-1}$ , corresponds to the stretching mode of  $-\text{OH}$  group, which is characteristic of hydrated calcium phosphate such as HA [23]. A weak peak observed at 876  $\text{cm}^{-1}$  and strong peak at 1450  $\text{cm}^{-1}$  corresponds to the stretching vibration of  $\text{CO}_3^{2-}$  ions. These observations confirm that HA crystals were prepared, partially substituted by  $-\text{CO}_3^{2-}$  groups. Therefore, HA crystals are  $\text{CO}_3^{2-}$  containing HA [24]. Also the broad bands at about 3200 and 2800  $\text{cm}^{-1}$ , correspond to the absorbed hydrate and the sharp medium and short peaks between 3570–3670  $\text{cm}^{-1}$  belong to the stretching vibrations of lattice  $\text{OH}^-$  ions of hydroxyapatite [25]. It has

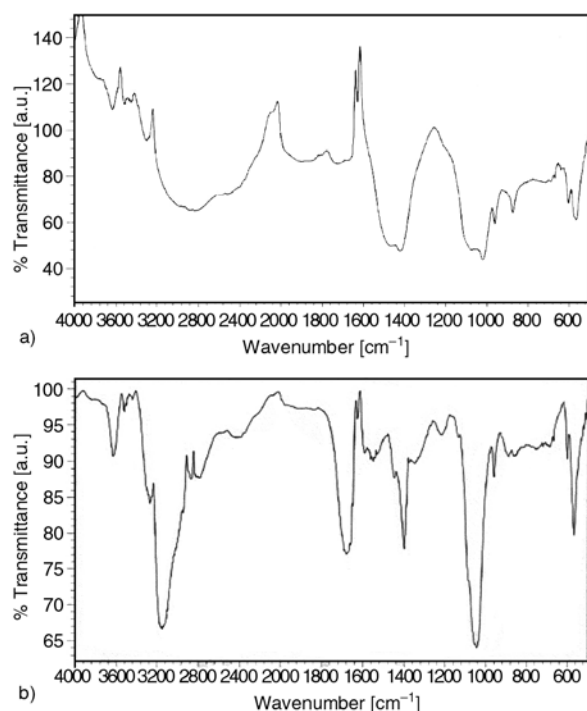


**Figure 1.** (a) FTIR spectra of native HA sintered at 70°C for 24 h; (b) FTIR spectra of PAm-gelatin-HA composite

been reported that the FTIR spectra of PAm where peaks at about 3298, 3184 and 1660  $\text{cm}^{-1}$  showed the presence of primary amide ( $-\text{NH}$  stretching vibration) group and peaks near about 1595 and 1429  $\text{cm}^{-1}$  corresponding to  $\text{C}=\text{O}$  asymmetric stretching vibration [26]. Gelatin being a protein, has been reported to contain the characteristic amide absorption bands at about 1690 and 1530  $\text{cm}^{-1}$  [27]. The FTIR spectra of PAm-gelatin-HA composite is shown in Figure 1b, which contains all the characteristic absorption peaks of HA, PAm and gelatin. As there are no considerable shifts of peaks of any group in the composite spectrum, it is confirmed that PAm-gelatin-HA composite is only a mixture and no chemical reaction has taken place between the individual components.

#### 3.2. XRD studies

The XRD pattern of the synthesized native HA is shown in Figure 2a which exhibits sharp apatite

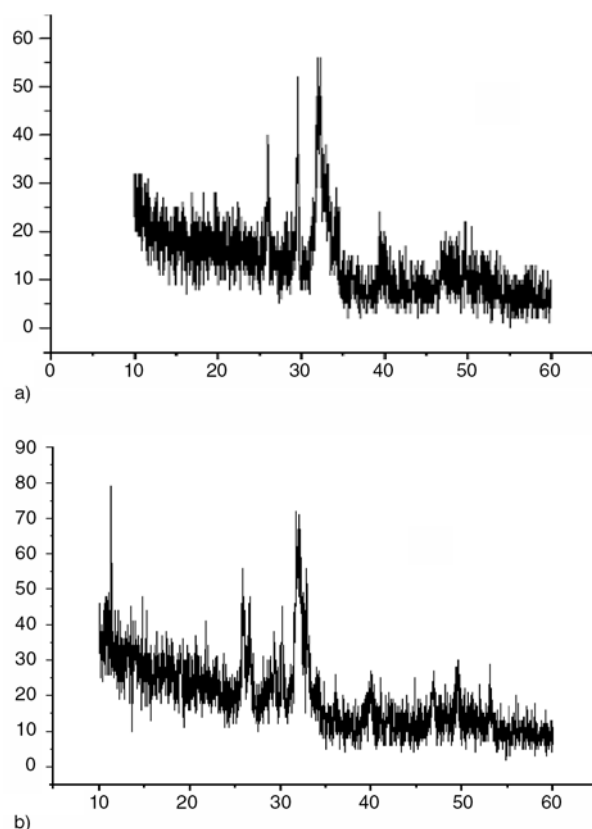


**Figure 2.** (a) XRD pattern of native HA sintered at 70°C for 24 h; (b) XRD pattern of native PAm-gelatin-HA composite with given composition, [AM] = 28.13 mM, [gelatin] = 0.5 g, [HAp] = 3.0 g, [MBA] = 0.129 mM

peaks due to crystal growth alternatively calcium carbonate peak at  $2\theta$  value of about  $29^\circ$  present together with apatite phase. However, the  $\beta$ -tricalcium phosphate ( $\beta$ - $\text{Ca}_3\text{P}_2\text{O}_7$ ) phase was not detected at any temperature. Also, the CaO peaks at  $37.469$  and  $54.029^\circ$  were not detected. The accompanying two peaks at about  $32.22$  and  $32.23^\circ$  of equal intensities were also detected which clearly confirm the presence of well crystallized HA phase [28]. The mean grain size was calculated using Debye-Scherrer formula [29, 30] as shown in Equation (4):

$$d = \frac{k\lambda}{\beta \cos \theta} \quad (4)$$

where  $d$  is mean grain size,  $k$  is the shape factor (0.9),  $\beta$  is broadening of the diffraction angle and  $\lambda$  is diffraction wavelength ( $1.54 \text{ \AA}$ ). The estimated average grain size of HA was found to be  $6.53 \text{ nm}$  and the width was found to be  $1.278 \text{ nm}$ . Figure 2b shows the XRD spectra of PAm-gelatin-HA composite with slight broadening of the apatite peaks showing the decrease in crystallinity of HA because of incorporation of polymer. The spectrum also shows a XRD peak at about  $31.99^\circ$  ( $2\theta$ ) indicating well crystalline nature of hydroxyapatite even in composite state.

### 3.3. TGA analysis

In order to evaluate thermal stability and understand the phase transformation in the prepared samples, the TGA studies were performed in the range  $50$  to  $800^\circ\text{C}$  and the results are shown in Figure 3. It is clear from the thermogram of native HA (Figure 3a) that the weight of the sample decreases quickly with increasing temperature and about total  $66\%$  weight loss is observed. The obtained weight loss is possibly due to evaporation of water. The obtained TGA results were further confirmed by a simple experiment that involved heating the composite of known initial weight in an oven in the temperature range  $50$  to  $800^\circ\text{C}$ . After heating was over the weight of composite was recorded and a weight loss of about  $66\%$  was noticed. It is revealed by the data that the weight loss that occurred at about  $580$  and  $620^\circ\text{C}$  could be attributed to the decomposition of trace  $\text{CO}_3^{2-}$  ions [31]. The exothermic dissociation of  $\text{CO}_3^{2-}$  is reported to occur at the temperature range between  $500$  to

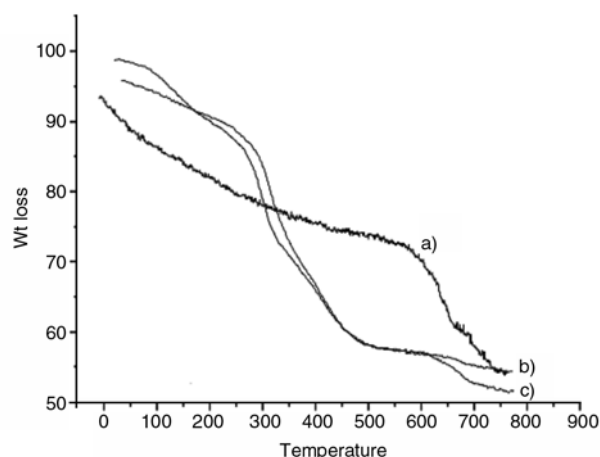


**Figure 3.** (a) TGA curve of native HA; (b) TGA curve of PAm-gelatin-HA composite with given composition  $[\text{Am}] = 28.13$ ,  $[\text{gelatin}] = 0.5 \text{ g mM}$ ,  $[\text{HAp}] = 3.0 \text{ g}$ ,  $[\text{MBA}] = 0.129 \text{ mM}$ ; (c) TGA curve of natural compact bone

$890^\circ\text{C}$  in nitrogen atmosphere. Figure 3b corresponds to the thermogram of PAm-gelatin-HA composite where initial weight loss from  $50$  to  $200^\circ\text{C}$  may be due to the evaporation of surface adsorbed water molecules and the quick weight loss from about  $300$  to  $600^\circ\text{C}$  may be due to the endothermic dissociation of  $\text{CO}_3^{2-}$  ions [32]. Furthermore, the TGA of natural compact bone shown in Figure 3c, may also be compared with that of prepared composite and a fair resemblance may be noticed.

### 3.4. Microscopy study

In order to study the morphology of the prepared composites and adhesion of platelets OPM study has been performed as shown in Figure 4a and 4b, respectively. The comparison of both the images indicates a change in surface of the composite material after the addition of platelets.

Since the morphology of a biomaterial contributes significantly to its biocompatibility and considering this important aspect, the morphology of the surface has been examined by recording SEM of the PAm-gelatin-HA composite. The SEM images of the composites are shown in Figure 5, which clearly shows that the composite surface is highly porous in nature. The size of the pores varies in the range  $3$  to  $20 \mu\text{m}$  as indicated by arrows in the same figure.



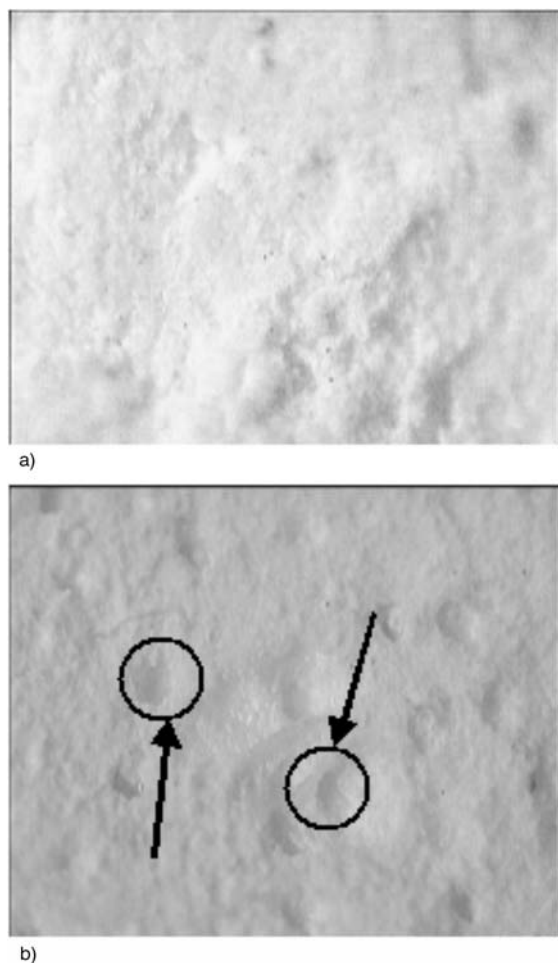


**Figure 4.** Optical micrographs of PAm-gelatin-HA composite. (a) composite without platelet; (b) composite with platelet (indicated with arrows)

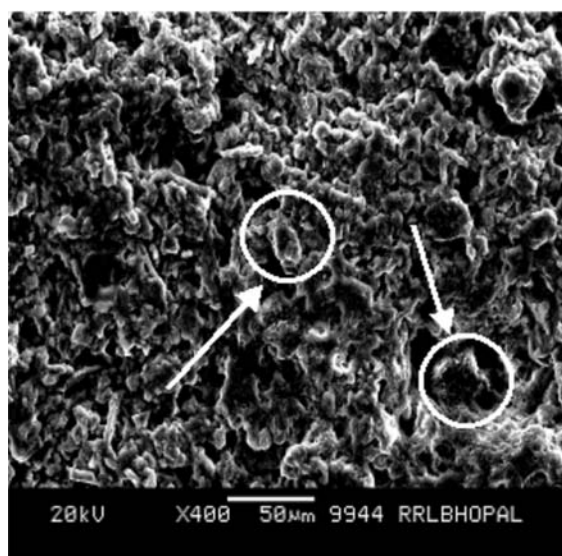


**Figure 5.** SEM micrographs of PAm-gelatin-HA composite, pores have been indicated with arrows

### 3.5. Mechanical testing

To examine the mechanical properties of the PAm-gelatin-HA composites (having composition [Am] = 28.13, [gelatin] = 0.5 g mM, [HAp] = 4.0 g, [MBA] = 0.129 mM) compression tests of the specimens were conducted, in dry condition. The modulus ( $E$ ) was found to be  $745 \pm 388$  MPa for the control set of composites and compressive strength was found to be  $31.57 \pm 8.16$  MPa. The enhanced modulus provides increased fracture toughness to the samples. These results show that PAm-gelatin-HA composites possess quite good mechanical properties for being used in tissue engineering (TE). The values show good agreement with those obtained for normal human articular cartilage, which has been reported to have a compressive strength ranging from 1.9 to 14.4 MPa [33, 34]. The compressive strength and Young's modulus of trabecular bone were reported ranging between 2–10 MPa and 50–100 MPa, respectively [35, 36].

### 3.6. Swelling behavior of composite

One of the prime factors to contribute to biocompatible nature of synthetic biomaterials is the amount of water content which imparts several unique physiochemical properties to the material. A polymer matrix imbibing an adequate of water, shows living tissue like membrane, physiological stability, low interfacial tension, permeability to biomolecules etc. Thus realizing the unusual significance of water sorption capacity of a material, the PAm-gelatin-HAp composites have been investigated for water sorption capacity and the influence of chemical composition of the composites on their water intake has been investigated as discussed below.

#### 3.6.1. Effect of Am

The influence of Am content of the composite on its swelling behavior has been studied by varying its concentration in the range 14.06 to 56.27 mM. The observed results are shown in Figure 6a which clearly indicate that the swelling ratio constantly increases with increasing amount of PAm. The observed results are quite expected as PAm is a highly hydrated polymer and its increasing content in the composite makes it more hydrophilic in

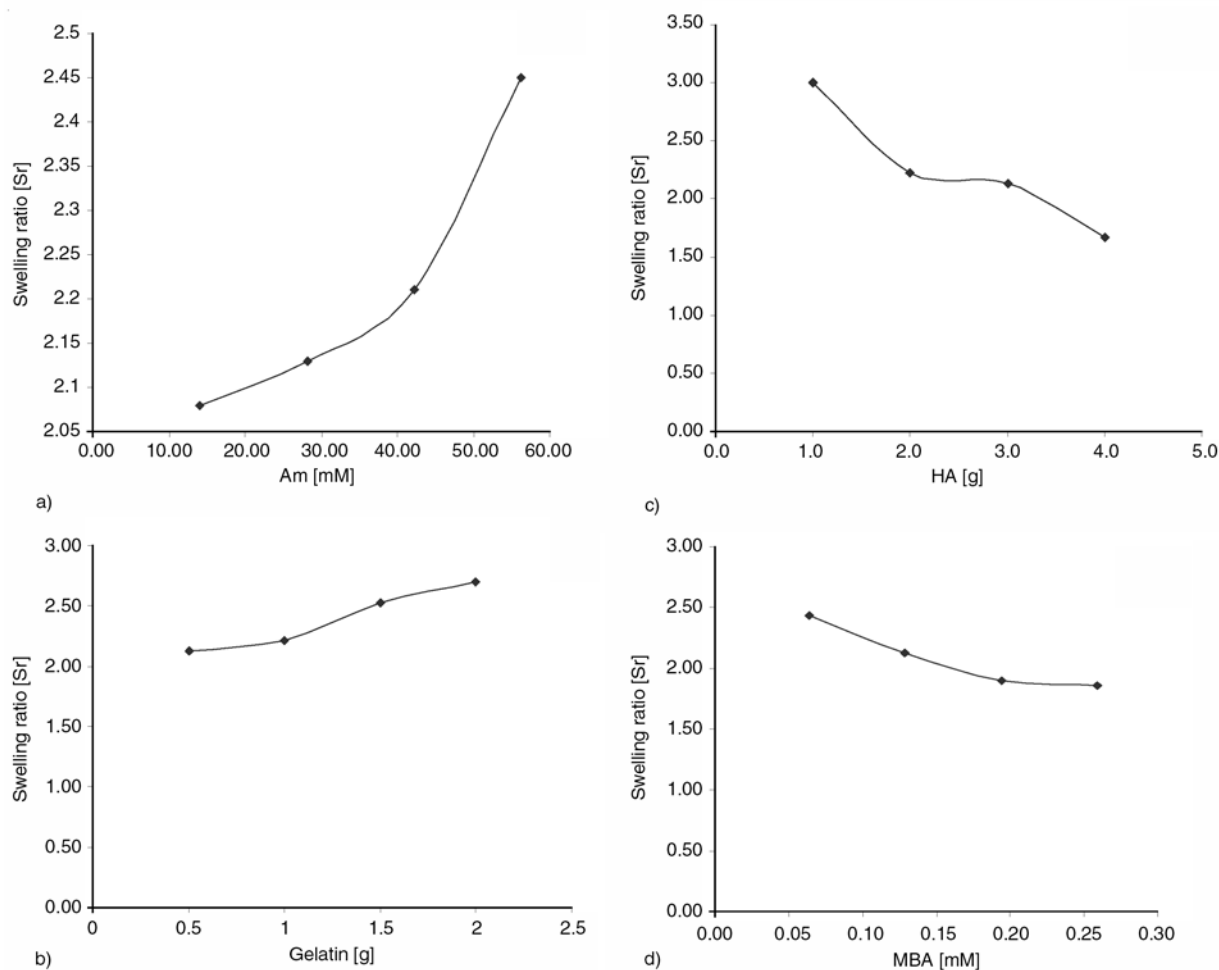


**Figure 6.** (a) Variation of swelling ratio with varying amounts of Am i.e. 14.06 to 56.27 mM; (b) variation of swelling ratio with varying amounts of gelatin i.e. 0.5 to 2.0 g; (c) variation of swelling ratio with varying amounts of HA i.e. 1.0 to 4.0 g; (d) variation of swelling ratio with varying amounts of MBA i.e. 0.064 to 0.259 mM

nature which eventually results in an enhanced swelling.

### 3.6.2. Effect of gelatin

The effect of gelatin on the swelling ratio of the hydrogel was investigated by varying the concentration of gelatin in the range 0.5 to 2.0 g in the feed mixture of the composite. The results are shown in Figure 6b which clearly reveal that the swelling ratio constantly increases with increasing concentration of gelatin up to 2.0 g. It is to be mentioned here that beyond this concentration the feeding mixture becomes too viscous to form the composite. The observed results may be explained by the fact that, since gelatin itself has a natural tendency to form reversible gel, its increasing pressure in PAm-gelatin-HAp mixture lowers the weight fractions of HA and PAm in the feed mixture. In this way a lower degree of crystallinity results in an

enhanced swelling. Gelatin is a hydrophilic polymer and its increasing concentration in the feed mixture increases water sorption capacity of composite.

### 3.6.3. Effect of hydroxyapatite

Impregnation of hydroxyapatite into the polymer matrix brings about a significant change in water sorption behavior and mechanical properties of the matrix. In order to obtain the effect of HA on the swelling ratio of the composite, the concentration of the HA was varied in the range 1.0 to 4.0 g in the feed mixture. The results are shown in Figure 6c, which clearly reveal that the swelling ratio constantly decreases with increasing HA content in the composite. The results are quite expected and may be explained by the fact that due to relatively lower hydrophilicity of the apatite in comparison to PAm-gelatin matrix, its increasing fraction in the com-

posite results in a lower water sorption by the composite. Alternatively, the increasing polymer-HA interaction with increasing concentration of HA results in a slower relaxation of polymer chains, which also decreases the swelling ratio.

### 3.6.4. Effect of crosslinker

One of the effective ways to modify the water sorption behavior of a polymer matrix is to employ varying amounts of crosslinking agent at the time of polymerization reaction. The addition of a crosslinker not only enhances the degree of crosslinking but also increases the glass transition temperature ( $T_g$ ) of the polymer. In the present study the effect of crosslinker content of the composite on its swelling ratio has been studied by varying its concentration in the range of 0.064 to 0.259 mM. The results are shown in Figure 6d reveal the fact that with the increasing content of MBA in the feeding mixture the crosslink density of the network increases [37] which results in higher crosslink density of the network. This obviously slows down the diffusion of water molecules into the composite and eventually results in a fall in water intake [38].

### 3.7. Network parameters

One of the most important structural parameters characterizing a crosslinked density is the average molecular mass between crosslinks ( $M_c$ ), which is directly related to the crosslink density. The magnitude of  $M_c$  significantly affects the physical and mechanical properties of crosslinked polymers, and its determination has great practical significance. Equilibrium swelling is widely used to determine

$M_c$ . Early research by Flory and Rehner laid the foundation for the analysis of equilibrium swelling. According to the theory of Flory and Rehner, for a perfect network (Equation (5)):

$$M_c = -v_1 d_p \frac{V_s^{1/3} - \frac{V_s}{2}}{\ln(1 - V_s) + V_s + \chi V_s^2} \quad (5)$$

where in Equation (5)  $M_c$  is the number average molar mass of the chain between crosslinks,  $v_1$  is the molar volume [ $\text{ml} \cdot \text{mol}^{-1}$ ],  $d_p$  is the polymer density [ $\text{g} \cdot \text{ml}^{-1}$ ],  $V_s$  is the volume fraction of polymer in the swollen gel and  $\chi$  is the Flory and Huggins interaction parameter between solvent and polymer. The swelling ratio is equal to  $1/V_s$ . Here the crosslink density  $q$  is defined as the mole fraction of crosslinked units, as shown by Equation (6):

$$q = \frac{M_0}{M_c} \quad (6)$$

where  $M_0$  is the molar mass of the repeating unit. Some authors defined a crosslink density,  $V_e$ , as the number of elastically effective chains totally included in a perfect network per unit volume, simply related to  $q$  since, as given by Equation (7),

$$V_e = d_p \frac{N_A}{M_c} \quad (7)$$

where  $N_A$  is Avogadro's number. The density of polymer  $d_p$  was determined to be  $0.65 \text{ g} \cdot \text{cm}^{-3}$ . Other parameters such as  $v_1$  and  $\chi$  were taken from the literature. Using Equations (5)–(7) the values of  $M_c$ ,  $q$ , and  $V_e$  have been calculated for the varying compositions of PAm-gelatin-HA composites [39]. The values are summarized in Table 1.

**Table 1.** Data showing the structural parameters of PAm-gelatin-HA composites of varying compositions

MBA (crosslinker) [mM]	Am [mM]	Gelatin [g]	HAp [g]	Swelling ratio	$M_c$	$q \cdot 10^2$	$V_e \cdot 10^{-20}$
0.064	28.13	0.5	3.0	2.43	189.40	37.52	2.38
0.129	28.13	0.5	3.0	2.13	83.90	84.71	5.38
0.259	28.13	0.5	3.0	1.86	55.14	128.00	8.17
0.129	14.06	0.5	3.0	2.08	730.00	9.73	6.17
0.129	28.13	0.5	3.0	2.13	83.90	84.71	5.38
0.129	56.27	0.5	3.0	2.45	200.00	35.54	2.25
0.129	28.13	0.5	3.0	2.13	83.90	84.71	5.38
0.129	28.13	1.0	3.0	2.21	123.00	57.78	3.66
0.129	28.13	2.0	3.0	2.70	47.05	151.07	9.58
0.129	28.13	0.5	1.0	3.00	394.40	20.34	1.29
0.129	28.13	0.5	2.0	2.22	142.00	50.05	3.17
0.129	28.13	0.5	4.0	1.67	51.77	137.29	8.71

### 3.8. Percent porosity

Porosity characterization is based on the presence of open pores, which are related to properties such as permeability, and surface area of the porous structure. The measured porosity of the PAm-gelatin-HA composites is given in Table 2, which reveals the fact that as the amount of crosslinker is increased in feed mixture porosity becomes low, the results are quite obvious since increased number of crosslinks make polymer network more compact which results in the lower mesh size and decreased porosity. It was found that the addition of HA results in more dense and thicker pore walls with lower porosity [40] as shown in Table 2. However the decrease in porosity observed as the amount of polymer like PAm is increased in feed mixture is mainly due to the increase in the HAP/polymer ratio in the dispersed phase which in turns improves the sintering and porosity reduction [41]. As we increase the amount of gelatin in feed

mixture porosity increases, this may be explained on the basis of the fact that gelatin is a hydrophilic polymer and during the formation of matrix it lets the polymer network to swell in greater amount, which in turns results in greater pore size within the network and after the drying of the matrix, it yields greater porosity.

### 3.9. Blood compatibility

Blood compatibility of a material is intimately related to various intrinsic factors such as organization of water molecules in the polymer matrix, chemical architecture and topology of the surface etc. In the present study also various *in vitro* tests were applied to observe the blood compatibility of the prepared PAm-gelatin-HA composite. The results are shown in Table 3, which may be discussed as below:

**Table 2.** Data showing the percent porosity of PAm-gelatin-HA composites of different compositions

S. No	(MBA) [mM]	Am [mM]	HAp [g]	Gelatin [g]	% Porosity
1.	0.064	28.13	3.0	0.5	13.00
2.	0.129	28.13	3.0	0.5	11.29
3.	0.259	28.13	3.0	0.5	4.00
4.	0.129	14.06	3.0	0.5	30.66
5.	0.129	28.13	3.0	0.5	11.29
6.	0.129	56.27	3.0	0.5	4.03
7.	0.129	28.13	1.0	0.5	11.29
8.	0.129	28.13	3.0	0.5	11.29
9.	0.129	28.13	4.0	0.5	5.60
10.	0.129	28.13	1.0	0.5	11.29
11.	0.129	28.13	3.0	1.0	15.18
12.	0.129	28.13	4.0	2.0	18.56

**Table 3.** Blood compatibility parameters of PAm-gelatin-HA composites of different compositions

(MBA) [mM]	Am [mM]	Hap [g]	Gelatin [g]	Swelling ratio	BSA adsorption [mg·g <sup>-1</sup> ]	Percentage haemolysis	Blood clot formation [mg]
0.064	28.13	3.0	0.5	2.43	0.021	2.4	11.0
0.129	28.13	3.0	0.5	2.13	0.020	3.4	32.0
0.259	28.13	3.0	0.5	1.86	0.023	6.9	52.0
0.129	14.06	3.0	0.5	2.08	0.022	4.5	49.0
0.129	28.13	3.0	0.5	2.13	0.020	3.4	32.0
0.129	56.27	3.0	0.5	2.45	0.018	2.0	21.0
0.129	28.13	1.0	0.5	3.00	0.018	2.9	25.0
0.129	28.13	3.0	0.5	2.13	0.020	3.4	32.0
0.129	28.13	4.0	0.5	1.67	0.024	3.7	43.0
0.129	28.13	1.0	0.5	2.13	0.020	4.2	32.0
0.129	28.13	3.0	1.0	2.21	0.015	5.0	29.0
0.129	28.13	4.0	2.0	2.70	0.011	3.4	23.0
Glass –surface						–	44.0
Polyethylene bag						30.4	35.0



When the concentration of crosslinker is raised in the range 0.064 to 0.259 mM, the amount of blood clot formed increases with increasing MBA content in the composite. The results summarized in Table 3 also reveal that both the percent haemolysis and protein adsorption also increase with increasing MBA content. The results obtained are consistent with each other and suggest that the composite shows decreasing blood compatibility with increasing number of crosslinks. The results may be explained by the fact that since MBA is a hydrophobic crosslinker, its increasing content results in greater protein-surface interaction and, therefore, shows more clot formation and percent haemolysis. The results reveal the fact that the weight of blood clot constantly decreases with increasing amount of PAm and gelatin in the feed mixture. The results may be explained on the basis of the fact that both PAm and gelatin are hydrophilic polymers and therefore, are not expected to provoke any damage to blood cells or any change in the structure of the plasma proteins. It has also been realized that with increasing concentrations of PAm and gelatin, the composite acquires more smoothness of their surfaces and this consequently results in an improvement in antithrombogenic property of material.

The prepared composites were tested for haemolytic activity and the results obtained are quite satisfactory. Percent haemolysis is maximum (100%) for a distilled water–water-added blood sample (positive control). The results obtained clearly indicate that, with increasing PAm and gelatin content, the extent of haemolysis steadily decreases. The observed results may be attributed to the reason that, with the increase in PAm and gelatin weight fractions in the composite, the surface composition favorably changes, which improves the blood – compatible quality of the material.

One of the essential components of the composite is HA and its concentration in the composite is expected to influence blood compatibility of the matrix. In order to examine this the concentration of HA powder was varied in the range 1.0 to 4.0 g and blood compatibility parameters were evaluated. The data summarized in Table 3 reveal that with increasing HA content, the blood compatibility of the composite shows a decrease, i.e. all the three parameters increase. The reason for the observed more thrombogenicity is that the ionic groups of HAp may react with the blood compo-

nents and produce greater blood-surface interactions. This is likely to cause thrombogenic behavior of the composite.

The above discussion clearly suggests that a less crosslinked composite with more PAm-gelatin and low HAp content may prove to be more biocompatible.

#### 4. Conclusions

Nanosized hydroxyapatite powder is obtained by the hydrothermal method and the free radical polymerization of acrylamide in presence of HA and gelatin forms a nanocomposite material. The HA-composites when examined by FTIR spectroscopy clearly show the presence of HA and polymer components in the composite. The XRD studies also confirm the nanosized mean grain size of the HA powder in native state as well as in composites. Thermal properties of the material assigned by TGA analysis, meet the thermal requirements of these types of materials. The optical microscopy and SEM studies reveal the morphological anisotropy of the material.

Swelling studies show the effect of composition on the swelling. It is found that as the PAm and gelatin contents increases, the swelling ratio also increases. The extent of swelling decreases with increasing amounts of HA and crosslinker.

The PAm-gelatin-HA composite also display a fair level of blood compatibility as confirmed by *in vitro* experiments of blood clot formation, protein adsorption and haemolysis. It is clear by the data, as we increase the amount of crosslinker in the feed mixture in the range 0.064–0.259 mM, the amount of clot formation increases. Similar type of results are observed when the amount of HA increases in the feed mixture of the composite. In case of polymers as the amounts of PAm and gelatin increase in composite mixture degree of blood clot formation decreases due to the increased swelling of composite. Percentage haemolysis tests for haemolytic activity of composites indicate that as the content of crosslinker and HA increases in feed mixture percent of haemolysis also increases. The observed results are consistent with blood clot formation test results and conclude that a material surface showing reluctance to BSA adsorption proves to be more biocompatible. BSA absorption results also show

the similar type of trends as those of percentage haemolysis and clot formation results.

## Acknowledgements

The authors gratefully acknowledge the authorities of BRNS (Board of Research in Nuclear Sciences), BARC (Bhabha Atomic Research Center) Mumbai, India, for providing financial assistance in the form of a project (Sanction no. 2005/35/26-BRNS/RTAC) and performing TGA, XRD and other analysis of prepared composite materials.

## References

- [1] Bajpai A. K., Singh R.: Study of biomineralization of poly(vinyl alcohol)-based scaffolds using an alternate soaking approach. *Polymer International*, **56**, 557–568 (2007).
- [2] Zioupos P.: Ageing human bone: Factors affecting its biomechanical properties and the role of collagen. *Journal of Biomaterials Applications*, **15**, 187–229 (2001).
- [3] Beaman F. D., Bancroft L. W., Peterson J. J., Krandorf M. J.: Bone graft materials and synthetic substitutes. *Radiologic Clinics of North America*, **44**, 451–461 (2006).
- [4] Pramanik S., Agrawal A. K., Rai K. N., Garg A.: Development of high strength hydroxyapatite by solid-state sintering process. *Ceramics International*, **33**, 419–426 (2007).
- [5] Chang M. C., Ko C.-C., Douglas W. H.: Preparation of hydroxyapatite-gelatin nanocomposite. *Journal of Biomaterials*, **24**, 2853–2862 (2003).
- [6] Li Z., Li Y., Yang A., Peng X., Wang X., Zang X.: Preparation and *in vitro* investigation of chitosan/nano-hydroxyapatite composite used as bone substitutes materials. *Journal of Materials Science: Materials in Medicine*, **16**, 213–219 (2004).
- [7] Damien C. J., Parsons J. R.: Bone graft and bone graft substitutes: A review of current technology and applications. *Journal of Applied Biomaterials*, **2**, 187–208 (1991).
- [8] Aoki H.: Science and medical applications of hydroxyapatite. Ishiyaku Euro America, St. Louis (1994).
- [9] Murugan R., Ramakrishna S.: Nanostructured biomaterials. in 'Encyclopedia of Nanoscience and Nanotechnology' (ed.: Nalwa H. S.) American Scientific Publishers, Stevenson Ranch, Vol 7, 595–613 (2004).
- [10] Song J., Malathong V., Bertozzi C. R.: Mineralization of synthetic polymer scaffolds: A bottom-up approach for the development of artificial bone. *Journal of the American Chemical Society*, **127**, 3366–3372 (2005).
- [11] Bajpai A. K.: Determination of solubility parameter of gelatin by swelling measurements. *Revue Roumaine de Chimie*, **41**, 219–222 (1996).
- [12] Bajpai A. K., Rajpoot M.: Release and diffusion of sulfamethoxazole through acrylamide-based hydrogel. *Journal of Applied Polymer Science*, **81**, 1238–1247 (2001).
- [13] Retama J. R., Lopez-Ruiz B., Lopez-Cabarcos E.: Microstructural modifications induced by the entrapped glucose oxidase in cross-linked polyacrylamide microgels used as glucose sensors. *Biomaterials*, **24**, 2965–2973 (2003).
- [14] Ishikawa T., Wakamura M., Kondo S.: Surface characterization of calcium hydroxylapatite by Fourier transform infrared spectroscopy. *Langmuir*, **5**, 140–144 (1989).
- [15] Bajpai A. K., Sainy R.: Preparation and characterization of novel biocompatible cryogels of poly (vinyl alcohol) and egg-albumin and their water sorption study. *Journal of Materials Science: Materials in Medicine*, **17**, 49–61 (2006).
- [16] Sepulveda P., Ortega F. S., Innocentini M. D. M., Pandolfelli V. C.: Properties of highly porous hydroxyapatite obtained by the gel casting of foams. *Journal of the American Ceramic Society*, **83**, 3021–3024 (2000).
- [17] Zhang Y., Zhang M.: Synthesis and characterization of macroporous chitosan/calcium phosphate composite scaffolds for tissue engineering. *Journal of Biomedical Materials Research*, **55**, 304–312 (2001).
- [18] Bajpai A., Sainy R.: Preparation and characterization of spongy cryogels of poly(vinyl alcohol)-casein system: Water sorption and blood compatibility study. *Polymer International*, **54**, 796–806 (2005).
- [19] Saini R., Bajpai A. K.: Preparation and characterization of biocompatible spongy cryogels of poly(vinyl alcohol)-gelatin and study of water sorption behavior. *Polymer International*, **54**, 1233–1242 (2005).
- [20] Bajpai A. K., Mishra D. D.: Adsorption of a blood protein on to hydrophilic sponges based on poly(2-hydroxyethyl methacrylate). *Journal of Materials Science: Materials in Medicine*, **15**, 583–592 (2004).
- [21] Bajpai A. K., Kankane S.: Preparation and characterization of macroporous poly(2-hydroxyethyl methacrylate) - based biomaterials: Water sorption property and *in vitro*-blood compatibility. *Journal of Applied Polymer Science*, **104**, 1559–1571 (2007).
- [22] Wang Y., Wang X., Wei K., Zhao N., Zhang S., Chen J.: Fabrication, characterization and long term *in vitro* release of hydrophilic drug using PHBV/HA composite microspheres. *Materials Letters*, **61**, 1071–1076 (2007).
- [23] Taş A. C.: Synthesis of biomimetic Ca-hydroxyapatite powders at 37°C in synthetic body fluids. *Biomaterials*, **21**, 1429–1438 (2000).
- [24] Zhang L. J., Feng X. S., Liu H. G., Qian D. J., Zhang L., Yu X. L., Cui F. Z.: Hydroxyapatite/collagen composite materials formation in stimulated body fluid environment. *Materials Letters*, **58**, 719–722 (2004).
- [25] Blakeslee K. C., Condrate R. A.: Vibration spectra of hydrothermal prepared hydroxyapatite. *Journal of the American Ceramic Society*, **54**, 559–563 (1971).

- [26] Pourjavadi A., Mahdavinia R. G.: Superabsorbency, pH-sensitivity and swelling kinetics of partially hydrolyzed chitosan-g-poly(acrylamide) hydrogels. *Turk Journal of Chemistry*, **30**, 595–608 (2006).
- [27] Saraswathy G., Pal S., Rose C., Sastry T. P.: A novel bio-inorganic bone implant containing deglude bone, chitosan and gelatin. *Bulletin of Materials Science*, **24**, 415–420 (2001).
- [28] Vijayalakshmi U., Rajeshwari S.: Preparation and characterization of microcrystalline hydroxyapatite using sol gel method. *Trends in Biomaterials and Artificial Organs*, **19**, 57–62 (2006).
- [29] Rahaman M. N.: *Ceramics processing and sintering*. Marcel Dekker, New York (1995).
- [30] Prabakaran K., Thamaraiselvi T. V., Rajeswari S.: Electrochemical evaluation of hydroxyapatite reinforced phosphoric acid treated 316L stainless steel. *Trends in Biomaterials and Artificial Organs*, **19**, 84–87 (2006).
- [31] Song Y., Wen S., Li M.: The investigation on preparation and physiochemical process of nanosized hydroxyapatite powder. *Material Research Society, Symposium Proceedings*, **724**, N7.15.1–N7.15.6 (2002).
- [32] Murugan R., Ramkrishna S., Panduranga Rao K.: Nanoporous hydroxy-carbonate apatite scaffold made of natural bone. *Materials Letters*, **60**, 2844–2847 (2006).
- [33] Gu Z. Q., Xiao J. M., Zhang X. H.: The development of artificial articular cartilage- PVA-hydrogel. *Bio-Medical Materials and Engineering*, **8**, 75–81 (1998).
- [34] Magnussen R. A., Guilak F., Vail T. P.: Cartilage degeneration in post-collapse cases of osteonecrosis of the human femoral head: Altered mechanical properties in tension, compression, and shear. *Journal of Orthopedic Research*, **23**, 576–583 (2005).
- [35] Taş A. C.: Preparation of porous bioceramics by a simple PVA- processing route. *Key Engineering Materials*, **264–268**, 2079–2082 (2004).
- [36] Yaszemski M. J., Payne R. G., Hayes W. C., Langer R., Mikos A. G.: Evolution of bone transplantation: Molecular, cellular and tissue strategies to engineer human bone. *Biomaterials*, **17**, 175–185 (1996).
- [37] Bajpai A. K., Bajpai J., Soni S. N.: Preparation and characterization of electrically conductive composites of poly(vinyl alcohol)–g–poly(acrylic acid) hydrogels impregnated with polyaniline (PANI). *Express Polymer Letters*, **2**, 26–39 (2008).
- [38] Bajpai A. K., Mishra A.: Preparation and characterization of tetracycline-loaded interpenetrating polymer network of carboxymethyl cellulose and poly(acrylic acid): Water sorption and drug release study. *Polymer International*, **54**, 1347–1356 (2005).
- [39] Bajpai A. K.: Blood protein adsorption onto macroporous semi-interpenetrating polymer networks (IPNs) of poly(ethylene glycol) (PEG) and poly(2-hydroxyethyl methacrylate) (PHEMA) and assessment of in vitro blood compatibility. *Polymer International*, **56**, 231–244 (2007).
- [40] Narbat M. K., Hashtjin M. S., Pazouki M.: Fabrication of porous hydroxyapatite-gelatin scaffolds crosslinked by glutaraldehyde for bone tissue engineering. *Iranian Journal of Biotechnology*, **4**, 54–60 (2006).
- [41] Pradeesh T. S., Sunny M. C., Varma H. K., Ramesh P.: Preparation of microstructured hydroxyapatite microspheres using oil in water emulsions. *Bulletin of Materials Science*, **28**, 383–390 (2005).

# Preparation and self-assembly behavior of polystyrene-block-poly (dimethylaminoethyl methacrylate) amphiphilic block copolymer using atom transfer radical polymerization

Y. J. Zhu<sup>1</sup>, Y. B. Tan<sup>1,2\*</sup>, X. Du<sup>1</sup>

<sup>1</sup>School of Chemistry and Chemical Engineering, Shandong University, Jinan 250100, People's Republic of China

<sup>2</sup>Key Laboratory of Colloid and Interface Chemistry (Shandong University), Ministry of Education, Jinan 250100, P. R. China

Received 15 November 2007; accepted in revised form 3 February 2008

**Abstract.** Asymmetric and semi-symmetric amphiphilic diblock copolymers polystyrene-*block*-poly (dimethylaminoethyl methacrylate) (PS-*b*-PDMAEMA) with the same PS block length of 62 repeat units and quite short (3 repeat units) or equivalent (47 repeat units) length of PDMAEMA have been prepared simply by varying the ratio of the bromine-terminated macroinitiator polystyrene (PS-Br) to DMAEMA using atom transfer radical polymerization (ATRP). The chemical structures and compositions of the PS-*b*-PDMAEMA block copolymers are studied by nuclear magnetic resonance (NMR) spectroscopy, gel permeation chromatography (GPC), and elementary analysis (EA). The self-assembly behaviors of copolymers in N,N-dimethyl formamide (DMF) with different pH and dioxane/water binary solvent mixture by direct dissolution method (DD), are studied by transmission electron microscopy (TEM), electron diffracting analysis (EDA), and energy-dispersive analysis of X-rays (EDAX) techniques. Transmission electron microscopy results suggest that asymmetric block copolymer PS<sub>62</sub>-*b*-PDMAEMA<sub>3</sub> (the numbers in the form of footnotes represent repeated units of each monomer in the copolymer) can form spherical core-shell micelles, large compound reverse micelles (LCRMs), hexagonal/rhombic phases, reverse hexagonal/rhombic phases, vesicles, reverse vesicles and necklace-like reverse micelles, controlled by common or selective solvent and pH, while most of the aggregates of semi-symmetric PS<sub>62</sub>-*b*-PDMAEMA<sub>47</sub> are simply spherical, such as spherical core-shell micelles and reverse spherical core-shell micelles, besides hexagonal/rhombic phases. All above structures are controlled by three components of the free energy of aggregation: core-chain stretching, interfacial energy and intercoronal chain interaction.

**Keywords:** smart polymers, amphiphilic block copolymer, self-assembly, polymer synthesis

## 1. Introduction

Unlike the completely hydrophobic or hydrophilic block copolymers, amphiphilic block copolymer, especially containing pH and temperature-responsive polycationic poly (dimethylaminoethyl methacrylate) (PDMAEMA) as the hydrophilic segment, namely, polymeric surfactants, can provide many significant benefits to diverse applica-

tions such as stabilizers, emulsifiers, or dispersants in industrial and pharmaceutical preparations [1–6]. They are also useful in colloid chemistry and self-assembly chemistry [7–9].

Amphiphilic block copolymers polystyrene-*block*-poly (dimethylaminoethyl methacrylate) (PS-*b*-PDMAEMA) have been synthesized via living anionic polymerization [10, 11]. Anionic polymer-

\*Corresponding author, e-mail: [ybtan@sdu.edu.cn](mailto:ybtan@sdu.edu.cn)  
© BME-PT and GTE



ization is an excellent and well-established method for controlling copolymer architecture and obtaining narrow molecular weight distributions. However, this method has drawbacks such as the necessary purity of the solvent and of the monomer, performance under high-vacuum and quite low reaction temperature. The recent development of living/controlled radical polymerizations such as Atom Transfer Radical Polymerization (ATRP) [12, 13], Reversible Addition Fragmentation chain Transfer polymerization (RAFT) [14] and Stable Free Radical Polymerization (SFRP) [4, 15], has opened a new route to synthesize functional and architectural block copolymers PS-*b*-PDMAEMA with well-defined structures. This paper reports the synthesis of two types of amphiphilic AB diblock copolymers of different lengths of PDMAEMA segment with narrow polydispersities by ATRP using well-defined bromine-terminated polystyrene (PS-Br) as macroinitiator, simply by varying the ratio of the macroinitiator to DMAEMA: one is asymmetric (95 mol% of PS) diblock copolymer PS<sub>62</sub>-*b*-PDMAEMA<sub>3</sub> (the numbers in the form of footnotes represent repeated units of each monomer in the copolymer) (Block 1), and the other is semi-symmetric (57 mol% of PS) PS<sub>62</sub>-*b*-PDMAEMA<sub>47</sub> (Block 2).

Amphiphilic block copolymer can not only be prepared by versatile synthetic approaches but also has multiple morphologies generated by its different chemical interactions between two blocks or environment. A vast array of structures by asymmetric amphiphilic block copolymers in solution has been identified and a detailed investigation of the thermodynamic and kinetic parameters that induce morphologies has been begun by Eisenberg's group [16–39]. Two methods for aggregate preparation, the water addition method (WA) and the direct dissolution method (DD), have been exploited for the mixed solvent system, which have important influences on aggregation morphology and size. For WA, the polymer is in a molecularly disperse solution of good solvent for both blocks initially, and the aggregation is induced by precipitant addition for one block at a low concentration. At high precipitant concentration, chain exchange is very slow, and thus, despite the same final binary solvent mixture composition, the thermodynamic aggregation is appreciably controlled at low precipitant concentration. For DD, polymer is added as solid to a

binary solvent mixture, and swelling followed by fission can lead to more complex morphologies that may better reflect thermodynamic equilibrium [40]. Spherical micelles assembled in aqueous solutions formed by amphiphilic PS<sub>131</sub>-*b*-PDMAEMA<sub>36</sub> asymmetric diblock [41] and PS<sub>10</sub>-*b*-PDMAEMA<sub>27</sub>-*b*-PS<sub>10</sub> triblock copolymers [42] by WA method have been studied by TEM. However, few works involve the self-assembly aggregations of PS-*b*-PDMAEMA controlled by polymer chain length and environment. In this paper, the correlation of several novel morphologies of linear diblock copolymers PS-*b*-PDMAEMA with different PDMAEMA block lengths in a binary solvent mixture (dioxane/water) using DD method and in pure organic solvents (DMF) with different pH are addressed. Multiple polymeric aggregation conformations are obtained by asymmetric PS<sub>62</sub>-*b*-PDMAEMA<sub>3</sub> compared with semi-symmetric PS<sub>62</sub>-*b*-PDMAEMA<sub>47</sub> and their changing tendencies are discussed in detail.

## 2. Experimental section

### 2.1. Materials

Styrene (S, Aldrich) and dimethylaminoethyl methacrylate (DMAEMA, AR) were purified by reduced pressure distillation to remove inhibitor. The monomers were stored at –5°C for later use. Benzyl bromide (AR) was normally distilled and stored under an argon atmosphere at –5°C. CuBr and 2,2'-bipyridyl were used as received without further purification.

### 2.2. Synthesis of Macroinitiator

In a typical polymerization experiment, 0.20 ml (0.0017 mol) benzyl bromide, 0.265 g (0.0017 mol) 2,2'-bipyridyl and 0.244 g (0.0017 mol) CuBr were placed in a dried 100 ml three-necked flask which was flushed with nitrogen. Pre-degassed styrene (22 ml, 0.1923 mol) was added to the flask immersed in an oil bath at 90°C, and then the solution was magnetically stirred for 5 h under a nitrogen atmosphere. Over this period the originally red translucent polymeric solution turned dark and opaque. After the polymerization was completed, the polymer was diluted by 20 ml THF, and then precipitated in excess methanol after passing through an alumina column. The white powder was

purified by re-dissolution in THF and reprecipitation in methanol, and then dried at 60°C under vacuum.

### 2.3. Synthesis of block copolymerization

Two shares of mixtures containing 1.161 g PS-Br macroinitiator, 0.019 g (0.133 mmol) CuBr, and 0.021 g (0.133 mmol) 2,2'-bipyridyl, 27 ml DMF were respectively introduced into two 50 ml glass vials under nitrogen atmosphere. The ampoules were immersed in an oil bath at 90°C and the ATRPs were started by adding 0.432 ml (2.556 mmol) and 4.321 ml (25.562 mmol) DMAEMA respectively. The reactions were left for 24 h with continuous stirring. After the polymerizations were completed, the former block copolymer 1 (Block 1) was precipitated in methanol while the later (Block 2) in ion-free water after passing through an alumina column, and dried at 60°C under vacuum.

### 2.4. Sample preparation

The samples were prepared by dissolved in pure DMF and dioxane/water (v/v: 94/6) binary solvent mixture using DD method with the same polymer concentration (1 wt%). The pH of copolymer solutions in DMF was regulated by addition amount of *p*-toluene sulphonic acid.

### 2.5. Characterization

*Nuclear Magnetic Resonance Spectra (NMR)*. The  $^1\text{H}$  NMR spectra were registered by using an AVANCE-400MHz (Bruker) spectrophotometer.  $\text{CDCl}_3$  sample solutions (5–10 wt%) were analyzed in tubs of 5 mm, using TMS as internal standard.

*Gel Permeation Chromatography (GPC)*. The analyses were carried out by using a Waters 515 chromatograph equipped with 2 columns Waters Styragel HT 3 and Waters Styragel HT 4, and a dif-

ferential refractive index detector (Waters 2410). The temperature was maintained at 35°C in a Waters column oven. A mixed solvent of  $\text{Et}_3\text{N}$ /THF (v/v: 1/99) (HPLC grade) was used as eluent at 1 ml/min flow rate, and the samples were prepared at concentration of about 5–10 mg/ml in  $\text{Et}_3\text{N}$ /THF. A standard curve was built up by using monodisperse polystyrene samples of molecular weight comprised between 1360 and 2 320 000 g/mol using  $\text{Et}_3\text{N}$ /THF as solvent.

*Elementary Analysis (EA)* Analysis of C, H, and N elements was done using a Vario EL III (ELEMENTAR) element analyzer manufactured by elementary analysis system, Germany.

*Transmission Electron Microscopy (TEM)*. The inner structures of the aggregations are observed by Hitachi-800 transmission electron microscope (Hitachi Co., Tokyo, Japan) operating at 150 kV equipped with Philips PV9900 energy-dispersive analysis of X-rays (EDAX) apparatus and D/max-rB electron diffracting (ED) apparatus. A drop of solution is dispersed onto a solidified epoxy-coated electron microscope grid, stained with 1 wt% potassium phosphotungstate aqueous solution as the negative staining agent, and then quenched with liquid nitrogen.

## 3. Results and discussion

### 3.1. Synthesis and characterization

ATRP is an excellent and well-established method for obtaining block copolymers using simple experimental protocols and a large variety of the available monomers, especially for preparation of amphiphilic block copolymers with well-defined architecture and narrow molecular weight distribution [43–50]. This example demonstrates, in the best way, the features that must be considered for a successful employment of ATRP in block copolymer synthesis. The facile process of polymerization of the amphiphilic block copolymer is depicted in Figure 1.

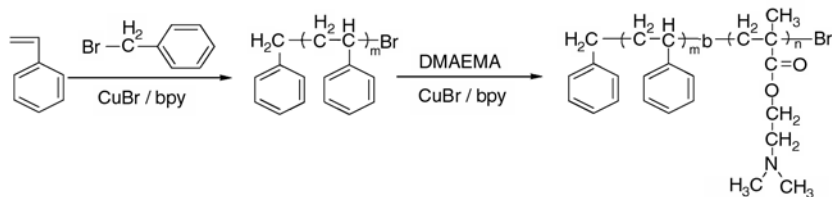


**Figure 1.** Synthesis of PS-*b*-PDMAEMA copolymer

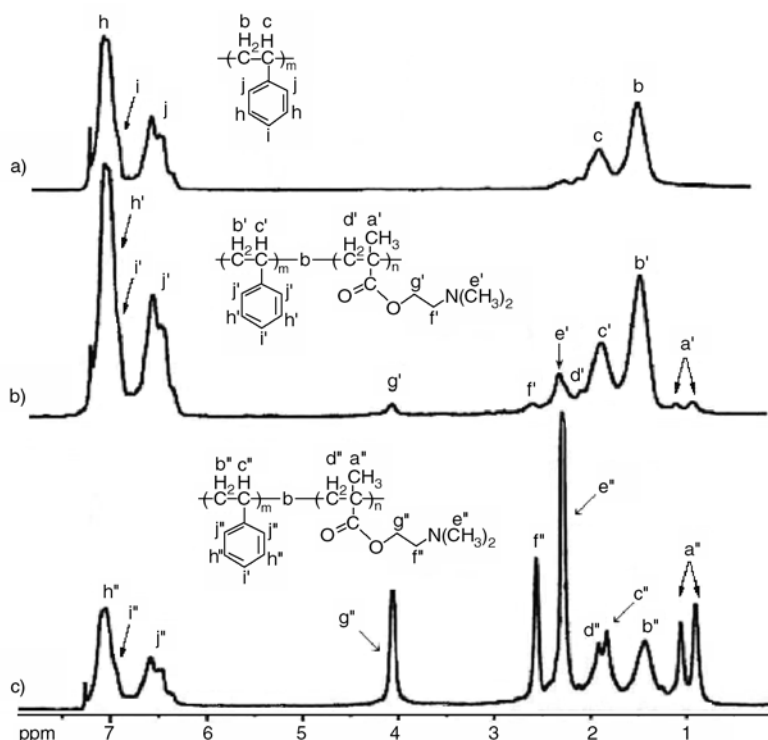


**Figure 2.**  $^1\text{H}$  NMR spectra of the macroinitiator and the block copolymer sample in different forms: (a) Macroinitiator PS-Br; (b) Block 1; (c) Block 2

Figure 2 shows typical  $^1\text{H}$  NMR spectra of bromine-terminated polystyrene as macroinitiator and the block copolymer. Two scales of diblock copolymers, with the same PS block but with different degrees of polymerization of DMAEMA were synthesized. Signals assigned to PS moiety (at  $\delta = 1.4\text{--}1.8$  ppm and  $\delta = 6.4\text{--}7.1$  ppm) and the PDMAEMA moiety (at  $\delta = 0.8\text{--}1.1$  ppm,  $\delta = 2.2\text{--}2.6$  ppm, and  $\delta = 4.1\text{--}4.2$  ppm) are clearly visible.

Single, and symmetrical molecular weight distribution peaks were obtained for all samples (Figure 3). The molecular weight of copolymers mainly depended on the molar ratio of DMAEMA monomer to macroinitiator of PS-Br. The  $M_w/M_n$  values of the polymers measured by gel permeation chromatography (GPC) were 1.20–1.26. The clear shift of the GPC traces toward the higher molecular weights indicated that the macromolecular chains were extended with the second monomer (DMAEMA) in a well-controlled way to form a block copolymer PS-*b*-PDMAEMA. For the sake of clearness, we took the GPC trace of Block 2 for example, which had the longest interval between PS-Br and block copolymer peaks. The GPC trace of Block 2 with longer PDMAEMA segment was a

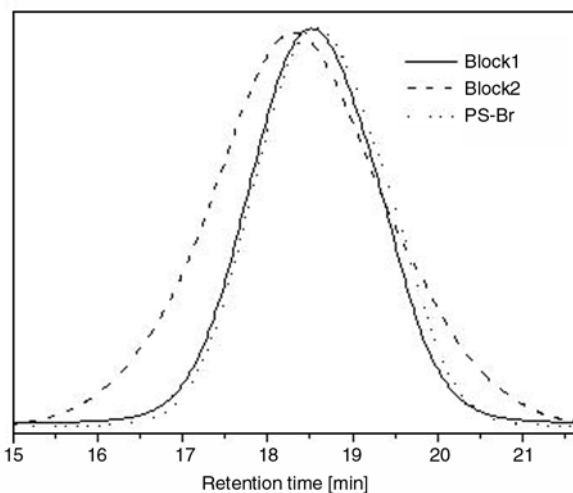


**Figure 3.** GPC traces of samples obtained in the synthesis of PS-*b*-PDMAEMA (their structures and the final characteristics shown in Table 1) using PS-Br as macroinitiator via ATRP process

monodisperse and narrow distributed single peak without shoulder peak, which was evidence that all PS macromolecules were bromine-terminated and had taken part in the polymerization reactions as macroinitiator, that was no PS homopolymer was present in block copolymers. The presence of PDMAEMA in PS-*b*-PDMAEMA was also impossible while the precipitants (methanol for Block 1

**Table 1.** Molecular characteristic of the macroinitiator and the copolymers PS-*b*-PDMAEMA determined by GPC, <sup>1</sup>H NMR and EA analyses

Sample	$M_{n,th}^a$ [g/mol]	Conversion [%]	$M_n^b$ [g/mol]	$M_w^b$ [g/mol]	$M_w/M_n^b$	Polymer structure <sup>b</sup>	m(St)/n(DMAEMA)		
							H NMR	EA	GPC
Macroinitiator	6599	54.56	6429	7829	1.218	PS <sub>62</sub> -Br	–	–	–
Block 1	8184	69.42	6857	8196	1.195	PS <sub>62</sub> - <i>b</i> -PDMAEMA <sub>3</sub>	34.2	36.5	22.7
Block 2	16569	43.65	13876	17525	1.263	PS <sub>62</sub> - <i>b</i> -PDMAEMA <sub>47</sub>	1.31	1.35	1.32

<sup>a</sup>Theoretical number average molecular weight ( $M_{n,th}$ ) calculated from the feed capacity.  $M_{n,th} = (M_m \times \text{Conversion} \times [M]/[I]) + M_i$ , where  $M_m$  and  $M_i$  are the molar masses of monomers and initiator (or macroinitiator), respectively,  $[M]$  and  $[I]$  are the concentration of monomer and initiator (or macroinitiator), respectively

<sup>b</sup>Number average molecular weight ( $M_n$ ), weight average molecular weight ( $M_w$ ), polydispersity index ( $M_w/M_n$ ) and the segment length of the polymers, by GPC

and water for Block 2) were solvents for PDMAEMA homopolymer. Table 1 summarizes the conversions, compositions, theoretical and experimental molecular weights, and molecular weight distributions of a series of PS-*b*-PDMAEMA copolymers via atom transfer radical polymerization.

As the results of Nuclear Magnetic Resonance Spectra (<sup>1</sup>H NMR), Gel Permeation Chromatography (GPC), and Elementary Analysis (EA), we have successfully synthesized a series of amphiphilic polymers with narrow molecular weight distributions.

### 3.2. Self-assembly

The conformational state of the polymers in solution, which is responsible for the compatibility phenomena, depends on the solubility parameter ( $\delta$ ). Dissolution of polymers is optimal where the  $\delta$  values for polymer and solvent are similar (see Table 2) [51]. High dielectric constant ( $\epsilon$ ) values and hydrogen bonding interaction improve the solubility of the corona block [52]. All aspects of the free energy of the aggregation are influenced by solvent. In a polar solvent, the hydrophobic part of the block copolymer will form the core of such micelles, whereas the hydrophilic block is expected to extend into the polar phase [53].

Here we report on the TEM study of the structural nature of PS-*b*-PDMAEMA in DMF with various protonated degrees and in dioxane/water binary solvent mixture (shown in Figure 4, 5, 6 and 9). Table 3 shows the pH- and solvent-dependence of the morphology and size measured from TEM images.

It was found that, with increasing pH, the sequence of copolymer structures in solution follows the order of sphere and hexagonal phase mixtures, spheres, vesicles, pearl necklaces, and finally hexagonal phases. The vesicular morphology is produced by just changes in the solution pH, which suggests that the morphological changes are induced by decreased repulsion (both steric and electrostatic) among the hydrophilic segments as a result of the protonation of PDMAEMA (by *p*-toluene sulphonic acid). All above structures have a phase separated core and a soluble corona controlled by three components of the free energy of aggregation: core-chain stretching, interfacial energy and intercoronal chain interaction [36, 54]. The shade of color of the resulting aggregations can be controlled by adjusting the dyeing time in the negative staining agent.

The plan view electron micrograph images showed that the aggregations consisted of the hexagonal phase, rhombic phase and spherical micellar aggre-

**Table 2.** Solubilities of copolymers and homopolymers in various solvents

Material	H-bond <sup>b</sup>	$\delta$ [(cal/cm <sup>3</sup> ) <sup>1/2</sup> ]	$\epsilon^c$	PS	PDMAEMA	PS- <i>b</i> -PDMAEMA <sup>d</sup>	
						95% (Block 1)	57% (Block 2)
DMF	m	12.1	36.7	+ + <sup>a</sup>	+	+ +	+ +
Water	s	23.4	80.1	– – <sup>a</sup>	+ +	– –	– –
1,4-Dioxane	m	10.0	2.21*	+ +	– –	+ +	+ <sub>a</sub>

<sup>a</sup>(+ +) readily soluble (10%, r. t); (– –) insoluble; (+) soluble.

<sup>b</sup>H-bond: hydrogen bond; s-strongly m-moderately ib.

<sup>c</sup>dielectric constant (20°C); \*25°C; from reference 53.

<sup>d</sup>weight fractions of styrene in the copolymers are 95% and 57%, respectively.



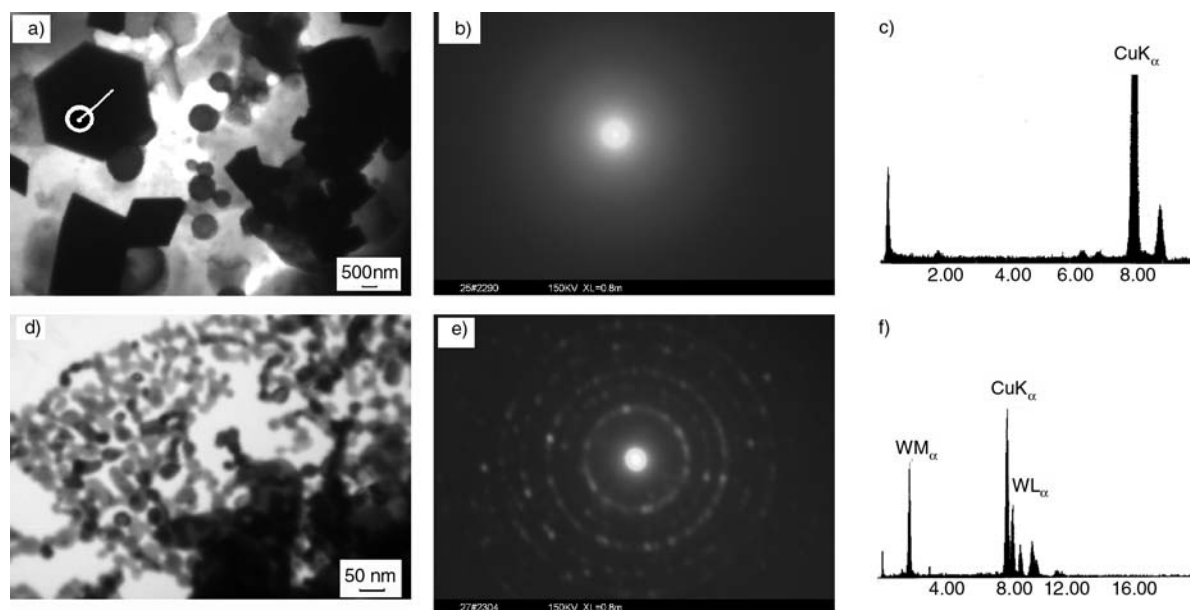


**Figure 4.** TEM images, electron diffracting (ED) patterns, and energy-dispersive analysis of X-rays (EDAX) spectra of the aggregations self-assembled by 1 wt% PS<sub>62</sub>-*b*-PDMAEMA<sub>3</sub> in DMF at pH = 1 (a, b, c) and crystal of negative staining agent (d, e, f) used in TEM

**Table 3.** Summary of the effect of solvent polarity or pH on the morphology for PS-*b*-PDMAEMA

Solvent		Block 1		Block 2	
		Morphology	Size <sup>a</sup> [nm]	Morphology	Size <sup>a</sup> [nm]
DMF	pH = 1	hexagonal/rhombic phases	443–1131	hexagonal/rhombic phases	714–988
		spherical micelles	668–1310		
	pH = 2	spherical micelles	420–768	hexagonal/rhombic phases	226–1710
	pH = 4	vesicles	370–690	spherical micelles	7–9
	pH = 5	necklace-like micelles	208–320	spherical micelles	4–5
dioxane/water		hexagonal/rhombic phases	1948–3638		
		large compound micelles	89–499	spherical micelles	73–194
		vesicles	48–232		

<sup>a</sup>The values listed in the table are the diameters of micelles and vesicles or the side lengths of hexagonal/rhombic particles.

gations self-assembled by 1 wt% PS<sub>62</sub>-*b*-PDMAEMA<sub>3</sub> in DMF at pH = 1 and crystal of negative staining agent, as shown in Figure 4a and Figure 4d. To our knowledge, only inorganic compounds and a few organic compounds can form highly symmetrical crystal. It seems incredible that an amorphous polymer, such as PS-*b*-PDMAEMA, can self-assemble into a highly symmetrical structure such as a hexagonal phase or a rhombic phase. To confirm the composition of the hexagonal particles, the corresponding selected area energy-dispersive analysis of X-rays (EDAX) spectrum is shown in Figure 4c, compared with the EDAX spectrum of potassium phosphotungstate in Figure 4f, by which elemental composition of aggregations were analyzed to shed light on the structure. The strong Cu signal is caused by the sample holder (copper grid). We did not detect any signals corresponding

to inorganic compounds, indicating our purification of the powder of the copolymer of PS-*b*-PDMAEMA eliminated any inorganic impurity. The selected area diffraction patterns are shown in Figure 4b and Figure 4e. The intensity of the rings from the hexagonal phases is hazy and decrescent indicating that the phases do not have a preferred orientation just as crystal. Contrarily, the superimposed rings originating from electron diffraction from crystal of potassium phosphotungstate were composed of bright spots. We judge that this lack of preferred orientation in hexagonal phase might be due to the undefined arrangement of macromolecules holding long chains and a great deal of atoms. By combining these three techniques, detailed information on the elemental component and the two-dimensional structure of aggregations could be determined.

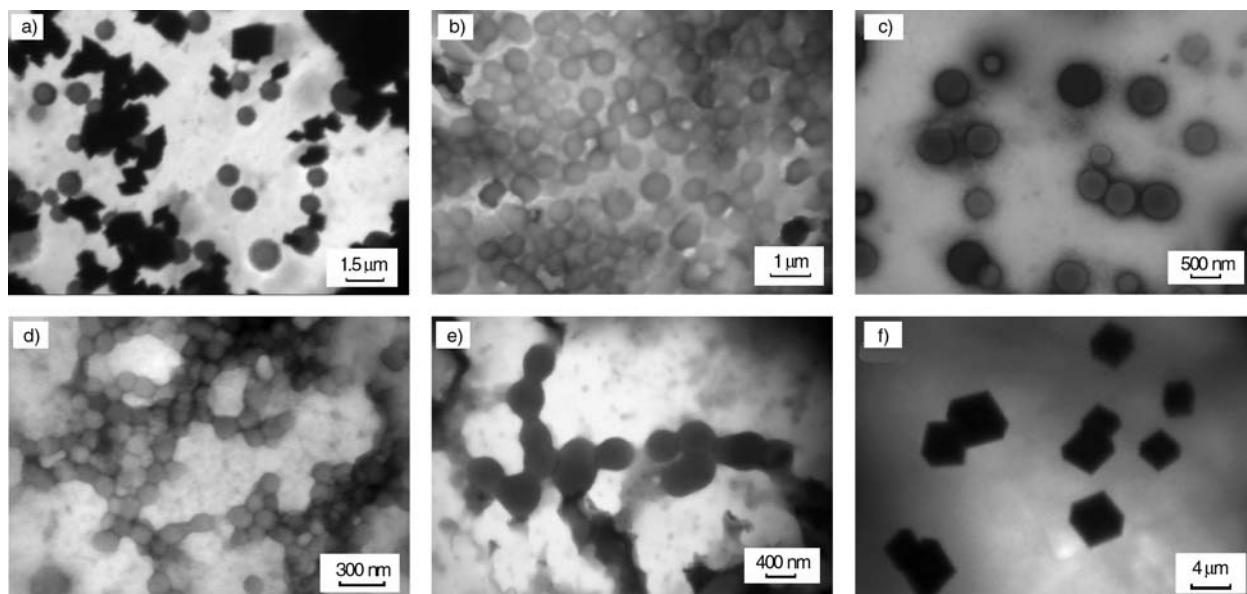


**Figure 5.** TEM images of the aggregations self-assembled by 1 wt% PS<sub>62</sub>-*b*-PDMAEMA<sub>3</sub> in DMF at pH = 1 (a); pH = 2 (b); pH = 4 (c) and pH = 5 (d, e, f)

First time Shen and Eisenberg reported of the formation of hexagonal particles self-assembled by 10.0 wt% asymmetric amphiphilic PS<sub>49</sub>-*b*-PAA<sub>7.2</sub> in dioxane/water (w/w: 63/37) mixture [29]. They presumed that the inverted morphologies were so compact that no internal structure could be seen, probably because of the very small diameters of the hollow rod regions that the short PAA blocks produced in the PS domain. Here we obtained much larger and regular hexagonal and rhombic structures in DMF self-assembled by not only the asymmetric amphiphilic PS<sub>62</sub>-*b*-PDMAEMA<sub>3</sub> at pH = 1 (Figure 4a and 5a) and pH = 5 (Figure 5f) but also the semi-symmetric PS<sub>62</sub>-*b*-PDMAEMA<sub>47</sub> at pH = 1 (Figure 9a) and pH = 2 (Figure 9b). For the coexistence of large dimensioned hexagonal/ rhombic structure and spherical micelles, we believe that the hexagonal/rhombic structure is formed by the second aggregation of very small PS-*b*-PDMAEMA micelles with higher total surface areas and energy than the larger micelles (Figure 7a and 10a).

For linear PS-*b*-PDMAEMA in polar solvent, the corona repulsion force and the core dimension determined the morphology. In DMF solvent, the corona repulsion force of PDMAEMA blocks with high degree of protonation controlled by addition amount of *p*-toluene sulphonic acid was dominant and thus the sphere morphology was observed. We can clearly see coexistence of spherical nanoparticles with the sizes between 700 and 1000 nm, having a phase-separated PS core and a PDMAEMA corona (Figure 7b and 10b), and hexagonal particles in Figure 5a. The hexagonal particles totally disappear and only spherical micelles exist when pH is further increased to 2. The micelles have a nearly spherical shape and an average diameter of 500 nm, as shown in Figure 5b.

When the pH of solution is increased, the size of morphologies, as listed in Table 3, decreases. Much smaller micelles with average diameters decreasing from about 8 to 5 nm are also formed by PS<sub>62</sub>-*b*-PDMAEMA<sub>47</sub> while the solution pH increases from 4 to 5 (Figure 9c and 9d). While longer corona

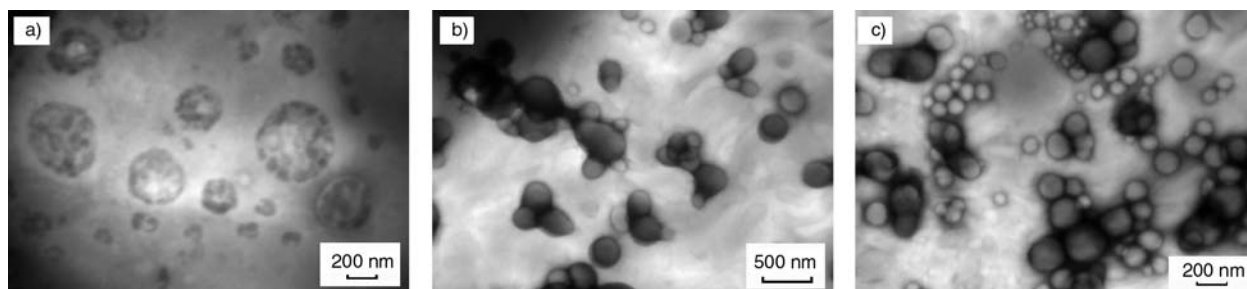


**Figure 6.** TEM images of the aggregations self-assembled by 1 wt% PS<sub>62</sub>-*b*-PDMAEMA<sub>3</sub> in dioxane/water (v/v: 94/6)

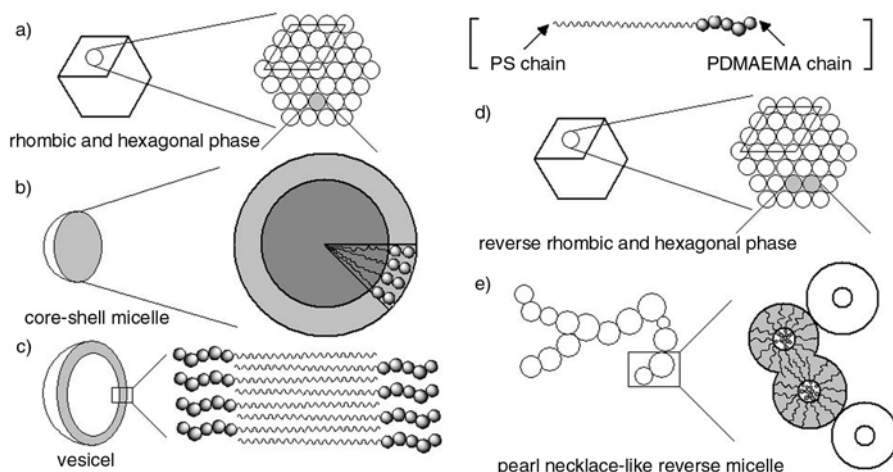


**Figure 7.** Proposed chain architectures of block copolymers  $\text{PS}_{62}\text{-}b\text{-PDMAEMA}_3$  in the hexagonal/rhombic phase (a), spherical core-shell micelle (b), vesicle (c), reverse rhombic/hexagonal phase (d), and pearl necklace-like reverse micelle (e)

chain makes the micellar aggregation number decrease [30], the micelles formed by  $\text{PS}_{62}\text{-}b\text{-PDMAEMA}_{47}$  are smaller than those self-assembled by  $\text{PS}_{62}\text{-}b\text{-PDMAEMA}_3$ , though the former molecule is larger. For the weaker electrostatic repulsive force between corona PDMAEMA chains, smaller micelles are formed by  $\text{PS}_{62}\text{-}b\text{-PDMAEMA}_{47}$  in solution pH = 5 self-assembled by less molecules than pH = 4. Meanwhile, the quantity of spherical micelles also increases obviously. Figure 5c shows TEM image of vesicular aggregations self-assembled by 1 wt%  $\text{PS}_{62}\text{-}b\text{-PDMAEMA}_3$  in DMF at pH = 4. Well defined closed bilayer structures are seen in the image. The contrast in the images Figure 5b and Figure 5c can be directly understood as the vesicular structure with a dark halo surrounding the grayer interior. For  $\text{PS}_{62}\text{-}b\text{-PDMAEMA}_3$ , the weaker the electrostatic repulsive force is, the lower the morphological curvature is. Lower curvature makes the vesicular structure appear (Figure 7c).

Core-shell micelles are present again and coexist with sheer hexagonal phases self-assembled by

1 wt%  $\text{PS}_{62}\text{-}b\text{-PDMAEMA}_3$  in DMF at pH = 5. Their low magnification images are shown in Figure 5d, 5e and Figure 5f. The micelles are seen to have sizes down to 250 nm compared with micelles with a bigger average diameter of 500 nm in Figure 5b. Typically, with increasing pH condition, the micelles are connected by bridging chains yielding a bunch structure that exhibits interesting necklace shape, with occasional multifunctional beads maintaining the gelled network. The pearl necklace morphology is most likely a result of the acid driving the spheres to form rods. However, the glassy nature of the PS cores of the beads makes it impossible to complete the transformation. The pearl necklace thus represents an intermediate step between spheres and rods [54]. Furthermore, hexagonal and rhombic phases with side length on the order of  $\sim 3\text{ }\mu\text{m}$  are prepared in DMF at pH = 5 (Figure 5f). Their three-dimensional structures are especially important to be understood in the study of such large regions of the detailed image contrast in such polygonal shape.

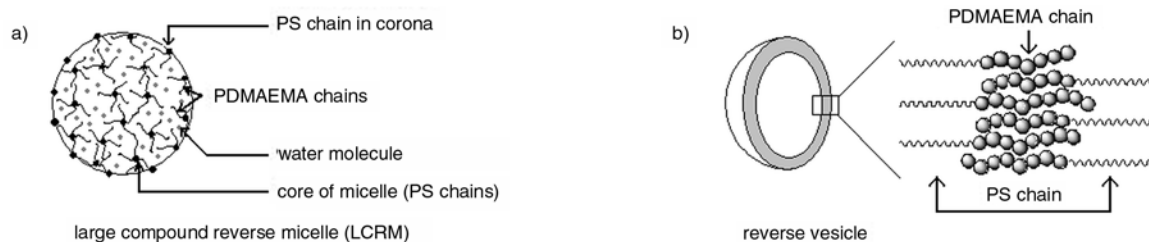


**Figure 8.** Proposed chain architectures of block copolymers  $\text{PS}_{62}\text{-}b\text{-PDMAEMA}_3$  in the large compound reverse micelle (LCRM) (a), and reverse vesicle (b)

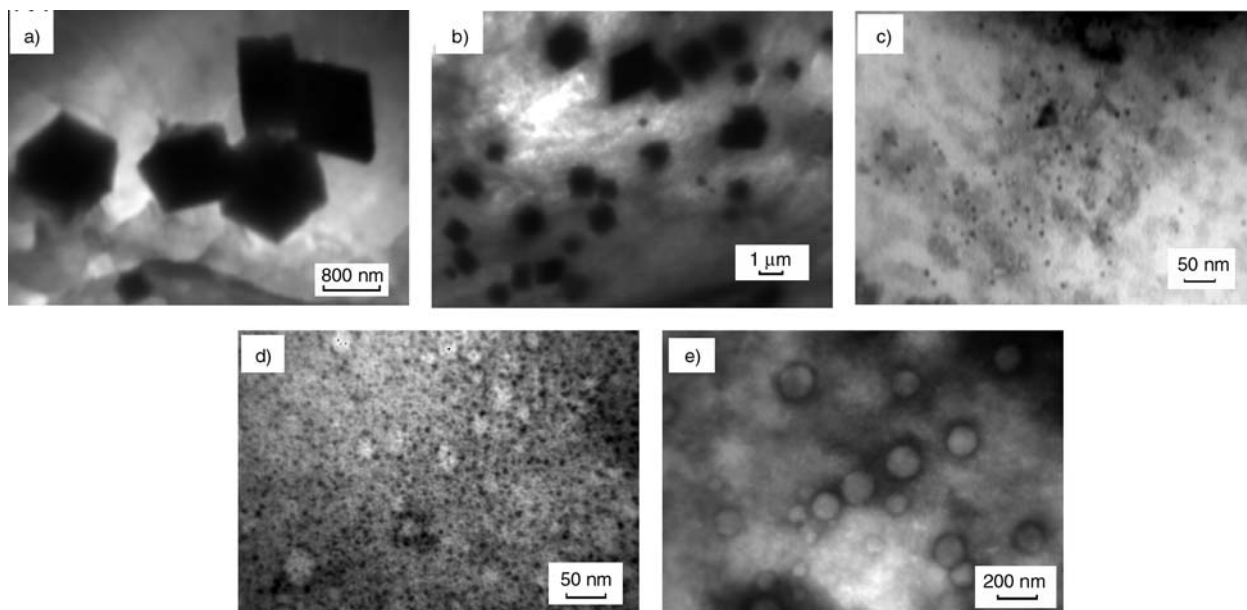


**Figure 9.** TEM images of the aggregates self-assembled by 1 wt% PS<sub>62</sub>-*b*-PDMAEMA<sub>47</sub> in DMF at pH = 1 (a); pH = 2 (b); pH = 4 (c); pH = 5 (d); and in dioxane/water (v/v: 94/6) (e)

Because the protonation degree of PDMAEMA block in PS<sub>62</sub>-*b*-PDMAEMA<sub>3</sub> is much lower in DMF at pH = 5 than at pH = 2, the electrostatic repulsion should not contribute much to the smaller spherical morphology through vesicular morphology transition. The effect of the other two parameters, the interface tension at the core-corona interface and the stretching (deformation) of the core-forming blocks in the core, may affect the final morphology. As DMF is the common solvent for both PS and PDMAEMA blocks (Table 2), the polarity of PDMAEMA block decreases according to the pH increasing, which induces the interface tension at the core-corona interface decrease. It's likely that the PS stretching and decreased interface tension cause the morphology change from vesicle to pearl necklace-like reverse micelle with PS corona and PDMAEMA core. The fusion between

reverse micelles might be caused by interpenetration of PS blocks in corona (Figure 7e). We proposed that the hexagonal/rhombic structure is also a reverse phase and formed by the second aggregation of very small PS<sub>62</sub>-*b*-PDMAEMA<sub>3</sub> reverse micelles (Figure 7d).

With increasing hydrophobic characteristic of the solvent in dioxane/water (v/v: 94/6) mixture compared with DMF, we observed the large compound reverse micelles (LCRMs) which are spherical and highly polydisperse formed by secondary aggregation of reverse micelles self-assembled by PS<sub>62</sub>-*b*-PDMAEMA<sub>3</sub> (Figure 6a). The LCRMs formation is illustrated that islands of PS chains are presumed in a continuous phase of core-forming polymer (PDMAEMA) all of which is surrounded by the solvent soluble PS corona (Figure 8a). The model is enlightened by Eisenberg who proposed the LCRMs

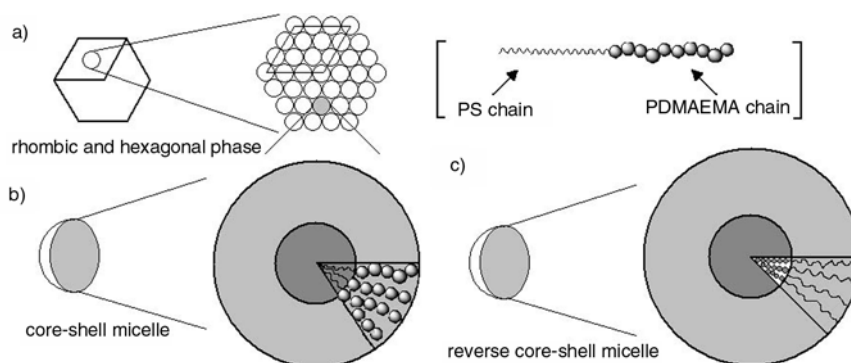


**Figure 10.** Proposed chain architectures of block copolymers PS<sub>62</sub>-*b*-PDMAEMA<sub>47</sub> in the hexagonal/rhombic phase (a), spherical core-shell micelle (b), and reverse spherical core-shell micelle (c)



formed by PS-*b*-PAA in aqueous solution bore a strong resemblance to bulk reverse micelles, which present a further solution to the problem of how to arrange a large, insoluble block where the solubilizing block is very short [55]. Vesicles are also coexisting in the solvent mixture (Figure 6b and 6c).

A striking model of the proposed chain architectures of block copolymers PS<sub>63</sub>-*b*-PDMAEMA<sub>3</sub> in the hexagonal/rhombic phase, spherical core-shell micelle, vesicle, reverse hexagonal/rhombic phase, pearl necklace-like reverse micelle is proposed in Figure 7 and large compound reverse micelle (LCRM), reverse vesicle in Figure 8. For polystyrene with PDMAEMA hydrophilic end-caps and a molecular weight greater than small molecular surfactant, PS<sub>62</sub>-*b*-PDMAEMA<sub>3</sub> copolymers self-assemble into big size core-shell micelles or large compound reverse micelles (LCRMs) consisting of a hydrophilic core that is surrounded by a corona of PS segment. Typically, the higher pH condition of solvent decreases the electrostatic repulsion of these positively charged PDMAEMA head-groups due to the lower charge density, which causing the size of the aggregation decrease.

It is found that the aggregation configuration self-assembled by 1 wt% PS<sub>62</sub>-*b*-PDMAEMA<sub>47</sub> (core-shell micelle) remains unchanged with pH shift in DMF from 4 to 5. And also, in dioxane/water (v/v: 94/6) solvent mixture, only reverse core-shell micelles are obtained (Figure 9e). From the TEM results in Figure 9, the self-assembly microstructure of PS<sub>62</sub>-*b*-PDMAEMA<sub>47</sub> based on the aggregation mechanism as depicted in Figure 10 is proposed.

#### 4. Conclusions

In this study, amphiphilic linear block copolymer with one block of polystyrene (PS) and another environmental-sensitive block of poly (dimethylaminoethyl methacrylate) (PDMAEMA) were successfully synthesized by atom transfer radical polymerization.

We report on transmission electron microscopy (TEM) based structural studies of the self-assembly behavior of PS-*b*-PDMAEMA. Indeed our experiments have reported changes in the structure of aggregations formed by PS<sub>62</sub>-*b*-PDMAEMA<sub>3</sub> resulting from changing in solvent and in charge density by adjusting solvent acidity. A rich variety in the image contrast is observed. At the same time,

PS<sub>62</sub>-*b*-PDMAEMA<sub>47</sub> copolymers are in the form of micelles in different solvent. Besides simple, core-shell micelles, large compound reverse micelles (LCRMs), vesicles, reverse vesicles, hexagonal phase, reverse hexagonal phase and pearl necklace-like micellar aggregates have been prepared from asymmetric diblock copolymers PS<sub>62</sub>-*b*-PDMAEMA<sub>3</sub> in dilute solution (1 wt%). This study illustrates the chain architectures of block copolymers in the morphologies of molecular self-assembled nanostructures. Some of the aggregates may have potential applications in areas such as separations and drug delivery systems. When the PS block length is nearly equivalent to the PDMAEMA block length, most of the aggregates of semi-symmetric diblock copolymers PS<sub>62</sub>-*b*-PDMAEMA<sub>47</sub> in organic solvent (DMF) or binary solvent mixture (dioxane/water, v/v: 94/6) are spherical, with a core-shell structure.

We note that the larger size of aggregations is due to their electrostatic repulsion of these positively charged PDMAEMA head-groups and their low surface curvature associated energy. The participation of polymers in aggregations enhances the configuration stability caused by the viscosity between polymeric long chains. Moreover, their large surface-to-volume ratio makes them sensitive to environmental conditions, which are intimately linked to their structural reorganization, including size, shape, bulk (interior), and surface bonding. All above structures are controlled by three components of the free energy of aggregation: core-chain stretching, interfacial energy and intercoronal chain interaction.

#### Acknowledgements

The work was financially supported by National Natural Science Foundation of China (No. 20674045), Shandong Provincial Natural Science Foundation (No.Y2007B34) and the Scientific Research Foundation for the Returned Overseas Chinese Scholars, State Education Ministry.

#### References

- [1] Alvarez-Lorenzo C., Barreiro-Iglesias R., Concheiro A., Iourtchenko L., Alakhov V., Bromberg L., Temchenko M., Deshmukh S., Hatton T. A.: Biophysical characterization of complexation of DNA with block copolymers of poly(2-dimethylaminoethyl) methacrylate, poly(ethylene oxide), and poly(propylene oxide). *Langmuir*, **21**, 5142–5148 (2005).

- [2] Even M., Haddleton D. M., Kukulj D.: Synthesis and characterization of amphiphilic triblock polymers by copper mediated living radical polymerization. *European Polymer Journal*, **39**, 633–639 (2003).
- [3] Jiang X., Lok M. C., Hennink W. E.: Degradable-brushed PHEMA-PDMAEMA synthesized via ATRP and click chemistry for gene delivery. *Bioconjugate Chemistry*, **18**, 2077–2084 (2007).
- [4] Khelfallah N. S., Peretolchin M., Klapper M., Müllen K.: Controlled radical polymerization of N,N-dimethylaminoethyl methacrylate using triazolynyl as counter radical. *Polymer Bulletin*, **53**, 295–304 (2005).
- [5] Rakhmatullina E., Braun T., Kaufmann T., Spillmann H., Malinova V., Meier W.: Functionalization of gold and silicon surfaces by copolymer brushes using surface-initiated ATRP(a). *Macromolecular Chemistry and Physics*, **208**, 1283–1293 (2007).
- [6] Wang X., Winnik M. A., Manners I.: Synthesis and self-assembly of poly(ferrocenyldimethylsilane-*b*-dimethylaminoethyl methacrylate): Toward water-soluble cylinders with an organometallic core. *Macromolecules*, **38**, 1928–1935 (2005).
- [7] Baines F. L., Armes S. P., Billingham N. C., Tuzar Z.: Micellization of poly(2-(dimethylamino)ethyl methacrylate-*block*-methyl methacrylate) copolymers in aqueous solution. *Macromolecules*, **29**, 8151–8159 (1996).
- [8] Baines F. L., Billingham N. C., Armes S. P.: Synthesis and solution properties of water-soluble hydrophilic-hydrophobic block copolymers. *Macromolecules*, **29**, 3416–3420 (1996).
- [9] Baines F. L., Dionisio S., Billingham N. C., Armes S. P.: Use of block copolymer stabilizers for the dispersion polymerization of styrene in alcoholic media. *Macromolecules*, **29**, 3096–3102 (1996).
- [10] Costa A. C., Geoghegan M., Vlcek P., Composto R. J.: Block copolymer adsorption from a homopolymer melt to silicon oxide: Effects of nonadsorbing block length and anchoring block-substrate interaction. *Macromolecules*, **36**, 9897–9904 (2003).
- [11] Ni P., Zhang M., Ma L., Fu S.: Poly(dimethylamino) ethyl methacrylate for use as a surfactant in the mini-emulsion polymerization of styrene. *Langmuir*, **22**, 6016–6023 (2006).
- [12] Zhang X., Matyjaszewski K.: Synthesis of well-defined amphiphilic block copolymers with 2-(dimethylamino)ethyl methacrylate by controlled radical polymerization. *Macromolecules*, **32**, 1763–1766 (1999).
- [13] Zhao B., Brittain W. J.: Synthesis, characterization, and properties of tethered polystyrene-*b*-polyacrylate brushes on flat silicate substrates. *Macromolecules*, **33**, 8813–8820 (2000).
- [14] Xiong Q., Ni P., Zhang F., Yu Z.: Synthesis and characterization of 2-(dimethylamino)ethyl methacrylate homopolymers via aqueous RAFT polymerization and their application in miniemulsion polymerization. *Polymer Bulletin*, **53**, 1–8 (2004).
- [15] Lokaj J., Vlcek P., Kriz J.: Synthesis of polystyrene-poly(2-(dimethylamino)ethyl methacrylate) block-copolymers by stable free-radical polymerization. *Macromolecules*, **30**, 7644–7646 (1997).
- [16] Allen C., Han J. N., Yu Y. S., Maysinger D., Eisenberg A.: Polycaprolactone-*b*-poly(ethylene oxide) copolymer micelles as a delivery vehicle for dihydrotestosterone. *Journal of Controlled Release*, **63**, 275–286 (2000).
- [17] Allen C., Maysinger D., Eisenberg A.: Nano-engineering block copolymer aggregates for drug delivery. *Colloids and Surfaces B: Biointerfaces*, **16**, 3–27 (1999).
- [18] Allen C., Yu Y., Maysinger D., Eisenberg A.: Polycaprolactone-*b*-poly(ethylene oxide) block copolymer micelles as a novel drug delivery vehicle for neurotrophic agents FK506 and L-685,818. *Bioconjugate Chemistry*, **9**, 564–572 (1998).
- [19] Bronich T. K., Kabanov A. V., Kabanov V. A., Yu K., Eisenberg A.: Soluble complexes from poly(ethylene oxide)-*block*-polymethacrylate anions and N-alkylpyridinium cations. *Macromolecules*, **30**, 3519–3525 (1997).
- [20] Bronich T. K., Popov A. M., Eisenberg A., Kabanov V. A., Kabanov A. V.: Effects of block length and structure of surfactant on self-assembly and solution behavior of block ionomer complexes. *Langmuir*, **16**, 481–489 (2000).
- [21] Discher D. E., Eisenberg A.: Polymer vesicles. *Science*, **297**, 967–973 (2002).
- [22] Kabanov A. V., Bronich T. K., Kabanov V. A., Yu K., Eisenberg A.: Spontaneous formation of vesicles from complexes of block ionomers and surfactants. *Journal of the American Chemical Society*, **120**, 9941–9942 (1998).
- [23] Eisenberg A., Liu F. T.: Preparation and pH triggered inversion of vesicles from poly(acrylic acid)-*block*-polystyrene-*block*-poly(4-vinyl pyridine). *Journal of the American Chemical Society*, **125**, 15059–15064 (2003).
- [24] Luo L. B., Eisenberg A.: Thermodynamic size control of block copolymer vesicles in solution. *Langmuir*, **17**, 6804–6811 (2001).
- [25] Luo L. B., Eisenberg A.: Thermodynamic stabilization mechanism of block copolymer vesicles. *Journal of the American Chemical Society*, **123**, 1012–1013 (2001).
- [26] Moffitt M., Vali H., Eisenberg A.: Spherical assemblies of semiconductor nanoparticles in water-soluble block copolymer aggregates. *Chemistry of Materials*, **10**, 1021–1028 (1998).
- [27] Savic R., Luo L., Eisenberg A., Maysinger D.: Micellar nanocontainers distribute to defined cytoplasmic organelles. *Science*, **300**, 615–618 (2003).
- [28] Shen H. W., Eisenberg A.: Morphological phase diagram for a ternary system of block copolymer PS(310)-*b*-PAA(52)/dioxane/H<sub>2</sub>O. *Journal of Physical Chemistry, B*, **103**, 9473–9487 (1999).

- [29] Shen H. W., Eisenberg A.: Block length dependence of morphological phase diagrams of the ternary system of PS-*b*-PAA/dioxane/H<sub>2</sub>O. *Macromolecules*, **33**, 2561–2572 (2000).
- [30] Shen H. W., Zhang L. F., Eisenberg A.: Multiple pH-induced morphological changes in aggregates of polystyrene-block-poly(4-vinylpyridine) in DMF/H<sub>2</sub>O mixtures. *Journal of the American Chemical Society*, **121**, 2728–2740 (1999).
- [31] Soo P. L., Eisenberg A.: Preparation of block copolymer vesicles in solution. *Journal of Polymer Science, Part B: Polymer Physics*, **42**, 923–938 (2004).
- [32] Yu G. E., Eisenberg A.: Multiple morphologies formed from an amphiphilic ABC triblock copolymer in solution. *Macromolecules*, **31**, 5546–5549 (1998).
- [33] Yu K., Eisenberg A.: Bilayer morphologies of self-assembled crew-cut aggregates of amphiphilic PS-*b*-PEO diblock copolymers in solution. *Macromolecules*, **31**, 3509–3518 (1998).
- [34] Yu Y., Eisenberg A.: Control of morphology through polymer-solvent interactions in crew-cut aggregates of amphiphilic block copolymers. *Journal of the American Chemical Society*, **119**, 8383–8384 (1997).
- [35] Yu Y., Zhang L., Eisenberg A.: Morphogenic effect of solvent on crew-cut aggregates of amphiphilic diblock copolymers. *Macromolecules*, **31**, 1144–1154 (1998).
- [36] Zhang L., Eisenberg A.: Morphogenic effect of added ions on crew-cut aggregates of polystyrene-*b*-poly(acrylic acid) block copolymers in solutions. *Macromolecules*, **29**, 8805–8815 (1996).
- [37] Zhang L., Eisenberg A.: Formation of crew-cut aggregates of various morphologies from amphiphilic block copolymers in solution. *Polymers for Advanced Technologies*, **9**, 677–699 (1998).
- [38] Zhang L. F., Eisenberg A.: Thermodynamic vs kinetic aspects in the formation and morphological transitions of crew-cut aggregates produced by self-assembly of polystyrene-*b*-poly(acrylic acid) block copolymers in dilute solution. *Macromolecules*, **32**, 2239–2249 (1999).
- [39] Zhang L. F., Shen H. W., Eisenberg A.: Phase separation behavior and crew-cut micelle formation of polystyrene-*b*-poly(acrylic acid) copolymers in solutions. *Macromolecules*, **30**, 1001–1011 (1997).
- [40] Cameron N. S., Corbierre M. K., Eisenberg A.: 1998 E.W.R. Steacie award lecture asymmetric amphiphilic block copolymers in solution: A morphological wonderland. *Canadian Journal of Chemistry*, **77**, 1311–1326 (1999).
- [41] Wang X. Y., Zhu J., Zhou D., Zhu X. L.: Reversible addition-fragmentation chain transfer free-radical polymerization of 2-(dimethylamino) ethyl methacrylate and synthesis of derived block polymer (in Chinese). *Petrochemical Technology*, **34**, 536–540 (2005).
- [42] Chen W.-X., Fan X.-D., Liu Y.-Y.: Synthesis and characterization of amphiphilic triblock copolymers and their self-assembly in aqueous solution. *Polymer Materials Science and Engineering*, **22**, 88–92 (2006).
- [43] Kajiwarra A., Matyjaszewski K.: Formation of block copolymers by transformation of cationic ring-opening polymerization to atom transfer radical polymerization (ATRP). *Macromolecules*, **31**, 3489–3493 (1998).
- [44] Lee S. B., Russell A. J., Matyjaszewski K.: ATRP synthesis of amphiphilic random, gradient, and block copolymers of 2-(dimethylamino)ethyl methacrylate and *n*-butyl methacrylate in aqueous media. *Bio-macromolecules*, **4**, 1386–1393 (2003).
- [45] Matyjaszewski K., Göbelt B., Paik H.-J., Horwitz C. P.: Tridentate nitrogen-based ligands in Cu-based ATRP: A structure-activity study. *Macromolecules*, **34**, 430–440 (2001).
- [46] Mühlebach A., Gaynor S. G., Matyjaszewski K.: Synthesis of amphiphilic block copolymers by atom transfer radical polymerization (ATRP). *Macromolecules*, **31**, 6046–6052 (1998).
- [47] Neugebauer D., Zhang Y., Pakula T., Sheiko S. S., Matyjaszewski K.: Densely grafted and double-grafted PEO brushes via ATRP. A route to soft elastomers. *Macromolecules*, **36**, 6746–6755 (2003).
- [48] Shinoda H., Miller P. J., Matyjaszewski K.: Improving the structural control of graft copolymers by combining ATRP with the macromonomer method. *Macromolecules*, **34**, 3186–3194 (2001).
- [49] Barim G., Demirelli K., Coskun M.: Conventional and atom transfer radical copolymerization of phenoxycarbonylmethyl methacrylate-styrene and thermal behavior of their copolymers. *Express Polymer Letters*, **1**, 535–544 (2007).
- [50] Lu X. J., Meng L. Z., Zhong X. X.: Novel fluorescent amphiphilic block copolymers: Photophysics behavior and interactions with DNA. *Express Polymer Letters*, **1**, 356–363 (2007).
- [51] Brandrup J., Immergut E. H.: *Polymer handbook*. Wiley, New York (1975).
- [52] Cheng N., Hu S.: *Solvent handbook*. Chinese Chemical Engineering Press, Beijing (1986).
- [53] Hickl P., Ballauff M., Jada A.: Small-angle X-ray contrast-variation study of micelles formed by poly(styrene)-poly(ethylene oxide) block copolymers in aqueous solution. *Macromolecules*, **29**, 4006–4014 (1996).
- [54] Zhang L., Yu K., Eisenberg A.: Ion-induced morphological changes in ‘crew-cut’ aggregates of amphiphilic block copolymers. *Science*, **272**, 1777–1779 (1996).
- [55] Zhang L., Eisenberg A.: Multiple morphologies of ‘crew-cut’ aggregates of polystyrene-*b*-poly(acrylic acid) block copolymer. *Science*, **268**, 1728–1731 (1995).

# Studies on the influence of structurally different peroxides in polypropylene/ethylene alpha olefin thermoplastic vulcanizates (TPVs)

R. R. Babu, N. K. Singha, K. Naskar\*

Rubber Technology Centre, Indian Institute of Technology, Kharagpur-721302, West Bengal, India

Received 21 January 2008; accepted in revised form 15 February 2008

**Abstract.** Novel thermoplastic vulcanizates (TPVs) based on polypropylene (PP) and new generation ethylene-octene copolymer (EOC) have been developed by dynamic vulcanization process, which involves melt-mixing and simultaneously crosslinking a rubber with a thermoplastic. In this paper technologically compatibilized blends of PP and EOC were dynamically vulcanized by coagent assisted peroxide crosslinking system. The effect of structurally different types of peroxides, namely dicumyl peroxide, di-tert butyl peroxy isopropyl benzene and tert-butyl cumyl peroxide with varying concentrations on the properties on TPVs was mainly studied. The physico-mechanical, thermal and morphological properties of these TPVs were characterized by using X-ray diffraction (XRD), differential scanning calorimeter (DSC) and scanning electron microscopy (SEM).

**Keywords:** polymer blends and alloys, polypropylene, ethylene octene copolymer, thermoplastic vulcanizate, peroxide

## 1. Introduction

Thermoplastic Elastomers (TPEs) have the processing characteristics of a thermoplastic and functional performance of a conventional thermoset rubber. TPEs are gaining importance day-by-day because of their wide range of applications especially in the automotive industries [1]. TPEs can be broadly classified into two groups: block copolymers and rubber–plastic blends. Blending of two or more polymers can give rise to better balance of properties than that of individual components. Polyolefin based blends have attracted much attention due to easy processability and broad spectrum of properties which can also be obtained at competitive price. Dynamic vulcanization is the process of mixing a thermoplastic and a rubber, and the latter is being cross-linked under dynamic conditions. The process needs to be carried out at high shear

rate above the melting temperature of thermoplastic and also at sufficiently high temperature to activate and to complete the process of vulcanization. The material prepared, so called thermoplastic vulcanizate (TPVs) or dynamic vulcanizate is characterized by processing behavior like thermoplastic at elevated temperature and performance properties of vulcanized rubber at ambient temperature [2]. In this dynamic vulcanization, small cross-linked rubber particles are dispersed in the uncross-linked thermoplastic polymer matrix as microgels, although the content of rubber exceeds the thermoplastic content in most cases. Dynamic vulcanization is a route to configure thermoplastic elastomer, which have better properties than those of conventional block co-polymer TPEs. Gessler was the first to claim dynamically vulcanized blends in 1962 [3]. Significant improvement in the field of TPVs

\*Corresponding author, e-mail: [knaskar@rtc.iitkgp.ernet.in](mailto:knaskar@rtc.iitkgp.ernet.in)  
© BME-PT and GTE



was achieved by Coran and Patel [4] by fully vulcanizing the rubbery phase without affecting the thermoplasticity of the blends. Further development in this field was advanced by Abdou-Sabet and Fath [5] by using phenolic resin as curative in polypropylene/ ethylene propylene diene rubber (PP/EPDM) which not only crosslink rubbery phase but also involve in compatibilizing the two phases by forming graft-links between the blend components. Though several cross-linking agents have been employed to cross-link the elastomer phase in TPVs, the phenolic resin, peroxide and silane cross-linking systems have gained considerable commercial importance. Major advantages of using peroxide cross-linking system are that they have improved high temperature resistance, reduced compression set, their ability to vulcanize both saturated and unsaturated rubbers and reversion resistance [6]. Besides the advantages of peroxide, there are also some disadvantages like radical transfer, polymer scission, dehydrohalogenation (in halogenated polymers like polyvinyl chloride, chlorinated polyethylene etc.) and oxygenation etc.

These types of competing reactions can be partially overcome by employing suitable coagent. Coagents are basically multifunctional reactive monomers mostly containing terminal unsaturation, which undergo addition reaction to stabilize the highly reactive polymer radicals. Principally it suppresses the chain scission reaction and enhances the extent of cross-linking. General mechanism for coagent assisted peroxide crosslinking along with possible competing reactions is shown in Figure 1 [7]. Naskar and Noordermeer [8, 9] investigated the possible use of peroxides in the production of PP/EPDM TPVs. They showed the influence of structurally different peroxides with special reference to the mechanical properties. Multifunctional peroxide [10], having peroxide and coagent functionality in a single molecule was also explored to overcome the unpleasant smell and blooming characteristics produced by decomposed products of some peroxides. Thitithammawong *et al.* [11] studied the influences of different peroxides in PP/epoxidized natural rubber (ENR) TPVs. Chatterjee and Naskar [12] also studied the properties of

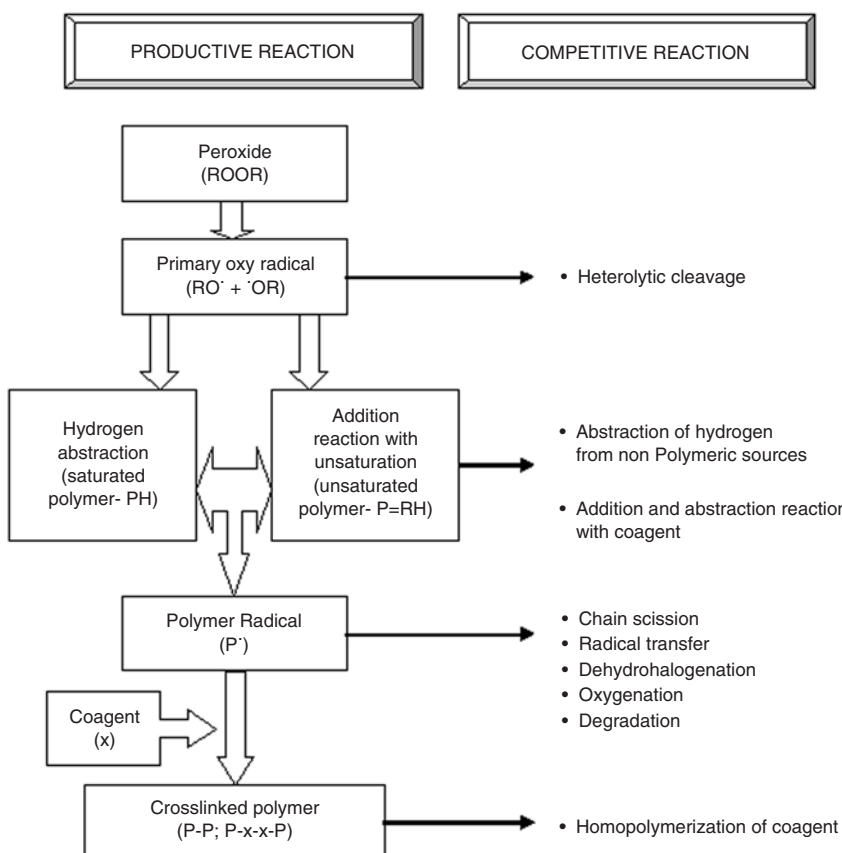


**Figure 1.** Various productive and competitive reactions involved in coagent assisted peroxide system

dicumyl peroxide cured TPVs based on maleated ethylene propylene rubber (m-EPM) and PP using maleated-PP as compatibilizer.

Interrelationships of morphology, properties and processing characteristics of dynamically vulcanized blends have been reviewed by Karger-Kocsis [13]. Properties of the TPVs depend on their morphology and the crosslink density in the elastomer phase. An investigation on the correlation between mechanical and morphological properties of oil extended PP/EPDM TPVs was carried out by Sengupta [14]. Recently Naskar [15] made an extensive review on structure-property relationship of PP/EPDM TPVs. Considerable researches have been pursued on PP/EPDM TPVs, but TPVs based on ethylene octene copolymer and PP were not well explored. Ethylene octene copolymers (EOC) or plastomers are a relatively new class of polymers that emerged with recent advances in metallocene polymerization catalysts. Representing one of the fastest growing synthetic polymers, EOCs are compatible with most of the olefinic materials which impart excellent impact strength for semicrystalline polymers, and offer unique performance capabilities for compounded products [16]. EOC is gradually replacing the field of applications of EPDM rubber and can be considered as a suitable alternative for EPDM. Addition of peroxide in PP/EOC blend involves two major competing reactions:

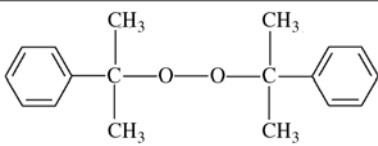
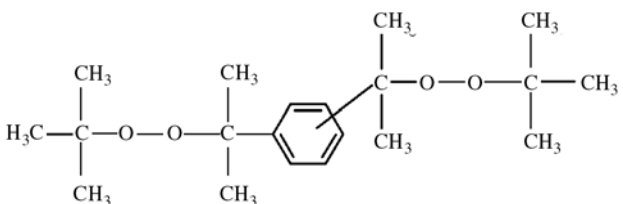
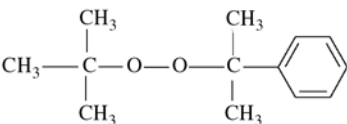
EOC cross-linking and PP degradation by  $\beta$ -scission. Final product properties are thus dependent on the balance among those two competing reactions. The primary objective of the present investigation is to study the influence of structurally different peroxides on the physico-mechanical, thermal and morphological characteristics of the dynamically cross-linked polypropylene (PP) and ethylene octene copolymer (EOC) blends at a fixed blend ratio.

## 2. Experimental

### 2.1. Materials

The general purpose polyolefin elastomer Exact 5171 (specific gravity, 0.870 g/cc at 23°C; comonomer (octene) content 13%; melt flow index (MFI), 1.0 dg/min at 190°C/2.16 kg), was commercialized by Exxon Mobil Chemical Company, USA. Polypropylene (PP) (Specific gravity, 0.9 g/cc at 23°C; melt flow index, 3.0 g/10 min at 230°C/2.16 kg) was obtained from IPCL, India. The coagent, tri allyl cyanurate (SR 507A; Specific gravity, 1.12 g/cc at 23°C) was obtained from Sartomer Company, USA. Three different types of peroxides were used and their commercial names, chemical names and half life data were given in the Table 1. These materials were obtained from Akzo Nobel Chemical Company, The Netherlands.

**Table 1.** Commercial names, chemical names, structures and half-life ( $t_{1/2}$ ) data of various peroxides used

Commercial name	Structure and chemical name	Temperature at which $t_{1/2}$ = one hour [°C]
Perkadox-BC-40BPB (40%)	 <p>Dicumyl peroxide (DCP)</p>	138
Perkadox-14-40B-D (40%)	 <p>Di(2-tert butyl peroxy isopropyl)benzene (DTBPIB)</p>	146
Trigonox-T-50D-D (50%)	 <p>Tert-butyl cumyl peroxide (TBCP)</p>	146

## 2.2. Preparation of PP/EOC TPVs

Compositions showing blend constituents, type and concentration of different peroxides are shown in the Table 2. The experimental variables are the type and concentration of peroxides. All TPVs were prepared by a batch process in a Haake Rheomix600 internal mixer, having a mixing chamber volume of 85 cm<sup>3</sup> with a rotor speed of 80 rpm at 190°C. Immediately after mixing, the composition was passed once through a cold two-roll mill to achieve a sheet of about 2 mm thickness. The sheet was cut and pressed in a compression molding machine (Moore Press, Birmingham, UK) at 200°C, 4 min and 5 MPa pressure. The sheet was then cooled down to room temperature under pressure. Test specimens were die-cut from the compression molded sheet and used for testing after 24 hrs of storage at room temperature. Since different peroxides not only differ in molecular weight but they also have different relative functionality depending on the number of peroxy groups present. From the structures of different peroxides (Table 1), it is clear that one mole of DTBPIB contains two peroxide groups where as DCP and TBCP contain one peroxide group. The technical definition of an equivalent is the amount of substance it takes to combine with one mole of hydrogen ion. A milliequivalent (meq) is 1/1000 of an equivalent, for a monovalent ion one milliequivalent is equal to one mole. In practice, the amount of substance in equivalent often has a small magnitude, so it is frequently expressed in terms of milliequivalents. In order to compare different peroxides, concentrations employed were expressed in terms of milliequivalents per 100 g of pure EOC. TPVs prepared by different peroxides are designated as D for dicumyl peroxide (DCP), T for tert-butyl cumyl peroxide (TBCP) and DT for di(tert-butylperoxyisopropyl)benzene (DTBPIB). The

number in the compound designation (Table 2) corresponds to the respective concentration of peroxide in milliequivalents.

## 2.3. Testing procedure

Tensile tests were carried out according to ASTM D412-98 on dumb-bell shaped specimens using a universal tensile testing machine Hounsfield H10KS (UK) at a constant cross-head speed of 500 mm/min. Tear strength was carried out according to ASTM D-624-81 test method using un-nicked 90° angle test piece. Tension set was performed at room temperature with a stretched condition for 10 minutes at 100% elongation according to ASTM D412-98 method. A Rubber Process Analyzer, RPA-2000 (Alpha Technologies, USA), was used to study the cure-characteristics of the different types of peroxides employed only on the EOC part (PP omitted) at 180°C for 30 minutes at 2.79% strain and a frequency of 1 Hz. Equilibrium solvent swelling measurement was carried out on the pure EOC gum vulcanizate to determine the crosslink density of the EOC. The crosslink density was calculated using the modified Flory–Rehner equation. A circular test piece of 2 mm thickness was allowed to swell in cyclohexane for about 48 hours to attain equilibrium swelling condition. Initial weight, swollen weight and deswollen or dried weight were taken and substituted in the equation to get the crosslink density values.

Wide angle X-ray Diffraction was performed with a Philips PW 1840 X-ray diffractometer (The Netherlands) with a copper target (CuK $\alpha$ ). The samples were scanned from 10 to 40° (2 $\theta$ ) at a scanning speed of 0.05° 2 $\theta$ /s with an operating voltage of 40 kV and current of 20 mA. Differential scanning calorimeter (DSC) measurements were carried out using a DSC Q100 V.8.1 (TA instruments,

**Table 2.** TPV compositions in phr (parts per hundred rubber)

COMP-ID	PP-EOC	D1	D3	D5	D7	T1	T3	T5	T7	DT1	DT3	DT5	DT7
EOC	100	100	100	100	100	100	100	100	100	100	100	100	100
PP	50	50	50	50	50	50	50	50	50	50	50	50	50
DCP	–	0.68(1)	2.03(3)	3.38(5)	4.73(7)	–	–	–	–	–	–	–	–
TBCP	–	–	–	–	–	0.42(1)	1.26(3)	2.10(5)	2.94(7)	–	–	–	–
DTBPIB	–	–	–	–	–	–	–	–	–	0.43(1)	1.27(3)	2.13(5)	2.98(7)
TAC	–	2	2	2	2	2	2	2	2	2	2	2	2

Values in the parenthesis corresponds to the concentration of corresponding peroxide expressed in milliequivalent.

D – Dicumyl peroxide (DCP)

T – Tertbutylcumyl peroxide (TBCP)

DT – Di(tertbutylperoxyisopropyl) benzene (DTBPIB)

USA). The scans were taken in the temperature range from  $-80$  to  $200^{\circ}\text{C}$  with a programmed heating rate of  $10^{\circ}\text{C}/\text{min}$  under nitrogen atmosphere. Phase morphology of the cryo-fractured samples of various blends was investigated by Digital Scanning Electron Microscope (SEM) (JEOL JSM 5800, Japan).

### 3. Results and discussion

#### 3.1. Mechanical properties

Mechanical properties are considerably improved by the dynamic vulcanization process. Influences of different peroxides on the mechanical properties of the PP/EOC TPVs are shown in the Figures 2–6. Effect of peroxide on a particular system depends on the nature of the polymer, type and concentration of peroxide and also upon the reactivity of other components in the system. It is generally accepted that peroxide causes cross-linking in EOC and also causes  $\beta$  chain scission in PP by abstraction of tertiary hydrogen atom from the main chain polymers. Addition of co-agents, which are highly reactive towards free radicals, can improve the cross-linking tendency to form tighter network in EOC and also decrease the extent of degradation in PP. Figure 2 shows the improvement in tensile strength with the addition of co-agent assisted different peroxide system with varying concentration. It is observed that tensile strength increases initially, reaches a maximum and then decreases for DCP and DTBPBIB, whereas for TBCP after initial increase it levels off. DCP cured TPVs show maxi-

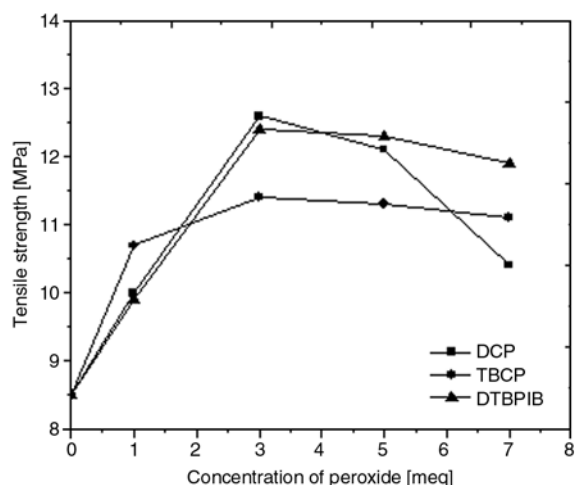


**Figure 2.** Tensile strength as a function of concentration of different peroxides. (Composition corresponds to Table 2)

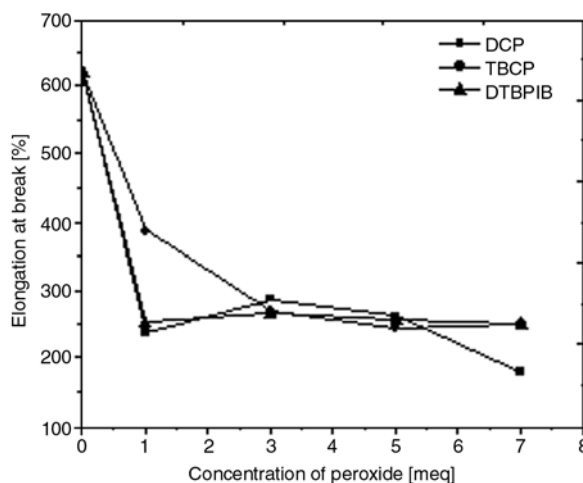


**Figure 3.** Elongation at break as a function of concentration of different peroxides. (Composition corresponds to Table 2)

um tensile strength at 3 meq concentration. On decomposition, DCP and DTBPBIB produce highly reactive radicals and the amount of generated radicals are also higher than for TBCP [8]. The decrease in tensile strength at higher concentration of DCP and DTBPBIB may be due to the severe degradation on the PP phase. Figure 3 shows the elongation at break behavior as a function of concentration of different peroxides. Elongation at break continuously decreases although little difference between the various peroxides used is noticed; TBCP shows a relatively higher value compared to others. Decreasing trend may be associated with the phase inversion on morphology and cross-linking in the EOC phase. Also at higher dosage level, the nature of failure of the samples shows brittle type. Moduli at 100% elongation as a function of concentration of different peroxides are shown in Figure 4. Modulus value increases initially and then reaches a plateau. DCP shows the highest modulus and TBCP shows the lowest modulus, which corresponds to the trend in tensile strength values. It is observed that crosslinking efficiency of DCP and DTBPBIB is higher than TBCP, which is further manifested from the cure characteristics.

Tear strength of the TPVs increase considerably by the dynamic vulcanization process. Influence of different peroxides on the tear strength is shown in Figure 5. During dynamic vulcanization, along with the cross-linking process on EOC phase, grafting of EOC on PP can also take place; the latter improves the interfacial adhesion. DTBPBIB shows



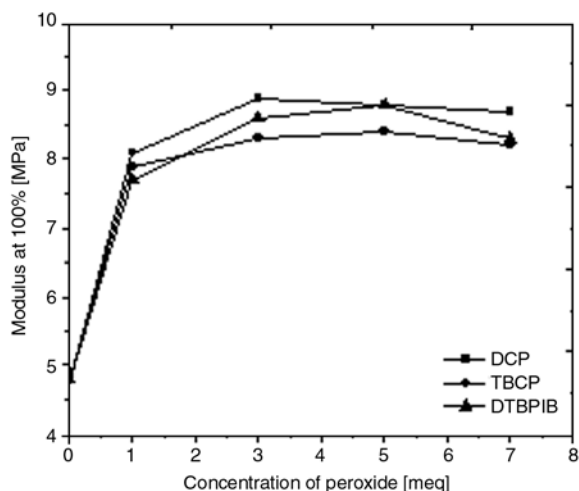


**Figure 4.** Modulus at 100% as a function of concentration of different peroxides. (Composition corresponds to Table 2)

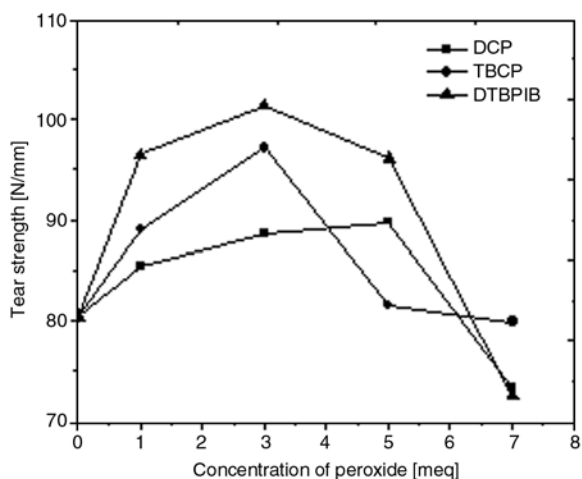


**Figure 5.** Tear strength as a function of concentration of different peroxides. (Composition corresponds to Table 2)

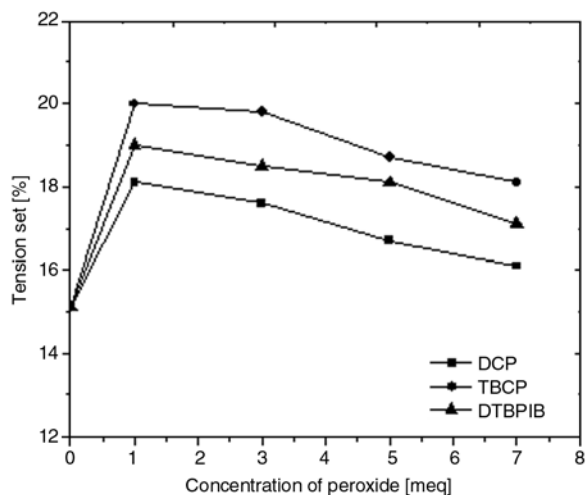


**Figure 6.** Tension set as a function of concentration of different peroxides. (Composition corresponds to Table 2)

the maximum tear strength at 3 meq concentration and DCP shows the least value. Decreasing trend on higher loading of peroxide may be due to severe degradation in PP and thus it has limited extensibility of cross-linked EOC [17]. DTBPIB is expected to form better interfacial cross-linking. Tensions set values as the function of concentration of different peroxides are shown in Figure 6. Unvulcanized blends show lower set values; whereas dynamically vulcanized ones show higher values. However, with further addition of peroxide tension set decreases continuously. This behavior may be explained on the basis of morphological aspect. In unvulcanized blend EOC being the major proportion give rise to continuous phase and PP as dispersed phase. It has been previously reported that EOC exhibit higher viscosity and elastic property than PP [18]. However, phase inversion occurs due to dynamic vulcanization which causes cross-linked EOC as dispersed phase and PP as continuous matrix which is responsible for the higher set values. Further as the concentration of peroxide increases, formation of tighter network causes gradual decrease in set values (higher elastic recovery property). Among the peroxides taken under investigation, DCP exhibits lower set values than DTBPIB and TBCP.

Hence mechanical properties of PP/EOC TPVs by coagent assisted peroxide would be ascribed by the extent of cross-linking in the EOC phase as well as extent of PP degradation. Different types of peroxides have different cross-linking efficiency and exhibit different decomposition pattern under given condition [8] which is responsible for governing final TPV properties.

### 3.2. Cure characteristics and crosslink density

In order to interpret the effect of different peroxides on the PP/EOC TPVs, it is necessary to understand the reactivity and efficiency of different peroxide only on EOC phase (PP omitted). Table 3 shows the cure characteristics for pure EOC gum vulcanizate. It is observed that irrespective of type of peroxide used, increase in concentration of peroxide causes increase in maximum torque (Max  $S$ ) and hence delta torque values ( $\Delta S$ ). This is evident that increase in concentration of peroxide, more radicals are formed and thus higher the crosslinking effi-

**Table 3.** RPA test results and crosslink density for pure EOC gum vulcanisates

Compound name	Min S [dNm]	Max S [dNm]	ΔS [dNm]	T <sub>10</sub> [m:s] <sup>a</sup>	T <sub>90</sub> [m:s] <sup>a</sup>	Cure rate [%]	Crosslink density (ν) ·10 <sup>-4</sup> mol/ml
RD1	0.35	3.59	3.23	0.4	2.6	44.0	1.85
RD3	0.47	4.20	3.73	0.3	2.4	48.0	2.50
RD5	0.87	5.06	4.19	0.3	2.3	48.0	2.88
RT1	0.10	3.12	3.01	1.0	5.2	23.8	1.02
RT3	0.17	4.18	4.01	0.5	4.5	24.8	1.88
RT5	0.27	4.40	4.12	0.4	4.2	26.1	1.96
RDT1	0.20	3.65	3.43	0.5	5.6	19.4	1.93
RDT3	0.22	4.34	4.12	0.4	5.2	21.0	2.52
RDT5	0.43	5.20	4.77	0.3	4.2	25.9	2.69

<sup>a</sup>m:s – minutes:seconds

R denotes the compound composition in the Table 2 without PP content

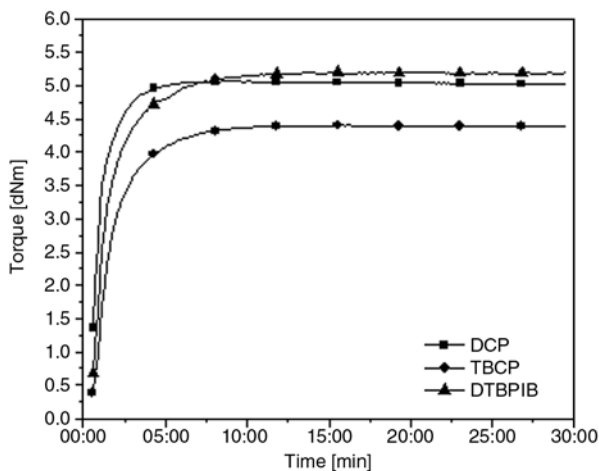


**Figure 7.** Rheographs for EOC compounds with 5 meq concentration of different peroxides

ciency and simultaneous decrease in scorch ( $T_{10}$ ) and optimum cure time ( $T_{90}$ ). Figure 7 shows the rheographs of different peroxides on the EOC phase at a concentration of 5 meq. As can be observed from the Figure 7 and Table 3, DTBPIB shows the maximum torque values followed by DCP and TBCP whereas considering the rate of cross-linking i.e., cure rate index (CRI), DCP is the fastest followed by TBCP and DTBPIB.

Crosslink density of pure EOC gum vulcanizate ( $\nu$ ) was calculated by using Flory–Rehner equation (Equation (1)):

$$\nu = -\frac{1}{V_s} \cdot \frac{\ln(1 - V_r) + V_r + \chi(V_r)^2}{(V_r)^{1/3} - 0.5V_r} \quad (1)$$

where  $V_s$  – molar volume of cyclohexane [ $\text{cm}^3/\text{mol}$ ],  $\chi$  – polymer swelling agent interaction parameter, which in this case is 0.306 [19] and  $V_r$  – volume fraction of ethylene-octene copolymer in the

swollen network [ $\text{cm}^3/\text{mol}$ ], which can be expressed by Equation (2):

$$V_r = \frac{1}{A_r + 1} \quad (2)$$

where  $A_r$  is the ratio of the volume of absorbed cyclohexane to that of ethylene-octene copolymer after swelling.

TBCP is found to give lowest crosslink densities, where as DCP and DTBPIB show higher and the latter shows only marginal difference in the values. There was a clear trend of variation in modulus values of TPVs for different peroxide with the delta torque and crosslink density values. Change in elongation at break and tension set values of TPVs with increase in concentration of different peroxide are also well correlated with the extent of crosslink density.

### 3.3. Differential scanning calorimeter (DSC)

DSC data of PP/EOC simple blends along with three different peroxide cured PP/EOC TPVs are shown in the Table 4. The blend shows two glass transitions ( $T_g$ ) and melting endotherms ( $T_m$ ). These clearly indicate that the blend components are thermodynamically immiscible. By dynamic vulcanization they are made technologically compatible which is manifested by improvement in mechanical properties. With the addition of peroxide, two major reactions take place. First, glass transition of EOC is shifted to higher temperature which may be due to cross-linking in EOC phase. Secondly, melting endotherm of both EOC and PP phases were diffused or obscured. This can be

**Table 4.** DSC data of PP/EOC TPVs with different peroxides

Compound name	T <sub>g</sub> EOC [°C]	ΔH <sub>f</sub> EOC [J/g]	% CRY. EOC	T <sub>m</sub> EOC [°C]	T <sub>g</sub> PP [°C]	ΔH <sub>f</sub> PP [J/g]	% CRY. PP	T <sub>m</sub> PP [°C]
PP	–	–	–	–	9	98.88	47.76	165
EOC	–51	23.34	8.05	50	–	–	–	–
PP-EOC	–51	16.22	8.47	50	7	32.75	47.50	165
D3	–47	15.97	8.26	52	8	30.82	44.70	163
T3	–48	15.51	8.02	51	7	31.58	45.80	164
DT3	–47	15.72	8.13	52	8	30.48	44.20	163
D15*	–45	11.32	5.86	50	1	23.65	34.62	150

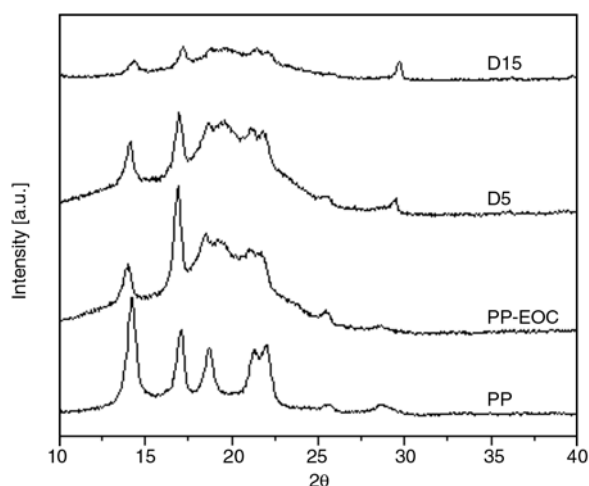
\*DCP of 15 meq concentration

explained on the basis of cross-linking in EOC part and grafting of EOC on PP or grafting of PP on EOC that limits the crystallizing tendency thereby reducing the heat of fusion ( $\Delta H_f$ ) and percentage crystallinity (% CRY) of PP as shown in Table 4. DCP and DTBPIB show higher cross-linking efficiency over TBCP and correspondingly affect more the crystallization of PP.

Further to understand the influence of higher dosage level of peroxide, DCP of 15 milliequivalents (meq) concentration was taken for the preparation of TPVs (in Table 4 designated as D15). It is interesting to note that apart from above mentioned effects, perfectness of the crystals in PP (size of the crystals) is affected considerably which is observed by a drastic fall in melting temperature from 165 to 150°C; glass transition temperature of PP also decreases from 8 to 1°C.

### 3.4. Wide angle X-ray diffraction (WAXD)

Crystallinity level and pattern of the blends were studied by using wide angle x-ray scattering technique. Figure 8 shows the WAXD pattern of the pure PP, PP-EOC unvulcanized blend and dynamically vulcanized blends. The diffraction pattern has a broad amorphous background superimposed on sharp crystalline peaks. Generally PP has three crystalline structure  $\alpha$  (monoclinic),  $\beta$  (pseudo hexagonal) and  $\gamma$  (triclinic). The diffraction pattern of PP has five sharp diffraction lines corresponding to 110, 040, 130, 111 and overlapping of 131 with 041 planes in the crystal which are located at a scattering angle  $2\theta$  of 14.2, 17.1, 18.7, 21.4 and 22.0° respectively. The pattern shows only  $\alpha$  form because there is no line at  $2\theta$  of 16.1° generally associated with  $\beta$  form [20]. Crystallinity pattern can be inferred from the change in position of

**Figure 8.** WAXD of PP, unvulcanized and dynamically vulcanized PP/EOC blends

peaks, whereas crystallinity level from the intensity of the peaks. Percentage crystallinity value can be calculated using Equation (3) from the area under the crystalline and amorphous portions.

$$X_c = \frac{I_c}{I_c + I_a} \cdot 100 \quad (3)$$

where  $X_c$  – degree of crystallinity [%],  $I_c$  – integrated intensity of crystalline region,  $I_a$  – integrated intensity of amorphous region.

Table 5 shows the degree of crystallinity in TPVs calculated from the WAXD. Upon adding EOC with PP, there is no change in the peak position which suggests that blending only slightly affects the  $\alpha$  monoclinic pattern of PP. But peak at

**Table 5.** Degree of crystallinity  $X_c$  calculated from WAXD

Compound name	% Crystallinity
PP (Pure)	50.9
PP-EOC (Unvulcanized)	49.4
D5 (Dynamically vulcanized)	46.7
D15 (Dynamically vulcanized)	29.6

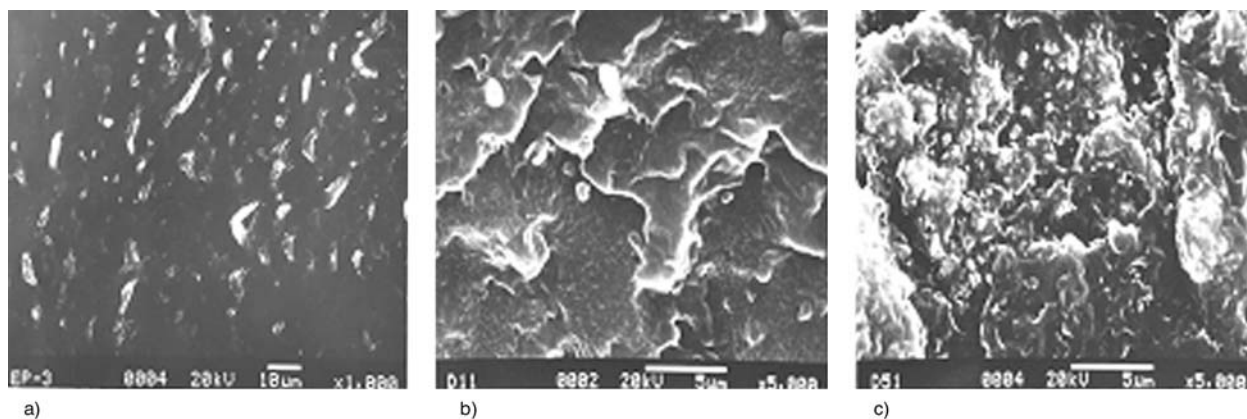


**Figure 9.** Morphology of the 50/100 PP/EOC blend (a) without dynamic vulcanization (b) 1 meq concentration of DCP (c) 5 meq concentration of DCP

$2\theta = 14.1^\circ$  corresponding to  $\alpha$  (110) plane intensity decreases indicating a small decrease in crystallinity level. This can be explained by the migration of EOC phase into the interchain spaces of PP. Similar behavior was obtained in PP/EPDM simple blends. It shows that increasing the EPDM content in the blend cause more defective and thinner lamellar crystals [21].

From the WAXS graph (Figure 8) of 5 meq concentration of DCP cured TPVs, again the intensity of the peaks decreases suggest the decrease in the crystallinity value. This may be due to the formation in-situ grafting of EOC with PP, which further reduces the regular arrangement of crystalline region and makes the crystallization process difficult. In order to have a better understanding of the effect of peroxide on the crystalline pattern, 15 meq concentration of DCP cured TPVs was analyzed. As mentioned previously, grafting of EOC on PP and limited extent of crosslinking in PP lead to decrease the crystallinity and the perfectness of the spherulite. Guan *et al.* [22] also reported that grafting of modifiers (like guanidine, diamide polymers) on PP backbones cause a decrease in crystallinity level and affect the perfectness of spherulites. Variation in the packing in the crystal lattice also inferred from the change in the peak position at 15 meq concentration.

### 3.5. Morphology

Morphology of un-vulcanized and dynamically vulcanized blends of PP/EOC TPVs are shown in Figure 9. In general morphology of un-vulcanized blend shows either a co-continuous phases or larger

rubbery particle dispersed in PP phase or PP particles dispersed in an EOC matrix depending on the blend composition. In this blend system of PP/EOC, EOC being in greater proportion than PP, the former forms continuous phase and PP as dispersed phase. Figure 9a shows the unvulcanized blend of PP/EOC, since both the components having good affinity show the elongated particles of PP dispersed in EOC matrix. During dynamic vulcanization, phase inversion occurs. This is evident because crosslinking of rubbery phase leads to drastic increase in viscosity which forms cross-linked EOC droplets in PP matrix and once it was cross-linked it shows higher stability against coalescence. As these droplets are formed PP becomes the continuous phase which maintains thermoplasticity of the blends. Figures 9b and 9c show the dynamically vulcanized blends with 1 and 5 meq concentration of DCP respectively. There is no much difference in the morphology of different peroxides taken under investigation. However, as the peroxide concentration increases, high degree of vulcanization persist, thereby decreasing the particle size with increasing number of particles [23].

### 4. Conclusions

Novel thermoplastic vulcanizates (TPVs) are prepared by dynamic vulcanization process from 50/100 blend ratio of PP/EOC by coagent assisted peroxide as crosslinking system. Dynamically vulcanized blends show better mechanical and thermal properties than those of unvulcanized blends. Different peroxides show different crosslinking efficiency and different decomposition products hav-



ing different reactivity. The choice of the best peroxide depends on the extent of crosslinking in EOC phase and also on the extent of degradation in the PP phase. Out of the three peroxides used in this investigation di cumyl peroxide (DCP) shows the best overall balance of properties except tear strength. DTBPIB shows a significant improvement in tear strength. Concentration of peroxide also has significant influence on the mechanical properties. Higher concentrations of peroxides cause increasing brittle failure of the sample due to severe degradation in the PP phase. Peroxide of 3 meq is sufficient to give significant improvement in mechanical properties. From the cure characteristics, different peroxides employed can be ranked on basis of efficiency and reactivity. Crosslinking efficiency can be ranked as DTBPIB ≥ DCP > TBCP and cure rate can be ranked as DCP > TBCP ≥ DTBPIB. Differential scanning calorimetry and morphological analysis show that the blend components are thermodynamically immiscible and exist as a heterogeneous biphasic system. DCP and DTBPIB form relatively highly reactive radicals and hence show better mechanical properties and correspondingly affect more the crystallization of PP. As the concentration of peroxide increases, particle size decreases. However, mechanical properties of these TPVs are not good enough at high concentration, which is due to severe degradation in the PP phase in presence of peroxide. From WAXS data, there is no measurable shift in the peak position suggesting no significant change in the crystallinity pattern with the addition of EOC and also by dynamic vulcanization, but the level of crystallinity (% crystallinity) is affected by the same.

## Acknowledgements

The authors are thankful to Council for Scientific and Industrial Research (CSIR), New Delhi, India for their financial assistance.

## References

- [1] Legge N. R., Holden G., Schroeders H. E.: Thermoplastic elastomer: A comprehensive review. Hanser, Munich (1987).
- [2] De S. K., Bhowmick A. K.: Thermoplastic elastomers from rubber-plastic blends. Horwood, London (1990).

- [3] Gessler A. M., Haslett W. H.: Process for preparing a vulcanized blend of crystalline polypropylene and chlorinated butyl rubber. US patent 3037954, USA (1962).
- [4] Coran A. Y., Patel R.: Rubber-thermoplastic compositions. Part I. EPDM-polypropylene thermoplastic vulcanizates. *Rubber Chemistry and Technology*, **53**, 141–150 (1980).
- [5] Abdou-Sabet S., Fath M. A.: Thermoplastic elastomer blends of olefin rubber and polyolefin resin. US patent 4311628, USA (1982).
- [6] Loan L. D.: Mechanism of peroxide vulcanization of elastomers. *Rubber Chemistry and Technology*, **40**, 149–176 (1967).
- [7] Dluzeski P. R.: Peroxide vulcanization of elastomers. *Rubber Chemistry and Technology*, **74**, 451–490 (2001).
- [8] Naskar K., Noordermeer J. W. M.: Dynamically vulcanized PP/EPDM blends-effects of different types of peroxide on the properties. *Rubber Chemistry and Technology*, **76**, 1001–1018 (2003).
- [9] Naskar K., Noordermeer J. W. M.: Influence of various peroxides in PP/EPDM thermoplastic vulcanizates at varied blend ratios. *Journal of Elastomer and Plastics*, **38**, 163–180 (2006).
- [10] Naskar K., Noordermeer J. W. M.: Dynamically vulcanized PP/EPDM blends-effects: Multifunctional peroxides as crosslinking agents, Part I. *Rubber Chemistry and Technology*, **77**, 955–971 (2004).
- [11] Thitithammawong A., Nakason C., Sahakaro K., Noordermeer J. W. M.: Thermoplastic vulcanizate based on epoxidized natural rubber/polypropylene blends, selection of optimal peroxide type and concentration in relation to mixing conditions. *European Polymer Journal*, **43**, 4008–4018 (2007).
- [12] Chatterjee K., Naskar K.: Development of thermoplastic elastomers based on maleated ethylene propylene rubber and polypropylene by dynamic vulcanization. *Express Polymer Letters*, **1**, 527–534 (2007).
- [13] Karger-Kocsis J.: Thermoplastic rubbers via dynamic vulcanization. in 'Polymer Blends and Alloys', (eds.: Shonaike G. O., Simon G. P.) Marcel Dekker, New York, 125–154 (1999).
- [14] Sengupta P.: Morphology of olefinic thermoplastic elastomers. PhD thesis, Twente University, Netherlands (2004).
- [15] Naskar K.: Thermoplastic elastomer based on PP/EPDM blends by dynamic vulcanization: A review. *Rubber Chemistry and Technology*, **80**, 504–510 (2007).
- [16] Walton K. L.: Metallocene catalysed ethylene/alpha olefin copolymers used in thermoplastic elastomers. *Rubber Chemistry and Technology*, **77**, 552–568 (2004).
- [17] George J., Varughese K. T., Thomas S.: Dynamically vulcanized thermoplastic elastomer blends of polyethylene and nitrile rubber. *Polymer*, **41**, 1507–1517 (2000).

- [18] Williams M. G., Harrington B. A., Miller T. M.: New low density EXACT® plastomers as high performance impact modifiers. A technical report by Exxon Mobil Company (2003).
- [19] Braton A. F. M.: Handbook of solubility parameters and other cohesion parameters. CRC Press, Boca Raton (1983).
- [20] George J., Varughese K. T., Thomas S.: Thermal and crystallisation behavior of isotactic polypropylene/nitrile rubber blends. *Polymer*, **41**, 5485–5503 (2000).
- [21] Bielinski D. M., Slusarski L., Wlochowicz A., Slusarczyk C., Douillard A.: Some aspect of isotactic polypropylene crystallization in an ethylene-propylene-diene rubber matrix. *Polymer International*, **44**, 161–173 (1997).
- [22] Guan Y., Wang S., Zheng A., Xiao H.: Crystallisation behaviour of polypropylene and functional polypropylene. *Journal of Applied Polymer Science*, **88**, 872–877 (2003).
- [23] Abdou-Sabet S., Patel R. P.: Morphology of elastomeric alloys. *Rubber Chemistry and Technology*, **64**, 769–779 (1991).